https://doi.org/10.35662/unine-thesis-2962

Numerical Modelling of Aftershock Sequences, Volcano-Tectonic Interactions, and Pandemic Propagation

Thanushika Gunatilake

A Doctoral Dissertation submitted to the

University of Neuchâtel

in

Center for Hydrogeology and Geothermics
CHYN

Accepted on the recommendation of:
Prof. Stephen A. Miller, University of Neuchâtel, Switzerland
Prof. Philippe Renard, University of Neuchâtel, Switzerland
Prof. Taras Gerya, ETH Zürich, Switzerland

https://orcid.org/0000-0001-2345-6789

UNIVERSITÉ DE NEUCHÂTEL

Faculté des Sciences
Secrétariat-décanat de Faculté
Rue Emile-Argand 11
2000 Neuchâtel – Suisse
Tél : + 41 (0)32 718 21 00
E-mail : secretariat.sciences@unine.ch

IMPRIMATUR POUR THESE DE DOCTORAT

La Faculté des sciences de l'Université de Neuchâtel autorise l'impression de la présente thèse soutenue par

Madame Thanushika GUNATILAKE

Titre:

"Numerical Modelling of Aftershock Sequences, Volcano-Tectonic Interactions, and Pandemic Propagation"

sur le rapport des membres du jury composé comme suit:

- Prof. Stephen A. Miller, Université de Neuchâtel, Suisse
- Prof. Philippe Renard, Université de Neuchâtel, Suisse
- Prof. Taras Gerya, ETH Zurich, Suisse

Neuchâtel, le 19 juillet 2022

Le Doyen, Prof. A. Bangerter

Declaration

I, Thanushika Gunatilake, declare that this thesis titled 'Numerical Modelling of Aftershock Sequences, Volcano-Tectonic Interactions, and Pandemic Propagation' and the work presented in it are my own. I confirm that:

- This work was done mainly during candidature for a research degree at this University.
- None of the parts of this thesis have been previously submitted for a degree or other qualification at any other institution.
- I have quoted from the work of others and have acknowledged all main sources of help. With the exception of such quotations, this thesis is entirely my own work.

Signed: Thanushika Gunatilake

Date: 31.07.2022

Abstract

The mystery of the dominant mechanism driving aftershocks is almost 130 years old. In 1894, Omori first empirically established that the rate of aftershocks for most aftershock sequences decreases approximately as 1/time. This is known as Omori's law. Many other empirical fits have been attempted, but the most commonly cited manifestation of this law is the modified Omori-Utsu Law, which can fit most aftershock sequences using fitting parameters that include aftershock productivity and a time lag until the onset of a power law decay in time. Few physical models exist, but the one most relevant to this thesis was first proposed in 1972 by Nur and Booker, who suggested that the high-pressure fluid induced by stress drops during an earthquake could trigger subsequent seismicity by reducing the effetive normal stress of neighboring regions. Recent studies showed that a physical, fluid-based model can successfully reproduce Omori-type behavior by arguing that the aftershock decay rate reflects the tectonic ability to heal the co-seismically generated permeable network. More precisely, the mainshock creates permeable networks that provide escape pathways for high-pressure fluids and generate aftershocks along these flow paths. Like dominoes, the aftershocks create new pathways. Postseismic deformation and chemical precipitation processes reseal the permeable network and influence aftershock decay rates. However, not all earthquake sequences follow the typical Omori behavior; some examples are the 2011 Tohoku earthquake sequence (Mw 9.1) in northern Japan, the 2016 Amatrice-Visso-Norcia (AVN) earthquake sequence in the central Apennines in Italy (Mw 6.5), and the 2014 Iquique earthquake sequence in Chile (Mw 8.1). These earthquakes triggered hundreds of thousands of aftershocks in the first year and showed dramatic differences in aftershock rates along strike, with non-Omori type aftershock behavior. In this thesis, I present a hypothesis for a fluid-driven aftershock cycle in which the differential decay rate is explained by continuous fluid source generation through thermal decomposition. The spread of the COVID19 virus first demonstrates the importance of an internal source. Using a non-linear diffusion model with a source term, I calculate the diffusion of infection pressure through a porous society. The internal source mimics the ongoing transmission of the virus from a human to a human. In earthquake physics, dehydration and decarbonization of H_2O and CO_2 at depth provide continuous fluid sources that trigger thousands of aftershocks. Using the non-linear diffusion model, I compare the temporal and spatial evolution of the 2016 earthquake-rich AVN sequence with numerically triggered aftershocks and show that aftershocks are driven

by co-seismically generated (high-pressure) fluid sources through thermal decomposition. Earthquakes without trapped fluid sources at depth or without thermal decomposition generate few, if any, aftershocks. The spatial distribution of evolving high-pressure fluid required developing a 3D dimensional model that includes (i) high-pressure fluid generation by thermal decomposition and (ii) the dynamics of permeability that plays a significant role. Higher permeability allows flow paths to remain open for extended periods of time, contribute to the aftershock sequence, and strongly influence the spatial and temporal variation of aftershocks. In this work, I show excellent spatial and temporal correlations between model results and observations for the AVN (2016) and L'Aquila (2009) earthquake sequences in the Apennines. Furthermore, seismic activity opens pre-existing vertical fractures that provide pathways for upwelling high-temperature magma, which is beneficial for geothermal production. The interplay between the penultimate eruption of Japan's Aso volcano in 2016, the associated Kumamoto sequence, and its impact on local geothermal power plants are explored using a nonlinear advection/diffusion model for pore pressure and heat flow. The results interpretations of the model presented in this thesis have potentially far-reaching implications in geophysics, geodynamics, and earthquake physics.

Résumé

Le mystère du mécanisme dominant à l'origine des répliques est vieux de près de 130 ans. En 1894, Omori a été le premier à établir empiriquement que le taux de répliques pour la plupart des séquences de répliques diminue approximativement comme 1/temps. C'est ce que l'on appelle la loi d'Omori. De nombreux autres ajustements empiriques ont été tentés, mais la manifestation la plus couramment citée de cette loi est la loi d'Omori-Utsu modifiée, qui peut s'adapter à la plupart des séquences de répliques en utilisant des paramètres d'ajustement qui incluent la productivité des répliques et un délai jusqu'à l'apparition d'une loi de puissance décroissante dans le temps. Il existe peu de modèles physiques, mais celui qui est le plus pertinent pour cette thèse a été proposé pour la première fois en 1972 par Nur et Booker, qui ont suggéré que le fluide à haute pression induit par les chutes de tension pendant un tremblement de terre pourrait déclencher une sismicité ultérieure en réduisant la tension normale effective des régions voisines. Des études récentes ont montré qu'un modèle physique, basé sur les fluides, peut reproduire avec succès le comportement de type Omori en soutenant que le taux de décroissance après une réplique reflète la capacité tectonique à guérir le réseau perméable généré coséquemment. Plus précisément, le choc principal crée des réseaux perméables qui fournissent des voies d'évacuation pour les fluides à haute pression et génèrent des répliques le long de ces voies d'écoulement. Comme des dominos, les répliques créent de nouvelles voies d'écoulement. La déformation postsismique et les processus de précipitation chimique referment le réseau perméable et influencent les taux de décroissance des répliques. Cependant, toutes les séquences de séismes ne suivent pas le comportement typique d'Omori ; quelques exemples sont la séquence de séismes de Tohoku 2011 (Mw 9,1) dans le nord du Japon, la séquence de séismes Amatrice-Visso-Norcia (AVN) 2016 dans les Apennins centraux en Italie (Mw 6,5), et la séquence de séismes Iquique 2014 au Chili (Mw 8,1). Ces séismes ont déclenché des centaines de milliers de répliques au cours de la première année et ont montré des différences spectaculaires dans les taux de répliques le long de la grève, avec un comportement de répliques de type non-Omori. Dans cette thèse, je présente une hypothèse pour un cycle de répliques alimenté par des fluides, dans laquelle le taux de décroissance différentiel est expliqué par la génération continue de sources de fluides par décomposition thermique. La propagation du virus COVID19 démontre d'abord l'importance d'une source interne. En utilisant un modèle de diffusion non linéaire avec un terme source, je calcule la diffusion de la pression d'infection à travers une

société poreuse. La source interne imite la transmission continue du virus d'un humain à un autre. Dans la physique des tremblements de terre, la déshydratation et la décarbonisation de H_2O et CO_2 en profondeur fournissent des sources de fluides continues qui déclenchent des milliers de répliques. En utilisant le modèle de diffusion non linéaire, je compare l'évolution temporelle et spatiale de la séquence AVN riche en séismes de 2016 avec des répliques déclenchées numériquement et je montre que les répliques sont entraînées par des sources de fluide générées de manière cosismique (haute pression) par décomposition thermique. Les tremblements de terre sans sources de fluide piégées en profondeur ou sans décomposition thermique génèrent peu, voire pas, de répliques. La distribution spatiale du fluide haute pression en évolution a nécessité le développement d'un modèle tridimensionnel qui inclut (i) la génération de fluide haute pression par décomposition thermique et (ii) la dynamique de la perméabilité qui joue un rôle important. Une perméabilité plus élevée permet aux chemins d'écoulement de rester ouverts pendant de longues périodes, de contribuer à la séquence de répliques et d'influencer fortement la variation spatiale et temporelle des répliques. Dans ce travail, je montre d'excellentes corrélations spatiales et temporelles entre les résultats du modèle et les observations pour les séquences de séismes AVN (2016) et L'Aquila (2009) dans les Apennins. En outre, l'activité sismique ouvre des fractures verticales préexistantes qui constituent des voies de remontée du magma à haute température, ce qui est bénéfique pour la production géothermique. L'interaction entre l'avant-dernière éruption du volcan japonais Aso en 2016, la séquence associée de Kumamoto, et son impact sur les centrales géothermiques locales sont explorés à l'aide d'un modèle d'advection/diffusion non linéaire pour la pression interstitielle et le flux de chaleur. Les interprétations des résultats du modèle présenté dans cette thèse ont des implications potentiellement importantes en géophysique, en géodynamique et en physique des séismes.

Acknowledgements

It is my pleasure to express my gratitude to Prof. Stephen A. Miller for supervising my dissertation and for his constant guidance and support throughout my work. I admire his enthusiasm and intuition for science, which provided us with hours of great discussion. I would also like to thank Batoul Geisler for our incredible time in our office and thriving discussions.

I would like to express my gratitude to Prof. Dr. Taras Gerya and Prof. Dr. Philippe Renard for their willingness to join the examination committee. Another thank you goes to all my colleagues and friends at CHYN. In particular, I would like to thank Valentin Dall'Alba-Arnau, Alexis Neven, Lea Perrochet and Arnaud Rüegg for the pleasant atmosphere. And most of all, I would like to thank Carine Erard Brayek, Sabine Erb Robert, and Corinne Carraux-Drey, who always helped me whenever I needed it.

I would also like to thank all my friends abroad who believed in me and always supported me. Especially to my best friend Deniz Zimmermann, who always had the right word to cheer me up. Also, a big thank you to Irmgard Amaru, Fritz Rick, Tom McCann, Philipp Müller, and Florian Becht, who supported me the best way during my Ph.D.

I am very grateful for the love, patience, and support of my dear parents Sandra Gunatilake, Tilaksiri Gunatilake, my big sister Erandika Gunatilake and my big brother Tarindu Gunatilake. I am very grateful to my family for their constant help in pursuing my dreams, and I admire their support throughout my life. Blood is thicker than water. Finally, I am very grateful to my boyfriend, Thomas Heinze, for his constant encouragement and opening my eyes to an academic career. I am fortunate to have such a supportive person who is always there for me, giving me comfort and peace in difficult times and bringing joy to my life. Thank you.

Table of Contents

List of Figures

Chapter 1

Introduction

Devastating earthquakes and tsunamis claimed nearly 750,000 lives worldwide over a time span of only two decades (1998 to 2017) [Becker et al., 2022]. Collateral damage included more than 125 million people injured, left homeless, or evacuated. Although more resilient structure and earthquake preparedness have improved in developed countries [Ritchie and Roser, 2014], these natural hazards remain. Our aim as scientists is to better understand these natural phenomena to mitigate the impacts of the resulting catastrophe.

The Earth has experienced relentless motion, collision, and destruction since its formation. This motion on a sphere manifests as poloidal motion through convergence and divergence, while strike-slip accommodates the transform component. The collision zones where the denser oceanic lithosphere converges with a less dense continental lithosphere are known as subduction zones [Stern, 2002]. This situation occurs, for example, where the oceanic Nazca plate subducts beneath the South American plate [Barazangi and Isacks, 1979]. Other examples around the Pacific Rim (e.g., Ring of Fire) include the Indonesian Archipelago, the Japan Trench, the Aleutian Island Chain and the Cascadia subduction zone [Hinga, 2015]. Convergent rates vary from a few centimeters to 10 cm per year. Active volcanoes and frequent earthquakes characterize the convergence of two plates [Kodaira et al., 2021, Cherniawsky et al., 2007] including the largest earthquakes on Earth known as megathrust earthquakes [Ruiz and Madariaga, 2018, van Dinther et al., 2014]. These earthquakes are interplate earthquakes with moment magnitudes (Mw) that can exceed 9.0 [Igarashi and Kato, 2021] and typically generate devastating tsunamis. The greatest ever recorded earthquake was the Mw 9.5 in southern Chile, followed a few years later by the Great Alaska earthquake of 1963 (Mw 9.2) [Lara et al., 2004]. The third-strongest earthquake ever recorded occurred in Indonesia in December 2004 with a magnitude of 9.1, where the Indian plate, an oceanic plate, is subducted beneath the Burma microplate and part of the larger Sunda plate [Lay et al., 2005, Richmond et al., 2006]. It devastated the provinces of surrounding countries, including Sri Lanka, India, and Thailand, making it one of the world's deadliest natural disasters [Satake, 2014]. The fourth strongest megathrust earthquake occurred in northern Honshu, Japan, in March 2011 (Tohoku-Oku earthquake) [Ozawa et al., 2011, Lay, 2018] resulting in the Fukushima nuclear power plant disaster. All of these earthquake generate robust aftershock sequences.

Divergence is accommodated by spreading zones such as mid-ocean ridges or zones of extension like the Italian Apennines, the Basin and Range Province (USA), and the East African Rift [Dobrynina et al., 2017, Thompson and Burke, 1974]. These intraplate fault zones are primarily characterized by an inclined fracture plane along diverging plate boundaries, resulting in a typical normal faulting earthquake sequence. A series of devastating normal fault earthquakes occurred in the central Apennines, including the Colfiorito earthquake in 1997 with magnitudes of Mw 6.0, 5.7, and 5.6, the L'Aquila earthquake in 2009 with a magnitude of Mw 6.3, and Amatrice - Visso - Norcia (AVN) earthquakes in 2016 with magnitudes of 6.5. 6.0 and 5.9 [Chiaraluce et al., 2003, Miller et al., 2004, Terakawa et al., 2010, Gunatilake and Miller, 2022]. The Apennine earthquakes, taken together, generated hundreds of thousands of aftershocks.

Transform motion is accommodated along strike-slip fault systems such as The San Andreas Fault, the North and East Anatolian fault systems, the Southern Alpine fault in New Zealand, and the Great Sumatran fault that incidentally hosts a volcanic arc [Lin et al., 2016, Barnes et al., 2005, Bilham and King, 1989]. Historical destructive earthquakes on these fault systems include the 1856 Fort Tejon earthquake (Mw 7.9), the San Francisco earthquake of 1906 (Mw 7.9), and the 1999 İzmit earthquake sequence near Istanbul Turkey (Mw 7.6) [Evans, 2009, Ellsworth et al., 1981, Karabulut et al., 2011]. Some of the most studied earthquakes include 1992 Joshua Tree (6.7), 1992 Landers (M7.3), and the 1999 Hector Mine earthquake (M7.1) [Miller, 2020, Savage and Svarc, 2009, Bennett et al., 1995, Hauksson et al., 1993]. All of these earthquakes generated rich aftershock sequences.

On the contrary, the 2011 Dalbandin (normal fault) earthquake with M_w 7.2 in Pakistan or the 2013 Saravan earthquake with a Mw 7.7 in Iran generated no aftershocks despite the high magnitudes. These normal-fault earthquakes correspond to the shallow dipping (≈ 0.5–$8°$) Makran subduction in southern Iran, and Pakistan [Burg, 2018]. Another major earthquake that triggered a few aftershocks is the Mw 8.4 strike-slip earthquake in Tibet (2001).

Aftershock sequences are typically evaluated using statistical and empirical laws. In 1894, Omori described that the frequency of aftershocks decreases approximately as a reciprocal of time after the mainshock. The parameter p in Omori's law is the predominant fitting parameter for the thousands of aftershocks of different earthquakes [Omori, 1895], and many empirical fits have been proposed over the last century. Recently it was proposed that the p-value reflects the tectonic ability to recover the co-seismically generated permeability networks [Miller, 2020]. Further empirical laws such as the Gutenberg-Richter or Baths law predict thousands of aftershocks with a statistical distribution [Olsson, 1999, Zhao et al., 2010].

Over the previous decades, numerous approaches have been attempted to understand the earthquake cycle. The most common approach is the stress transfer in earthquake occurrence due to changes in Coulomb failure stress (ΔCFS) [Stein, 1999, Chëry et al., 2001, Cortés-Aranda et al., 2015]. This technique was further advanced to include rate-state friction [Ruina, 1983, Dieterich, 1979]. Although ΔCFS models are widely used, they often find unsatisfying correlations between the locations of aftershocks and stress changes associated with the main earthquake [Miller, 2020]. Statistical models such as ETAS (Epidemic Type Aftershock Sequence) assume that aftershocks can generate their own aftershock sequences. This model yields earthquake production rate comparable with the recorded seismic events [Console et al., 2007, Lombardi et al., 2010]. However, this empirical magnitude-dependent aftershock productivity model currently lacks any physical basis.

An alternative view for understanding earthquake propagation assumes that aftershocks are driven by the diffusion of fluids due to high pore pressure. The importance of fluids in tectonics and earthquake processes has increasingly been recognized over the past years, [Bosl and Nur, 2002, Nur and Booker, 1972, Miller et al., 2004, Terakawa et al., 2020]. Growing evidence suggests that high-pressure fluids play a fundamental role in the earthquake sequence, from swarms [Chiodini et al., 2012, Hauksson et al., 1995] to foreshocks and aftershocks [Podladchikov and Miller, 2013, Miller et al., 2004, Chiodini et al., 2012], and episodic tremor and slip (ETS) that can track the propagation of trapped high-pressure fluid via porosity waves [Podladchikov and Miller, 2013, Shelly et al., 2006, Rogers and Dragert, 2003].

Furthermore, previous studies based on laboratory experiments show that thermal pressurization lubricates frictional interfaces associated with devolitization and highly generates overpressurized fluids [Di Toro et al., 2011]. Numerical thermo-hydro-mechanical-chemical (THMC) models investigate the reaction between a rising melt and a viscous solid through porosity waves coupled with heat transfer. The results indicate a dramatic reduction of effective viscosity upon shear heating, leading to thermal runaway and proving the presence of high-pressure fluid at depth [Bessat et al., 2021]. Furthermore, there is numerical evidence that high-pressure fluids coincide with the degassing of CO_2 from the Earth's mantle as a trigger and driver, for example, the entire 2008 Bohemian earthquake swarm [Heinze et al., 2017a, Parotidis et al., 2003].

In this thesis, I explore, through numerical experiments, links between seismogenesis and the presence or co-seismic generation of high-pressure fluids. Figure 1.1 shows a conceptual model of a fluid-driven earthquake cycle as a timeline for a brittle-ductile lithosphere and is based on seismic, geodetic, geochemical, and laboratory observations. Ubiquitous dehydration of hydrous minerals and decarbonization of carbonate minerals at depth (deep source) generate large amounts of H_2O and CO_2 in the ductile part of the lithosphere. Propagation of this trapped high-pressure fluid from the ductile part into the brittle part of the lithosphere via porosity waves generates pre-earthquake swarms and foreshocks at the base of the brittle crust [Connolly and Podladchikov, 2015]. Foreshocks primarily appear between the brittle and ductile transition zone [Petrillo et al., 2020]. However, once the reservoir at depth reaches its maximum capacity of deep sources, the high-pressure fluids begin to inject into the overlying brittle crust, degrading the crustal strength.

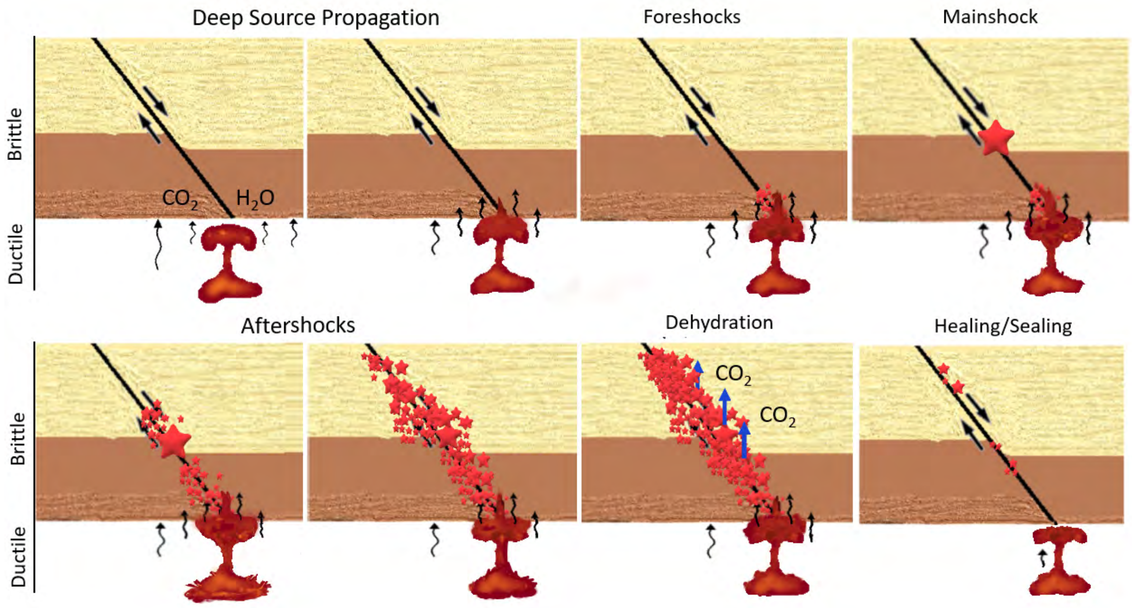

Figure 1.1: Conceptual model of a fluid-driven earthquake cycle shown as a timeline for a brittle-ductile lithosphere. The deep source propagates from the ductile to the brittle part of the lithosphere and produces foreshocks (red dots) in the base of the brittle crust. The high-pressure fluid weakens the crust through reductions in effective normal stress and pore-elastic stresses and causes the mainshock. Dehydration and decarbonization of CO_2 in the fault zone result in more fluid mass and drives the ensuing aftershock sequence observed as CO_2 degassing on the subsurface. Finally, tectonic stresses and chemical precipitation shut down, and the healing process starts (modified after Stephen A. Miller).

The high-pressure fluid weakens the crust by reducing the effective normal stress and inducing pore elastic stresses, leading to the main earthquake [Miller, 2013]. Thermal pressurization at high slip velocities generates more fluid mass through dehydration and decarbonization in the fault zone [Bizzarri and Cocco, 2006, Aharonov and Scholz, 2018], which then diffuses into the surroundings at timescales that depend on the dynamic of permeability structure. The co-seismically generated fractures provide new pathways for the fluid to diffuse both from the fault zone and trapped sources at depth. The post-seismic dynamics of permeability control the earthquake-aftershock decay rates [Miller, 2020]. Thus, high-pressure fluid sources at depth and the additional slip-derived over-pressured fluids drive the entire main and aftershock sequence. Finally, the tectonic relaxation and chemical precipitates shut down the fracture networks created by the earthquake/aftershocks resulting in the healing of the permeability networks.

An excellent example of the conceptual model (Figure 1.1) is found in the central Apennines in Italy. A series of earthquakes starting in 1997 and ending in 2016 ruptured nearly 200 km. These includes the Colfiorito earthquakes in 1997, the 2009 L'Aquila earthquakes, and the 2016 AVN earthquakes, which occurred in the Carbonate Apennines and exhibited foreshocks, and mainshocks, followed by aftershocks with many events of M>5 [Michele et al., 2020, Moschella et al., 2021]. The Apennines host an abundance of mantle-derived CO_2 due to ongoing subduction [Frezzotti et al., 2009]. Furthermore, geochemical evidence indicates that the area of the 2009 L'Aquila earthquakes releases approximately 500 t/day of deeply derived CO_2, suggesting the presence of deep pressurized fluid pockets and deep degassing associated with this event [Chiodini et al., 2011]. These findings are consistent with the 1997 Colfiorito earthquake, where high-pressure fluid was shown to drive the entire aftershock sequence [Miller et al., 2004]. Further seismic activities provided evidence of fluid-driven events; for example, in 1989, in the Alban Hills near Rome, Italy, where Lake Albano had significant concentrations of dissolved CO_2 associated with sublacustrine fluid discharges fed by a pressurized CO_2-rich reservoir [Chiodini et al., 2012]. Therefore, many lines of evidence strongly suggest that high-pressure fluid propagation is an integral part of the earthquake process. These findings open a whole new perspective to understanding the importance of the role of fluid in seismogenesis. The conceptual model presented above opens new research avenues and provides a new context for searching for precursor signals of large earthquakes. In this thesis, I explore this potentially significant contribution and propose a physical model that accounts the co- and postseismically generated permeability networks and the internal generation of CO_2 by thermal decomposition leading to trapped high-pressure fluid in the lithosphere [Gunatilake and Miller, 2022]. This thesis aims to provide a physical model capturing foreshocks, mainshocks, and the numerous aftershocks with numerical modeling representing both deeply and internally generated CO_2 through decarbonization by including a source term. In addition, the model considers the tectonic ability to heal the permeability networks and constrain the temporal evolution of source generation. Finally, we simulate the measured aftershock sequences and compare them with observations in both space and time.

1.1 Outline of the thesis

The remainder of this thesis is divided into five main chapters. Chapter 2 derives and describes the fundamental theories and equations used within this thesis and aims to familiarize the reader with the propagation of a fluid in a porous medium, considering linear elasticity, which describes reversible deformation, and plasticity, which describes irreversible deformation. I present the mathematical formulation of the non-linear diffusion equation and highlight the importance of permeability dynamics and the source term that is essential to understanding aftershock propagation and its healing. Chapter 3 focuses on the carbonate-rich Apennines sequence and is a published manuscript in the Journal of Geophysical Research: Solid Earth titled 'Spatio-temporal complexity of aftershocks in the Apennines controlled by permeability dynamics and decarbonization.' The non-linear diffusion model with a source term reproduces the Amatrice-Visso-Norcia (AVN) earthquake sequence in the Apennines (Italy). The source term, representing co-seismic decarbonization, is essential to match the data, providing empirical evidence that internally generated fluid sources (e.g., decarbonization/dehydration) are necessary for aftershock sequences displaying non-Omori type behavior. Chapter 4 introduces a 3-dimensional numerical model of non-linear diffusion with source term to evaluate the spatial distribution of evolving high-pressure fluid. In this work, I consider the 2009 L'Aquila (M_w 6.3) and the 2016 Amatrice-Visso-Norcia (M_w 6.5) earthquake sequences. At first glance, these two earthquake sequences appear to overlap, but a closer look reveals that the AVN sequence filled a seismic gap, with three severe events of $M_w > 5$ and hundreds of aftershocks between the 2009 L'Aquila sequence and the 2016 AVN sequence. This finding supports our working hypothesis that earthquakes are predominantly driven by an internal fluid generation that activates various fault systems. This work aims to quantify the stimulated region/volume by internal fluid with the onset of the 2016 AVN and the 2009 L'Aquila sequence, identify the relationship between both sequences, and reproduce the temporal and hypocentral evolution of the recorded seismic data.

Chapter 5 extends the model to quantify the influence of fluid and heat transport from a geothermal perspective. This manuscript is under review in the Journal of Nature Communications Earth and Environment titled 'Dynamics between earthquakes, volcanic eruptions, and geothermal energy exploitation in Japan.' Active volcanoes provide a rich geothermal energy source since the intruding magma causes steep geothermal gradients, thus allowing for harvesting large amounts of heat for geothermal exploitation. Heat is harvested by multiple geothermal power plants in the vicinity of the Aso volcanic system in southern Japan, which last erupted in October 2021. This paper examines the interplay between the penultimate eruption of the Aso volcano in 2016, the associated numerous seismic events known as the Kumamoto sequence, and their influence on the local geothermal power plants. Using a non-linear advection/diffusion model of pore pressure and heat flow combined with simplified mechanics, the modeling results show evidence for strong coupling between earthquake activity and volcanic eruptions and good spatial and temporal correlation between modeled earthquake locations and aftershock decay rates along the entire sequence.

Chapter 6 is a manuscript submitted to Nature Scientific Reports (revision under review) titled 'Adapting a physical epidemic-type aftershock model to simulate the spread of COVID19'. This paper presents the results of a numerical model for the spread of COVID19 based on non-linear pressure diffusion in porous media. The model was initially developed for simulating earthquake aftershock sequences and provided a mechanistic explanation for Omori's Law and the often-used (statistical) Epidemic Type Aftershock Sequence (ETAS) model. We reformulated the physical equations to calculate infection pressure diffusion and show that the COVID pandemic propagates through an analogous porous media. This quantitative and deterministic model matches the cumulative number of COVID19 cases for 12 countries (studied to date) and the city of Melbourne, Australia, to demonstrate that the model scales. Chapter 7 summarizes these findings and outlines possible future research directions.

Chapter 2

Background

2.1 Earthquake Physics

The definition of 'aftershocks' is widely used in earthquake physics, and describes all the earthquakes that follow the largest magnitude earthquake of the sequence. But this definition can be transient. If a large earthquake occurs, all events preceding it are called foreshocks, and all subsequent earthquakes are called aftershocks. Occasionally, an aftershock is even larger than the previous mainshock, in which case the previous mainshock is renamed to a foreshock, the new larger earthquake designated the mainshock, and all subsequent events called aftershocks.

A few empirical laws characterize earthquake sequences, including Gutenberg-Richter (GR) frequency-size statistics and Omori's Law of the temporal decay of aftershocks. Gutenberg–Richter describes the relationship between the magnitude and number of earthquakes in a region in a given period and is written as:

$$log_{10}N = a - bM, \tag{2.1}$$

where N is the cumulative number of earthquakes recorded in the region over a certain timescale, and M is the magnitude of those events. The declining power-law scale means ten times fewer earthquakes per unit of magnitude. The b parameter characterizes the slope of the straight line in logarithmic space and is often close to 1. The a parameter is a constant determined by the total number of events. For example, if one magnitude 9 earthquake occurs, GR predicts ten M=8, one hundred M=7, one thousand M=6, etc.

Omori's Law, proposed in 1894 and later appended to the Omori-Utsu Law, states that aftershock frequency decays as an inverse power law in time. Omori's law is one of the fundamental empirical laws and is widely used to analyze seismic data. The modified Omori's law describes the frequency of earthquakes after the main shock and states that the rate of aftershocks decrease hyperbolically with time:

$$N(t) = \frac{K}{(t+c)^p}, \tag{2.2}$$

where N is the number of earthquakes as a function of time t following the mainshock, K is the aftershock productivity, and c and p are empirical constants. The c value relates describes the time lag until Omori behavior, but it difficult to measure because immediate aftershocks get drown in the seismic record. The exponent p determines how fast the aftershock rate decreases with time and often has a value close to 1.0 [Enescu et al., 2009, Utsu et al., 1995]. Miller (2020) recently proposed that the p-value is a measure of tectonic stress state available to heal co-seismically generated permeable fracture networks. This is discussed in detail throughout this thesis.

The empirical Båth's law predicts the expected size of the potentially most destructive aftershock that follows a mainshock and claims that the average difference in magnitude between a mainshock and its largest aftershock is 1.2, regardless of the mainshock magnitude. Mathematically, Bath's law is expressed as:

$$\Delta m \approx \frac{1}{b} \log_{10} \left(N/N_{\text{aft}}\right), \tag{2.3}$$

where Δm is the differences in magnitude between mainshocks and their largest aftershocks, b is a constant, N and N_{aft} is the cumulative number of earthquakes and aftershocks.

Apart from these empirical laws, the space-time distribution of aftershocks can be described by various physical mechanisms. Hydraulic and mechanical interactions play an essential role in aftershock genesis [Nur and Byerlee, 1971, Scholz, 2019]. At a specific range of temperature and pressure, usually at depths below 800 m, CO_2 is supercritical, and behaves as a highly compressible fluid. It is stored as a high-pressure fluid in the pores of sedimentary rocks [Pruess, 2003]. From a geodynamic perspective, the fluid is confined by preexisting faults and other impermeable lithological structures. Once the high-pressure fluid starts to migrate along faults with lower permeability, it activates these faults, triggers seismicity due to increased pore-pressure [Miller et al., 2004] and controls the space-time evolution of numerous aftershocks [Di Luccio et al., 2010]. The rise of fluid pressure reduces the Coulomb stress and, therefore, to a regional poro-elastic stress evolution. The reduction of fault strength, shear stress accumulation, and fluid pressure facilitates the rupture of faults and can cause thousands of aftershocks.

2.2 Diffusion of Fluid Pressure

The relative amount of fluid in a porous media is defined by the ratio of fluid volume V_f $[m^3]$ and the total volume V $[m^3]$ of the media. The ratio of fluid volume and available pore space is also called saturation S $[-]$ of the porous medium and is mathematically written as:

$$\Theta = \frac{V_f}{V} \quad , \quad S = \frac{\Theta}{\phi}, \tag{2.4}$$

where Θ is relative volumetric water content, and ϕ is $[-]$ porosity.

Fluid flow through a porous media is described by Darcy's law [Darcy, 1856]. The flux discharge per unit area q $[m/s]$ can be best explained using a simple example of a sand column filled with water at the top and propagating downwards through the porous sandbox. It can be given by the proportional relation between the discharge rate Q $[m^3/s]$ through the cross-sectional area of the flow A $[m^2]$.

$$\frac{Q}{A} = q = -\frac{\kappa \rho g}{\eta} \frac{h_1 - h_2}{L}, \tag{2.5}$$

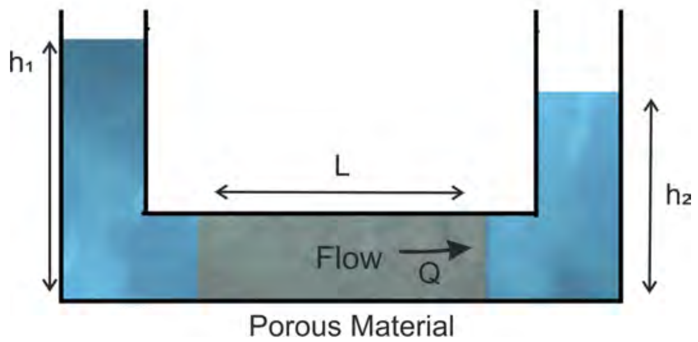

where Q $[m^3/s]$ is the volumetric flow rate, A is $[m^2]$ the cross-sectional area of the flow, h_1 $[m]$ the height of upstream water column, h_2 $[m]$ the height of the downstream water column, L $[m]$ the length of the sandbox, ρ water density $[kg/m^3]$, g gravitational acceleration $[m/s^2]$, η fluid viscosity $[Pas]$ and intrinsic permeability of the medium κ $[m^2]$. Flux q $[m/s]$ is a product of the flow resistance of the rock or soil κ, the inverse of the viscosity of the fluid μ as a measure for the internal resistance of the liquid, and the pressure drop over a given distance. Switching from water column height to pressure P $[Pa]$, the flux q $[m/s]$ can be expressed as

$$q = -\frac{\kappa}{\mu} \nabla P. \tag{2.6}$$

Finally, fluid velocity v $[m/s]$ is related to Darcy flux q and effective porosity ϕ accounting for the total volume available for fluid flow

$$v = \frac{q}{\phi}. \tag{2.7}$$

The conservation of mass of a fluid in porous media is governed by the balance of incoming and outgoing fluxes and the temporal change of the mass inside the control volume $M_{inside} = M_{in} - M_{out}$. As the flux difference is equal to the gradient of the Darcy velocity, the conservation of mass can be mathematically expressed as:

$$\frac{d\phi\rho}{dt} = -\rho\nabla\vec{q} + Q, \tag{2.8}$$

where Q is the source/sink term reflecting addition or removal of fluid mass within the respective volume. The temporal change on the right hand side of the equation above can be split into a change of fluid density and pore space using standard mathematical derivation laws, such as chain rule:

$$\phi\frac{d\rho}{dt} + \rho\frac{d\phi}{dt} = -\rho\nabla\vec{q} + Q. \tag{2.9}$$

Various processes, such as thermal expansion or contraction, can change porosity over time. These processes make porosity a function of various variables, such as temperature T $[K]$, salinity concentration S $[kg/m^3]$, and pressure P:

$$\frac{d\phi(P,T,S)}{dt} = \frac{\partial\phi}{\partial P}\frac{\partial P}{\partial t} + \frac{\partial\phi}{\partial T}\frac{\partial T}{\partial t} + \frac{\partial\phi}{\partial S}\frac{\partial S}{\partial t}. \tag{2.10}$$

A similar formulation can be made for the fluid density $\rho(T,P,S)$:

$$\frac{d\rho(P,T,S)}{dt} = \frac{\partial\rho}{\partial P}\frac{\partial P}{\partial t} + \frac{\partial\rho}{\partial T}\frac{\partial T}{\partial t} + \frac{\partial\rho}{\partial S}\frac{\partial S}{\partial t}. \tag{2.11}$$

Assuming only very slight changes in temperature and salinity concentration, we can neglect the porosity and fluid density dependence on these components. However, the change of a volume of a medium to applied pressure is described by the compressibility β, which results in changes in porosity and density over time. Therefore the fluid and pore compressibility can be written as:

$$\beta_\phi = \frac{1}{\phi}\frac{\partial\phi}{\partial P}, \tag{2.12}$$

$$\beta_\rho = \frac{1}{\rho}\frac{\partial\rho}{\partial P}. \tag{2.13}$$

Considering these components, the right-hand side of the conservation of mass can be rewritten in the following form:

$$\rho\frac{d\phi}{dt} + \phi\frac{d\rho}{dt} = \rho\phi\left(\beta_\phi + \beta_\rho\right)\frac{\partial P}{\partial t}. \tag{2.14}$$

The gradient of the flux $\nabla\vec{q}$ is given by the empirical Darcy's law as described above and is accounted for in the conservation of mass as:

$$\rho\phi(\beta_\phi + \beta_\rho)\frac{\partial P}{\partial t} = \rho\nabla\left(\frac{k}{\eta}\nabla P\right) + Q. \tag{2.15}$$

The density can be dropped, as it is on both sides of the equation, and finally, the non-linear Pressure diffusion equation in the absence of gravitational effects can be written as:

$$\frac{\partial P}{\partial t} = -\frac{1}{\phi\beta}\nabla\left(\frac{\kappa}{\mu}\nabla P\right) + \frac{Q}{\phi\beta}. \tag{2.16}$$

2.3 Poro-elastic Stresses

High-pressure fluid diffusion can result in the deformation of a solid body. Therefore, the well-known Newton's law $F = m \cdot a$ is the basis for a stressed body. In solid body mechanics, pressure P is a force F vertical to the surface A: $P = F/A$ $[N/m^2 = Pa]$. In solid body mechanics, the concept of stress σ is based on a similar definition of acting force per area $\sigma = F/A$ $[N/m^2 = Pa]$. However, the stress calculations incorporate multiple components due to the presence of multiple surfaces and possible directions, not only the vertical component. Normal stress is vertical to the respective surface σ_{ii} and shear stress is parallel to a surface τ_{ij}, with $i, j = x, y, z$. In two dimensions, the Cauchy stress tensor is written as:

$$\sigma = \begin{bmatrix} \sigma_{\mathrm{xx}} & \tau_{\mathrm{xy}} \\ \tau_{\mathrm{yx}} & \sigma_{\mathrm{yy}} \end{bmatrix} \tag{2.17}$$

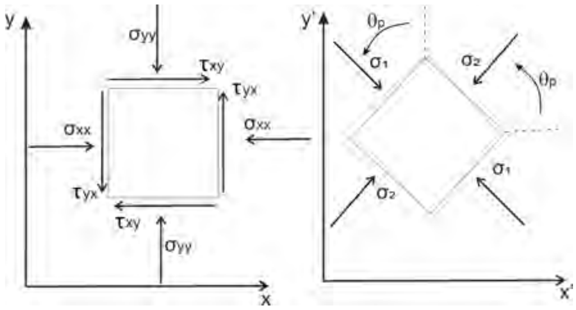

Figure 2.1: Any state of the Cauchy stress tensor σ_{ii}, τ_{ij} can be transformed by rotation into the directions of principal stresses $\sigma_{1,3}$.

Therefore, the mean stress can be calculated with

$$\sigma_{\mathrm{m}} = \frac{\sigma_{\mathrm{xx}} + \sigma_{\mathrm{yy}}}{2}. \tag{2.18}$$

The maximum and minimum stresses known as the principle stresses are derived from the rotation of the Cauchy stress tensor at an angle on a plane where shear stress is zero. The angle θ_p, where the shear stress τ_{xy} becomes zero, can be derived with

$$\tan 2\theta_p = \frac{2\tau_{xy}}{\sigma_{xx} - \sigma_{yy}}. \tag{2.19}$$

Respectively σ_1, σ_2 are calculated as

$$\sigma_{1,2} = \frac{\sigma_{xx} + \sigma_{yy}}{2} \pm \sqrt{\left(\left(\frac{\sigma_{xx} - \sigma_{yy}}{2}\right)^2 + \tau_{xy}\right)^2}. \tag{2.20}$$

Finally, Newton's law can be reformulated for solid body mechanics accordingly.

$$\frac{\partial \sigma_{ij}}{\partial x_j} = \rho \cdot \frac{\partial^2 u_i}{\partial t^2}, \tag{2.21}$$

where σ_{ij} is an element of the Cauchy stress tensor, ρ $[kg/m^3]$ is the density of the rock, u is the displacement and t $[s]$ is time. The indexes i and j indicate the directions in a two-dimensional plane, respectively, x and y direction in a Cartesian coordinate system. Using the relationship between displacement u and velocity v, the elastic deformation can be calculated in two dimensions as

$$\begin{aligned} \frac{\partial v_x}{\partial t} &= \frac{1}{\rho} \cdot \left(\frac{\partial \sigma_{xx}}{\partial x} + \frac{\partial \sigma_{xy}}{\partial y}\right), \\ \frac{\partial v_y}{\partial t} &= \frac{1}{\rho} \cdot \left(\frac{\partial \sigma_{xy}}{\partial x} + \frac{\partial \sigma_{yy}}{\partial y}\right). \end{aligned} \tag{2.22}$$

The relationship between the stress $\sigma_{i,j}$ and strain $\varepsilon_{i,j}$ is based on Hooke's law using the elasticity tensor D_{ijkl}

$$\sigma_{ij} = D_{ijkl} \cdot \epsilon_{kl}, \tag{2.23}$$

which is valid if the deformation of a solid body is reversible. The strain ε in solid mechanic can be divided into normal and shear strain:

$$\varepsilon_{\mathrm{xx}} = \frac{\Delta S}{S} = \frac{\partial u_{\mathrm{x}}}{\partial x}, \ \varepsilon_{\mathrm{yy}} = \frac{\Delta L}{L} = \frac{\partial u_{\mathrm{y}}}{\partial y}, \tag{2.24}$$

$$\varepsilon_{\mathrm{xy}} = \frac{\Delta S}{L} = \frac{1}{2}\left(\frac{\partial u_{\mathrm{y}}(x,t)}{\partial x} + \frac{\partial u_{\mathrm{x}}(x,t)}{\partial y}\right). \tag{2.25}$$

Thus, the volumetric strain ε_{V} is defined as

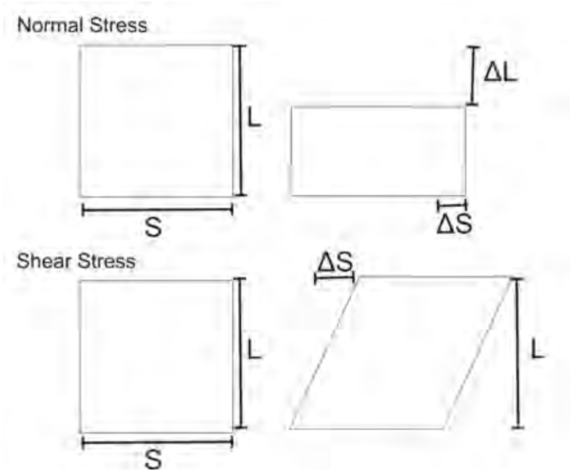

Figure 2.2: Schematic diagram showing normal and shear stresses.

$$\varepsilon_{\mathrm{V}} = \frac{\varepsilon_{\mathrm{xx}} + \varepsilon_{\mathrm{yy}}}{2}. \tag{2.26}$$

The principal strain is defined in the direction of the principal stresses, and the Young's modulus E $[Pa]$ quantifies the relationship between axial (normal) stress σ and axial strain ε in the linear elastic region of a material:

$$E = \frac{\sigma_{\mathrm{yy}}}{\varepsilon_{\mathrm{yy}}}, \tag{2.27}$$

while the Poisson ratio ν describe the deformation of the rock perpendicular to the direction of loading:

$$\nu = \frac{\varepsilon_{\mathrm{xx}}}{\varepsilon_{\mathrm{yy}}}. \tag{2.28}$$

The resistance of rock to a certain compression is described by the bulk modulus K

$[Pa]$ and is defined as the ratio of the infinitesimal stress to the resulting relative decrease of the volume V

$$K = V\frac{\Delta\sigma_{\mathrm{m}}}{\Delta V}. \tag{2.29}$$

Furthermore, the shear modulus γ is a measure of the elastic shear stiffness of the rock and is defined as the ratio of shear stress to the shear strain:

$$\gamma = \frac{\sigma_{xy}}{\varepsilon_{xy}}. \tag{2.30}$$

Accordingly, the Lame constant is a material constant that depends on the resistance and stiffness of the rock:

$$\lambda = K - \frac{2}{3}\gamma. \tag{2.31}$$

Finally, the elasticity tensor D_{ijkl}, assuming that the strain of deformation is zero in one dimension, can be written as follows:

$$\underline{D}\begin{bmatrix} \lambda + 2\gamma & \lambda & 0 \\ \lambda & \lambda + 2\gamma & 0 \\ 0 & 0 & 2\gamma \end{bmatrix}$$

Therefore the dynamic behavior of the stresses during deformation can be written as

$$\begin{aligned} \frac{\partial\sigma_{xx}}{\partial t} &= (\lambda + 2\gamma)\cdot\frac{\partial v_x}{\partial x} + \lambda\cdot\frac{\partial v_y}{\partial y}, \\ \frac{\partial\sigma_{yy}}{\partial t} &= (\lambda + 2\gamma)\cdot\frac{\partial v_y}{\partial y} + \lambda\cdot\frac{\partial v_x}{\partial x}, \\ \frac{\partial\sigma_{xy}}{\partial t} &= \gamma\cdot\left(\frac{\partial v_x}{\partial y} + \frac{\partial v_y}{\partial x}\right). \end{aligned} \tag{2.32}$$

If the deformation of rocks due to the fluid pressure is irreversible, it is called plastic deformation. When strain reaches the maximum amount of elastic deformation, it is followed by plastic deformation. The yield function f contains yield criteria. Whenever $f < 0$, the rock behaves elastically. When $f = 0$, the rock is in its plastic stage and has reached its' yield point'. The most common failure criteria are the Mohr-Coulomb failure criteria:

$$f = \tau - \sigma_n \cdot \sin\phi - c\cdot\cos\phi, \tag{2.33}$$

where τ is the shear stress, σ_n is the normal stress, ϕ $[^\circ]$ is the angle of internal friction, and c $[Pa]$ is the cohesion. Cohesion and angle of internal friction are material properties. The criteria can be reformulated for defining a critical state of shear and normal stress for $f = 0$

$$|\tau| = c + \mu\sigma_n, \tag{2.34}$$

where μ is the coefficient of internal friction as another representation of the angle of internal friction.

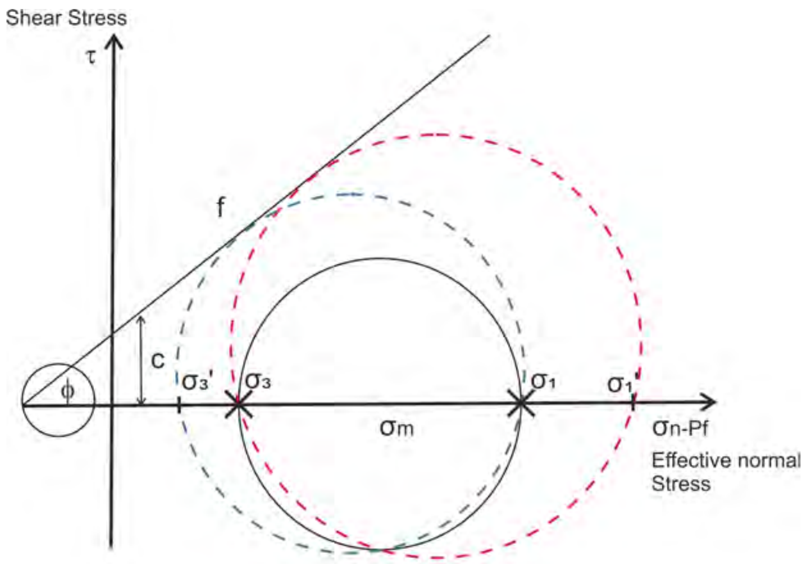

Figure 2.3: Mohr's circle as representation of possible stress states and the Mohr Coulomb failure criteria defining critical combinations of shear and normal stress causing failure.

Figure 2.3 shows a Mohr-Coulomb failure envelope for a two-dimensional environment. Mohr's stress circle represents every possible combination of normal and shear stress at all angles for a specific stress state of a point defined by the principal stresses. Hence, the Mohr-Coulomb theory provides an easy way to express the multiaxial stress state by using Mohr's circles, where σ_1 and σ_3 are the maximum and minimum principal stresses. The failure criterion can be reached by increasing σ_1 (red dashed circle), decreasing σ_3 (blue dashed circle), or increasing the fluid pressure. The influence of fluid pressure on the mechanical stress state of the porous media is expressed using the 'effective stress' following Terzaghi is:

$$\sigma_{\text{eff}} = \sigma_{\text{n}} - \alpha P, \tag{2.35}$$

where α is the Biot coeff with a maximum value of 1. The typical value of α for rocks is usually close to 1, so α is often neglected for geoscience applications in solid porous rocks. Including the effect of pore pressure, P, the Mohr-Coulomb failure criteria become:

$$|\tau| = c + \mu(\sigma_n - P). \tag{2.36}$$

The effective normal stress and shear stress acting on a plane is defined as:

$$\sigma_n = \frac{\sigma_1 + \sigma_3 - 2P}{2} \cdot \cos(2\theta) \tag{2.37}$$

$$\tau = \frac{\sigma_1 + \sigma_3}{2} \cdot \sin(2\theta) \tag{2.38}$$

where θ is the angle measured from the normal to the σ_1 plane and indicates the optimally oriented failure plane, in other words, θ is the plane's orientation where minimum fluid pressure is needed to trigger a failure and where the shear stress is already maximum and the normal stress minimum.

2.4 Diffusion and Advection of Heat

The heat transport is mathematically described by an advection-diffusion equation, similarly to fluid pressure diffusion. The derivation of this equation is based on the conservation of energy:

$$E = m \cdot C_p \cdot T, \tag{2.39}$$

where E is energy [J], m is mass [kg], C_p specific heat capacity [$J/kg°C$] and T the temperature [$°C$]. Considering the conservation of energy in a volume V with $m = V \cdot \rho$, the energy per unit volume e and its time derivative can be rewritten as

$$\begin{aligned} e = \frac{E}{V} &= \rho C_p T, \\ \frac{\partial e}{\partial t} &= \rho C_p \frac{\partial T}{\partial t}, \end{aligned} \tag{2.40}$$

assuming that only temperature changes with time, changes in density and heat capacity can be neglected. The temporal change of temperature depends on the difference between in- and outgoing heat flux $\nabla \vec{J}$ and the heat generated Q

$$\frac{\partial T}{\partial t} = -\vec{\nabla} \vec{J} + Q. \tag{2.41}$$

The total flux $\vec{J}$ is defined as the sum of advective and conductive contributions:

$$\vec{J} = \vec{J}_{cond} + \vec{J}_{adv}, \tag{2.42}$$

where $\vec{J}_{cond}$, considering Fick's law, relates the diffusive flux to the temperature gradient T

$$\vec{J}_{cond} = -\lambda \vec{\nabla} T, \tag{2.43}$$

where λ is thermal conductivity. The addictive flux $\vec{J}_{adv}$ is further written as:

$$\vec{J}_{adv} = \vec{q} \cdot \rho c_p T, \tag{2.44}$$

where $\vec{q}$ is the transport velocity. Advection is the dominant heat transport process in systems with high flow velocities. The heat conservation equation becomes a temperature advection-diffusion equation:

$$\frac{\partial T}{\partial t} = \frac{\lambda}{\rho c_p} \vec{\nabla}^2 T - \vec{q} \cdot \vec{\nabla} T + \frac{Q}{\rho c_p}. \tag{2.45}$$

2.5 Thermal Stresses

A body can change its shape and volume due to temperature changes, just like a porous body changes due to pore pressure changes. These changes are called thermal strain ϵ_T and are expressed as [Jaeger et al., 2009]:

$$\epsilon_T = \alpha \Delta T, \tag{2.46}$$

where α is the coefficient of linear thermal expansion, and ΔT is the temperature difference. If the deformation of the body is limited, the strain will result in thermal stress:

$$\sigma_T = C \cdot \epsilon_T, \tag{2.47}$$

where C is the elastic stiffness of the rock. Based on Young's modulus and Poisson ratio described in the previous chapter, we can simplify the thermal stress:

$$\sigma_{T_{ij}} = \frac{E}{1 - 2v} \cdot \alpha \Delta T \delta_{ij}, \tag{2.48}$$

with Kronecker delta δ_{ij} [Jaeger et al., 2009]. This resulting equation means higher thermal stress changes with larger temperature changes. We achieve compressional deformation when thermal stresses are positive and relative tension when the temperature difference is negative. The magnitude of thermal stress depends on the material and can widely change.

2.6 Permeability - Porosity Relationship

In geological settings, permeability as a rock property is directly linked to effective porosity and varies widely in heterogeneous rocks. It represent the ability of fluid to flow though a porous media and is a major factor to describe the development of aftershocks and therefore the dominant flow path. Permeability and porosity are critical parameters of the host rock as they control the fluid diffusivity. Similar to other fluid properties, such as viscosity, the porosity and permeability are known to be dependent on state variables. To account for those dynamic changes, various models have been developed over the years. In a very prominent, model permeability solely depends on stress and pressure [Carcione and Tinivella, 2001, Rutqvist et al., 2002, Latham et al., 2013, Bai et al., 1997, Min et al., 2004]. A purely pressure dependent model is presented by Rutqvist et al. (2002), which links the permeability response on pressure to changes in porosity

$$\begin{aligned} \phi &= \phi_{res} + (\phi_{in} - \phi_{res}) \cdot \exp\left(a \cdot (\sigma_m - P)\right) \\ k &= k_{in} \cdot \exp\left(c \cdot (\phi/\phi_{in} - 1)\right), \end{aligned} \tag{2.49}$$

with initial and residual values of permeability and porosity and two constants, a and c. Different studies (e.g. [Miller et al., 2004, Carcione and Tinivella, 2001]) use an exponential function of permeability in dependence of the normal stress σ_n.

$$k = k_0 \cdot \exp\left(-\frac{\sigma_n}{\sigma_0}\right) \tag{2.50}$$

where k_0 is permeability at zero stress, σ_0 is a scaling constant, and σ_n incorporates the normal stress on a potential fault plane of dip angle θ as shown in eq. 2.37.

Another permeability model that depends on temperature and pressure is presented by [Guo et al., 2017] and written as

$$\kappa = \kappa_0 e^{-3C_t\beta\left(T + \frac{P_w - \eta P_n - \sigma_0}{\beta}\right)}, \tag{2.51}$$

where C_t is the rock compressibility.

The effective stress σ_{eff} known as the Duhamel-Neumann approach depends on pressure and temperature

$$\sigma_{eff} = (P_w - \eta P_n) + \beta T, \tag{2.52}$$

where P_w and P_n are confining and pore pressures, respectively, and η is effective stress coefficient, T is temperature and β is thermal stress coefficient, which is derived from the following dependence: $\beta = a_T E/(1-2\nu)$, where a_T is the average thermal expansion coefficient, E is the average elastic modulus, and ν is Poisson's ratio. While porosity is further defined as:

$$\varphi = \varphi_0 \mathrm{e}^{-C_t\left(\sigma_{eff}-\sigma_0\right)} \tag{2.53}$$

All these models do not distinguish between intact and fractured permeability dynamics. In general, the permeability of fractures is higher than that of the surrounding rock and increases co-seismically due to sudden slip of existing fractures and or newly created fractures by an earthquake [Mitchell and Faulkner, 2008]

Miller (2020) presents a time-dependent permeability model that considers several additional components crucial during an aftershock sequence. First, it considers the exponential dependence of permeability on effective normal stress, similarly to the model previously shown. The pre-failure permeability is expressed as

$$k = k_o \exp\left[-\sigma_e/\sigma^*\right], \tag{2.54}$$

where k is permeability, k_o is the permeability at zero stress, σ_e is effective normal stress, τ is shear stress, μ is friction coefficient, P is pore pressure, and σ_0 constrains the permeability response to σ_e. Second, the model considers the increase in permeability by orders of magnitude in pre-existing frictional interfaces and the newly developed fracture network during slip. Third, it also considers the exponential decrease in permeability with time, reflecting the healing/sealing of the permeability network after an earthquake. Hence, the permeability after failure is

$$k = (k_o + \mathrm{d}\cdot\exp(-\alpha t))\exp\left[-\sigma_e/\sigma^*\right], \tag{2.55}$$

where d is the co-seismic step-increase in permeability at slip $[m^2]$, α $[s^{-1}]$ reflects permeability recovery over the timescale of t $[s]$, which plays a dominant role in this study. Once a fault or fracture reaches a critical stress state - e.g., defined by the Mohr-Coulomb failure criteria - and slips, its permeability increases significantly, here expressed through d. Mechanical or chemical processes can cause the decrease of permeability over time, expressed through the value α. As mentioned above, a mainshock does not always come along with thousand of aftershocks. In a geological setting that inherits and generates a large amount of high-pressure fluid and therefore generates many aftershocks, the system requires a long time until the initial permeability state has been recovered. If the geological setting has a less vigorous fluid generation, e.g., by thermal decomposition, the initial permeability state is more rapidly recovered. On the other hand, in a geological setting without fluid presence or generation and therefore none to very few aftershocks, the permeability state barely changes after the mainshock.

2.7 Numerical Model

The equations presented in the section above are too complex to be solved analytically. Therefore, a numerical approximation is implemented to obtain solutions in complex geological settings. Various computational approaches simulate pore pressure diffusion in fractured porous media, such as dual-porosity, discrete fracture networks, or effective porous media. The underlying idea of a dual-porosity model is separating a fractured porous medium into two domains with opposite characteristics, namely fractures and the porous matrix itself [Zyvoloski et al., 2008, Di Donato and Blunt, 2004]. Usually, the permeability of the porous matrix is much smaller than that of the fractures. The mass exchange between the fracture network and the matrix is included based on the pressure difference between the two domains and requires additional assumptions about the fracture network geometry The discrete fracture network refers to a computational model that explicitly represents the geometrical properties of each individual fracture (e.g., orientation, size, position, shape, and aperture) and the topological relationship between individual fractures and fracture sets [Cacas et al., 1990, Lei et al., 2014]. Such models require a large number of parameters and information about the underground structure, which are usually not available and need to be approximated, e.g., through statistical methods.

A straightforward approach is the approximation of an effective porous media. In an effective porous media, there is no specific difference between fractures and porous matrix, as the fractures are simply considered as part of the matrix, and the overall volume is assigned a macroscopic quantity for porosity, and permeability [Dong et al., 2019]. The benefit of this approach is its low demand on parameters, and the required effective parameters can often be well estimated in the field, e.g., through pumping tests. However, as fractures are not resolved explicitly, it is most suitable for relatively coarse numerical models in which not explicit fractures but rather faults with various smaller fractures are considered.

The numerical scheme used in this work to calculate the pore pressure changes and temperature diffusion and advection is an implicit finite difference scheme with Gaussian elimination and LU-factorisation. The implicit finite difference scheme can be explained based on the time-dependent heat equation:

$$\frac{\partial T}{\partial t} = \kappa \frac{\partial^2 T}{\partial x^2}, \tag{2.56}$$

where the temperature derivation is evaluated at the new timestep as

$$\frac{T_i^{n+1} - T_i^n}{\Delta t} = \kappa \frac{T_{i+1}^{n+1} - 2T_i^{n+1} + T_{i-1}^{n+1}}{\Delta x^2} \tag{2.57}$$

Hence, the aim is to solve a linear system of equations. The Gaussian elimination optimizes the implied matrix multiplications. Resulting in a linear system of equations $Ax = b$ with the inverse Matrix x = A[1]b. The Gaussian transformation lead to $A'x = b'$. It is computationally more efficient to store the transformation of the Gaussian elimination using matrix factorization. Therefore, the general matrix A is written as the product of two-factor matrices $A = LU$ with the lower triangular matrix L and an upper triangular matrix U.

The numerical model was implemented in Matlab, aiming to solve the non-linear diffusion of pressure, advection/diffusion of heat, and brittle mechanics. The fractional step method with an implicit finite difference scheme with Gaussian elimination and LU-factorisation provides the model results presented in this work.

Chapter 3

Spatio-temporal complexity of aftershocks in the Apennines controlled by permeability dynamics and decarbonization

Published in Journal of Geophysical Research: Solid Earth (Gunatilake and Miller, 2022)

3.1 Abstract

In 2016, a series of large normal faulting earthquakes in the Apennines filled the seismic gap between the 1997 Colfiorito and 2009 L'Aquila earthquakes. These earthquakes, known as the Amatrice-Visso-Norcia (AVN) sequence, spawned hundreds of thousand of aftershocks in the first year, extending about 60 km along strike. The Colfiorito and L'Aquila aftershocks showed a significant high fluid-pressure component in their aftershock genesis, and we show evidence that the AVN aftershocks also include a significant high pressure CO_2 component. This CO_2 is both deeply-derived, and internally generated by thermal decomposition. Using a simple model of non-linear diffusion with a source term, we compare model results with the observed cumulative number of aftershocks, and also spatial comparisons between the calculated fluid pressure and the hypocenters of about 35,000 well-located events. The good comparisons between model and observations provide evidence that the AVN sequence includes a contribution (additional fluid source) from co-seismic decarbonization. Our results suggest that internal fluid generation through devolitization or decarbonization is responsible for non-Omori type aftershock behavior such as observed for the AVN sequence and for the 2011 M_w 9.1 Tohoku (Japan) and the 2014 Iquique (Chile) M_w 8.2 megathrust subduction zone earthquakes.

Keywords: Apennines earthquakes; Amatrice-Visso-Norcia sequence; fluid-driven aftershocks; thermal decomposition; Mathematical, physical, and numerical modeling; Non-linear fluid-pressure diffusion with source term.

Keypoints

- Amatrice-Visso-Norcia (AVN) earthquakes sequence modeled as a fluid-pressure diffusion process with a source term.
- Model shows that this sequence is driven by deeply-derived and co-seismically generated CO_2 through thermal decomposition.
- Good spatial and temporal agreement for all depth profiles between modelled and well-located aftershocks of about 35,000 events.

3.2 Plain-Language Summary

The 2016 Amatrice-Visso-Norcia (AVN) earthquake sequence (Italian Apennines) spawned hundreds of thousands of aftershocks in the first year. In this work, we show using a physical and numerical model that the aftershocks are generated by high pressure CO_2 thermally decomposed from the carbonates (decarbonization), in addition to deeply-derived CO_2 already shown to be a major contributing factor in Apenninian earthquake sequences. Model results also suggest that aftershock sequences that differ from the standard Omori-type decay rate (e.g. The 2016 AVN-sequence, the 2011 Tohoku earthquake, Japan and the 2014 Iquique earthquake, Chile) indicate the internal generation of fluids from either dehydration or de-carbonization.

3.3 Introduction

Significant earthquakes in the central Apennines include the 1997 Colfiorito (M_w 6.0), the 2009 L'Aquila (M_w 6.3) [Boncio and Lavecchia, 2000, Chiaraluce et al., 2003, Chiarabba et al., 2009, Antonioli et al., 2005, Carro et al., 2005], and more recently the 2016 Amatrice-Visso-Norcia (AVN) sequence [Spallarossa et al., 2021, Mancini et al., 2019, Michele et al., 2020]. These normal faulting earthquakes share many common features, including rich aftershock sequences in the months following the mainshock. The AVN sequence started with a M_w 6.0 earthquake on August 24, 2016 at a hypocentral depth of 8 km near the city of Amatrice. A robust aftershock sequence ensued, including a M_w 5.9 event on October 26, 2016 at the northernmost extent of the sequence near the town of Visso, and finally a M_w 6.5 earthquake on October 30, 2016 near the town of Norcia [Chiaraluce et al., 2017].

This extensional regime stores large volumes of mantle-derived CO_2 shown to play a significant role in Apennines seismogenesis [Miller et al., 2004, Di Luccio et al., 2010, Chiodini et al., 1995, Chiodini et al., 2004, Chiodini et al., 2020, Tung and Masterlark, 2018].

High pressure fluids have long been implicated as an important contributor to seismogenesis [Sibson, 1992, Sibson, 2007, Micklethwaite and Cox, 2004, Nur and Booker, 1972], and previous studies indicated a direct coupling between seismicity in the Apennines and CO_2 degassing [Chiodini et al., 1999, Miller et al., 2004, Chiarabba et al., 2009, Chiodini et al., 2013, Terakawa et al., 2010]. Geochemical evidence of mantle-derived CO_2 post-seismically infiltrating aquifers in the seismogenic region support this interpretation [Chiodini et al., 2020, Frondini et al., 2019].

The Colfiorito and L'Aquilla earthquakes share features of the geological setting of the AVN sequence. The Colfiorito earthquake sequence occurred within the Umbria–Marche domain (Mesozoic–Cenozoic) consisting of Upper Triassic-Miocene carbonates, while the L'Aquila earthquake sequence occurred in the carbonate (e.g. dolostone) sedimentary sequence of the Latium–Abruzzo domain (Mesozoic–Cenozoic), and Laga Formation. The AVN sequence occurred in the Umbria-Marche domain and the Laga Formation (Miocene – Pliocene) consisting of Upper Miocene flysch deposits [Montone and Mariucci, 2020].

The Visso-Norcia earthquakes share the geological succession of Colfiorito, and although the Amatrice earthquake initiated in the geological unit of L'Aquilla, it propagated northward into the Colfiorito section [Montone and Mariucci, 2020]. For simplicity, we do not identify specific geological units, but since both regions are predominantly carbonates, we assume a general geological cross section that approximates both regimes (Figure 3.1).

We build on an existing model [Miller, 2020] by including a source term to consider the growing body of evidence that significant fluid sources are generated through thermal decomposition of carbonates and the invasion of deeply derived fluids into the system [Girault et al., 2018, Kim et al., 2021, Collettini et al., 2013, De Paola et al., 2011, Han et al., 2007].

The mathematical model is formulated as non-linear diffusion in a porous media with a source term, and written:

$$\frac{dP}{dt} = \frac{1}{\phi\beta} \bigtriangledown \cdot \left[\frac{k}{\eta} \bigtriangledown P \right] + \frac{S}{\phi\beta} \tag{3.1}$$

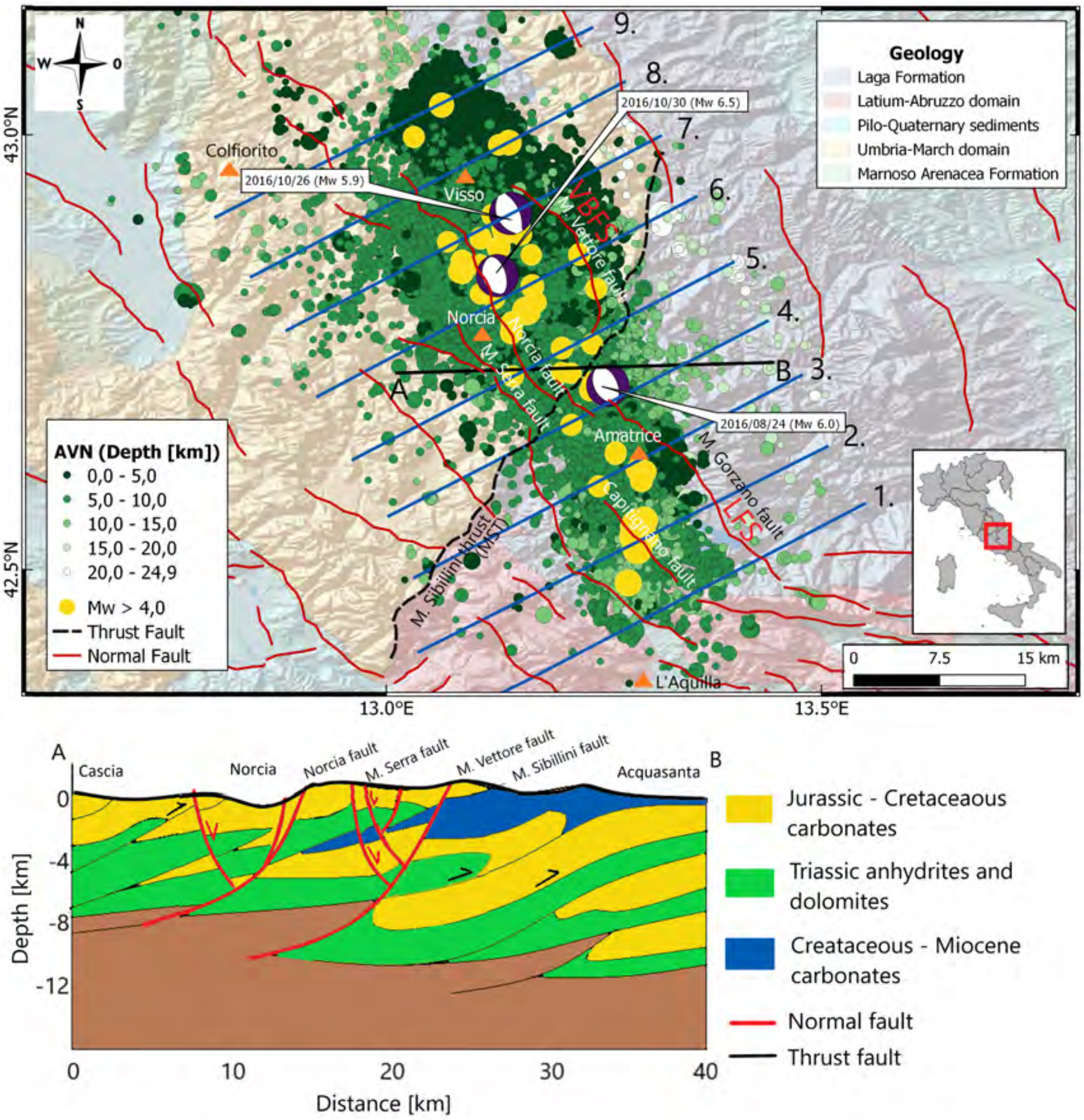

Figure 3.1: Study Area. a) Map showing hypocenters (green) of 34,108 well located aftershocks from the 2016 AVN Apennines sequence. All aftershocks equidistant from the labelled profiles (1-9) are used for temporal and spatial comparisons. Red lines indicate normal faults including the Vettore-Bove fault system (VBFS) and the Laga fault system (LFS), and the dashed black line indicate the Mt. Sibillini thrust fault (MST). Note that the MST is shallow-dipping towards the NNW, so the aftershocks in profiles 4 and 5 are primarily located within the footwall of the MST. Focal mechanisms from the three largest events show a normal faulting sequence. Yellow circles are all $M_w \geq 4.0$. b) Simplified geological cross-section of the region (modified from [Porreca et al., 2018]), showing alternating Jurassic and Cretaceous carbonates, and also Triassic dolomites and anhydrites, cut by normal and thrust faults.

where P is fluid pressure [Pa] above hydrostatic, t is time [s], ϕ is porosity [-], β

is the lumped compressibility of the pore space and fluid $[Pa^{-1}]$ [Segall and Rice, 1995], k is permeability $[m^2]$, η is fluid viscosity [Pa s], and S is a source term $[s^{-1}]$. Note that the units of S $[s^{-1}]$, when divided by $\phi\beta$ $[Pa^{-1}]$ results in a pore pressure increase rate $[Pa/s]$.
Permeability is further defined as:

$$k = (kc_0 + d \cdot exp(-\alpha_j t_j)) \cdot exp(-\sigma_e/\sigma^*); \tau > \mu\sigma_n \tag{3.2}$$

where kc_o is a baseline permeability, d is a co-seismic step-increase in permeability at slip [m2] [Miller, 2015, Miller, 2020], $\alpha_j[s^-1]$ is the parameter controlling the permeability recovery for the duration t_j [s], σ^* [Pa] constrains the permeability response to the effective normal stress σ_e [Rice, 1992, Miller et al., 2004], τ is the shear stress [Pa], μ is the friction coefficient and σ_n is the normal Stress [Pa]. The subscript j=1:3 in this work reflects the different phases in the observed aftershock rates (Methods).
The source term is written:

$$S = Q_0 e^{\pm\zeta_j t_j} \tag{3.3}$$

where Q_0 $[s^{-1}]$ is introduced along activated numerical faults to mimic decarbonization, and ζ_j determines the timescale of source generation and also the possibility of source consumption back into carbonates over a timescale t_j. The source term is not well-constrained without laboratory experiments, so we choose $Q_o = 1e^{-8}$ $[s^{-1}]$ because this value was suitable for all profiles.

In this work, we assume $\alpha_j = \zeta_j$ in both the permeability and source terms to minimize the number of free parameters, but these can be independently investigated in future studies. Conceptually, α and ζ are likely related because the fluid pressure from the source increases permeability in Equation (3.2), while permeability recovers as the source pressure diffuses. Laboratory experiments are required to constrain α and ζ. The dominant parameter α_j is the only parameter varied between simulations, with the sign and value of α_j constrained by the data.

3.4 Study area

The dataset [Spallarossa et al., 2021] was compiled using the non-linear location (NLL) algorithm with the Complete Automatic Seismic Processor (CASP) and located about 450,000 events in the year following the first AVN earthquake (August 24th, 2016). The relocated earthquakes cover nearly 60 km along strike of the

Apennines NW-SE trending normal fault system [Chiarabba et al., 2020]. From this dataset, we excluded earthquakes without a listed magnitude, depths marked as uncertain, and events with magnitudes below the magnitude of completeness $M_c = 1.2$. This resulted in our dataset of close to 35,000 events.

Figure 3.1a shows the epicenters for all well-located events $M_w \geq 1.2$ for one year following the onset of the M_w 6.0 earthquake (Aug. 24, 2016). Significant faults in the study area are also shown, and include the Mt. Vettore fault, Norcia fault and importantly the Monti Sibillini Thrust fault (MST). Focal mechanisms for the three largest events (U.S.Geological Survey) indicate predominantly normal faulting.

We investigate the catalog by dividing the dataset into 9 cross-sectional profiles (labeled 1-9 in Figure 3.1a) perpendicular to the general trend of the seismicity, and roughly corresponding to the strike (N130°) of the Vettore-Bove-Fault-System (VBFS) and Laga-Fault-System (LFS). Figure 3.1b shows the major geologic features of a succession of the alternating Jurassic and Cretaceous carbonates, and also Triassic dolomites and anhydrites [Collettini and Barchi, 2002, Di Domenica et al., 2012]. These lithological units are intersected by many normal faults, including the Mt. Vettore, Mt. Serra, and Norcia faults.

The Amatrice-Visso-Norcia earthquake primarily activated the Vettore-Bove fault system in the north and the Laga fault systems in the south. These fault systems include the NW-SE trending Mt. Gorzano fault on the western slope of the Laga Mountains, the NE dipping Mt. Bove and Mt. Vettore faults in the north, and the SW dipping Mt. Serra and S. Lorenzo faults in the central and northern Apennines [Stemberk et al., 2019, Galadini and Galli, 2003]. Figure 3.1b shows the first 8 km of SW-dipping normal faults bounded by NE dipping normal faults. For this study, we inferred the activated fault planes from this geologic cross section.

The NNW-dipping M. Sibillini Thrust fault (MST) located between Amatrice and Norcia plays a significant role in the spatio-temporal evolution of the AVN earthquake sequence. The MST acts as a barrier between Amatrice and Visso mainshocks, giving further evidence for reactivation of different normal faults in the north and south and later as an asperity for the Norcia mainshock [Improta et al., 2019].

Figure 3.2a shows the cumulative number of aftershocks recorded for each profile (from south to north), and shows a systematic transition from non-Omori like behavior (profiles 1-3), to an intermediate behavior (profiles 4-6), finally transitioning to Omori-like behavior in the north (profiles 7-9). For comparison, the dashed lines in Figure 3.2a shows typical Omori behavior. Figure 3.2b shows all measured hypocenters for each profile, with our simple 3-fault system used in the model simulations. Note that the hypocentral distribution of aftershocks for each profile shows much complexity and little consistency between each of the profiles.

The AVN sequence included three significant earthquakes, each of which generated their own aftershock sequence. This indicates behavior similar to that observed in Colforito [Miller et al., 2004] where the earthquakes breached a seal separating deeply trapped CO_2 and the hydrostatically pressurized carbonate system.

3.5 Methods

The numerical algorithm is described in detail elsewhere [Miller et al., 2004, Miller, 2015, Miller, 2020] but a short summary is useful here for completeness.

We numerically solve, using implicit finite differences, the non-linear diffusion Equation 3.1 on a regular grid of 300x300 nodal points to calculate fluid pressure diffusion through a permeable numerical domain. We impose no-flow boundary conditions on the side and bottom boundaries, and a constant hydrostatic pressure at the surface. The model includes a temperature-dependent viscosity for supercritical CO_2 with a value of $\eta = 1e^{-4}\, Pa\ s$ at the surface, resulting in $\eta = 1e^{-5}\, Pa\ s$ at the depth of the fault system, and choose compressibility $\beta = 4e^{-9}\, Pa^{-1}$. Both of these parameters are in the range of supercritical CO_2 at relevant temperature and pressure shown elsewhere [Sulem and Famin, 2009].

We assume porosity of 0.03, a friction coefficient of 0.48, maximum principal stress (σ_1) is vertical with rock density of $2700\, kg/m^3$, and the minimum principal stress σ_3 is horizontal and assumed 0.62 σ_1. We also assume $\sigma^* = 35\, MPa$ and $kc_0 = 1e^{-12}\, m^2$, as used elsewhere [Miller, 2020, Zhu et al., 2020]. This formulation results in an initial background permeability field roughly approximating crustal permeability [Manning and Ingebritsen, 1999].

At the start of each simulation, we impose a source term $Q_0 = 1e^{-8}\, s^{-1}$ on the activated fault to simulate the generation of fluids (e.g. CO_2) through thermal decomposition of carbonates associated with a large earthquake event. We solve Equation 3.1 to calculate fluid pressure (above hydrostatic) as it diffuses from the source through the dynamic permeability of the numerical domain, and record the time and location of a triggered numerical aftershock. See Supplemental Information for visualizations of the dynamic permeability for each simulation. A numerical aftershock is defined as a nodal grid point reaching the Mohr-Coulomb failure condition. When a numerical grid point fails, the local permeability increases by a factor d (assumed 1000), initiating t_j that controls permeability recovery and the source

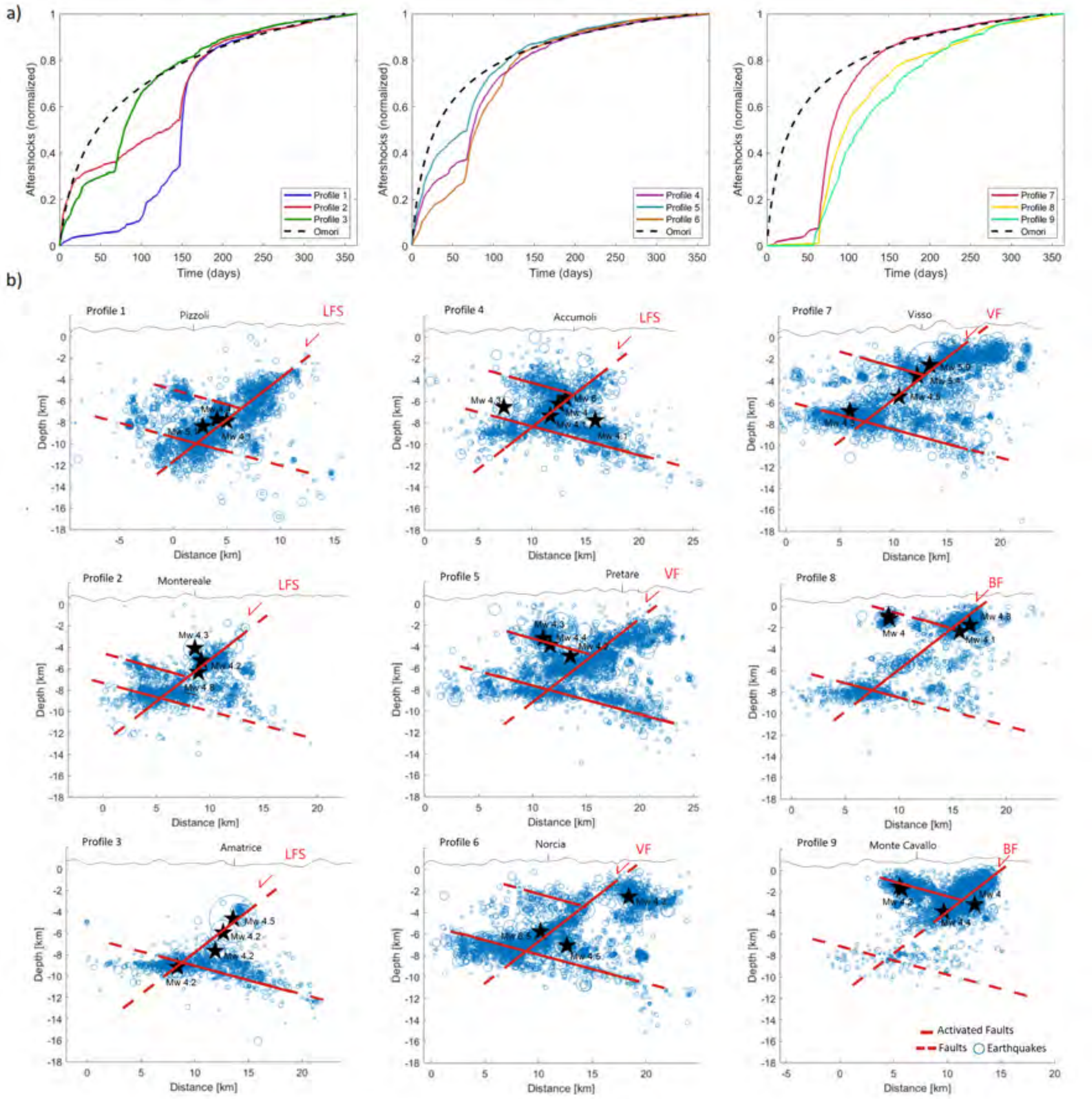

Figure 3.2: Data and Model Setup. a) The cumulative number of aftershocks associated with each profile (Figure 3.1) (normalized by the maximum number of events in each catalog). The dashed line indicates typical Omori Law behavior. b) Spatial distribution of hypocenters (blue) with the numerical faults shown superposed. Fault locations were chosen to respect the geological model (e.g. LFS and VF faults) and also constrained by hypocenter locations. Activated faults (e.g. $Q_0 = 1e^{-8}\, s^{-1}$) are shown as dashed red lines, and the solid red line denotes permeable faults ($k_0 = 1e^{-12}\, m^2$) without an active source term. Black stars indicate $M_w \geq 4$ events and the relevant earthquake defining temporal phases.

term governed by $\alpha_j = \zeta_j$.

The first phase (Figure 3.3a) begins with the M_w 6.0 earthquake on August 24, 2016, where the source term is activated on faults designated yellow in Figure 3.2b and decays at a timescale defined by $\zeta_1 = \alpha_1$. The source term (Q_0) is then reactivated at time t_2 to start the second phase, decaying at a timescale defined by $\zeta_2 = \alpha_2$, and the third phase at a time t_3 defined by $\zeta_3 = \alpha_3$. The start of each phase is constrained by the data, but it's worth noting that each phase initiates with $M_w \geq 4$ earthquakes (Figure 3.3).

Mechanics are only virtually simulated by imposing a normal distribution of slip planes relative to the maximum (σ_1) and minimum (σ_3) principal stresses and passing through a numerical grid point. The normal and shear stresses on the virtual plane are:

$$\tau = \frac{\sigma_1 - \sigma_3}{2} sin(2\theta) \tag{3.4}$$

$$\sigma_n = \frac{\sigma_1 + \sigma_3 - 2P_f}{2} - \frac{\sigma_1 - \sigma_3}{2} cos(2\theta) \tag{3.5}$$

where θ is the angle measured from the normal to σ_1.

3.6 Results

Our goal is to match both the rate of aftershocks (Figure 3.2a), and the spatial distribution of hypocenters (Figure 3.2b), using a simple 3-fault system for all simulations. We purposely limit input parameter variations, constraining ourselves to variations in only one parameter, α.

The aftershock rates for profiles 1-9 (Figure 3.2a) show behavior dissimilar to typical Omori-type decay rates (dashed lines Figure 3.2a). To capture this behavior, we choose a different α_j for each distinct phase of the aftershock record. We identify the time of the observed rate change, and adjust α_j until at a suitable fit is achieved for the entire record. The sign of α_j is always negative because permeability persistently recovers back to its natural pre-seismic state. The sign of the source term ζ_j, on the other hand, is generally negative because the source generation rate reduces, but takes on a positive sign (2nd phase) upon initiation of a new large earthquake, which we propose corresponds to thermal decomposition and a direct fluid source.

We simulate for 365 days and compare model results to the data. We discuss, in turn, model results (Figure 3.3) compared to the temporal evolution of aftershocks (Figure 3.2a), and model results (Figure 3.4) compared to the spatial distribution of hypocenters (Figure 3.2b).

Figure 3.3a shows observed cumulative aftershocks (black) superposed with modelled cumulative aftershocks (red) for the nine profiles across the study area. We find very good agreement between model results and observations for all phases and all profiles of the AVN sequence. Insight into these results can be gained by discussing values for α and ζ for each of the observed phases of aftershock rates. Recall that in our simulations we assume $\alpha_j = \zeta_j$, so will we discuss only in terms of α. Figure 3.3b summarizes the α_j values used in the simulations for each phase, and plotted for intuitive convenience as $1/\alpha$ [days].

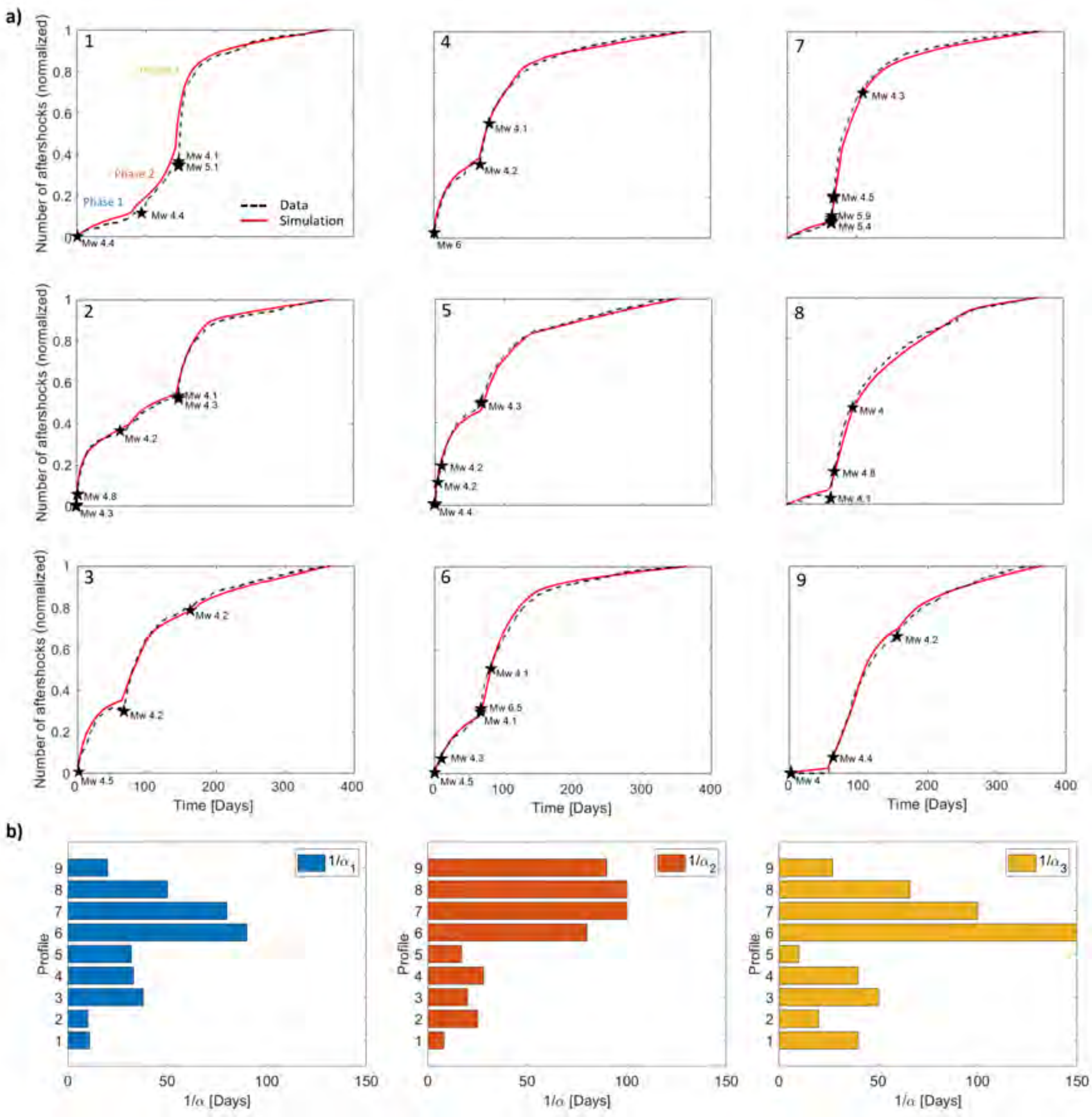

Figure 3.3: Temporal comparison of data and model. a) Comparison of observed cumulative aftershocks for each profile with model results shown superposed. The different phases discussed in the text are indicated in profile 1 and applied to all profiles. Stars indicate events with $M_w \geq 4$ and the onset of different phases. b) Compendium of $\alpha = \zeta$ for each profile used to match the data in a). See text for details.

Phase 1 (blue) : Profile 1 and 2 show $1/\alpha$ values from 10-12 days that indicate, according to our model, limited direct fluid sources and rapid permeability recovery. In contrast, profiles 3, 4 and 5 (located in the vicinity of August 24, 2016 earthquake) shows $1/\alpha$ values from 35-38 days, indicating a direct fluid source of CO_2 and sluggish permeability recovery compared to profiles 1 and 2. This result provides evidence for CO_2 generation from decarbonization, and/or invasion of a deep fluid source and concomitant with longer permeability recovery times.

The MST barrier roughly coincides with the boundary between profiles 5 and 6, and even though our model does not know of this boundary, the simulation results capture this barrier with ($1/\alpha$). Specifically, profiles 6 and 7 ($1/\alpha$ = 75-85 days) suggests tapping into a substantial high pressure CO_2 reservoir at depth, resulting in long model permeability recovery times. We expect no internal generation of fluids in this region in Phase 1 because no significant earthquake had yet occurred. In regions further north of the MST barrier (profiles 8 and 9), $1/\alpha$ progressively decreases ($1/\alpha$ = 20-50 days) indicating a less vigorous reservoir at depth. We speculate that the reservoir at depth decreases in intensity further to the north because section 9 corresponds to the southern extent of the Colfiorito sequence, which likely degassed during the 1997 seismic sequence [Miller et al., 2004].

Phase 2 (orange) initiated with a $M_w\,5.9$ earthquake, followed 4 days later by a $M_w\,6.5$ earthquake, the largest earthquake in the AVN sequence. The epicenters for both these events initiated in profiles 6 and 7, and continued rupturing through profiles 8 and 9. Model results show $1/\zeta = 1/\alpha = 80 - 100$ days for profiles 6-9, indicating a substantial source of co-seismically generated CO_2 via thermal decomposition. Meanwhile, to the south, and to the south of the MST barrier, recovery times are relatively swift for profiles 1-5, ($1/\alpha$ = 10-30 days), indicating a minor influence from the large earthquakes north of the MST, and thus limited source generation and rapid permeability recovery.

Phase 3 (yellow) : In the south, several $M_w \geq 4.5$ earthquakes occurred in profiles 1-3. This is reflected in slightly higher values for $1/\alpha = 1/\zeta$ = 25-50 days, indicating internal fluid generation and/or additional input of high-pressure sources at depth. In contrast, profile 5 is relatively distant from these earthquakes and therefore not influenced (i.e. $1/\alpha$ = 10 days).

Finally, profile 6 hosting the $M_w\,6.5$ earthquake suggests continuous source generation and/or deep source input, and long duration permeability recovery ($1/\alpha$ = 150 days). Meanwhile, profiles 7,8 and 9 tend towards Omori-type behaviour and display a smooth decay in source and permeability recovery times northwards ($1/\alpha$ = 35-100 days).

Figure 3.4 compares the calculated fluid pressure field (at 365 days) with 35,000 well-located hypocenters shown superposed for each profile. Simulation results show that the calculated fluid pressure encases an overwhelming majority of measured hypocenters for all profiles. These results, using a simple and intuitive model for permeability dynamics and a simple fault system, indicates that this model captures the dominant physics driving this sequence.

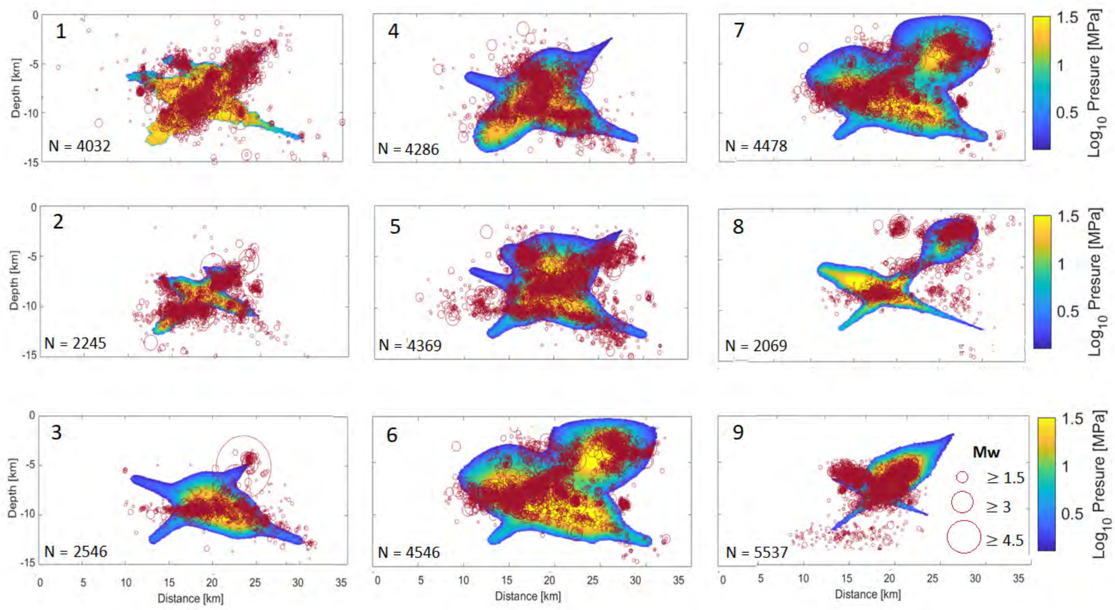

Figure 3.4: Comparison of calculated fluid pressure field at 365 days and measured hypocenters for profiles 1-9 (Figure 3.1) shown superposed. The number of hypocenters used in the comparison for each panel is indicated by N.

Figure 3.5 summarizes our findings, and shows that the MST, not implemented in our model, emerges from our modelling results. Specifically, results show that the MST acts as a hydraulic barrier separating two isolated over-pressured systems at depth, and this is reflected in both the source generation and permeability recover times. The observed hypocentral distribution supports our interpretation because the productivity of aftershocks is significantly higher north of the MST compared to the south.

3.7 Discussion and Conclusion

We showed that a model of non-linear diffusion with a source term successfully reproduces the observed temporal aftershock rates and shows strong spatial correlations between calculated fluid over-pressure and the hypo-central locations of tens

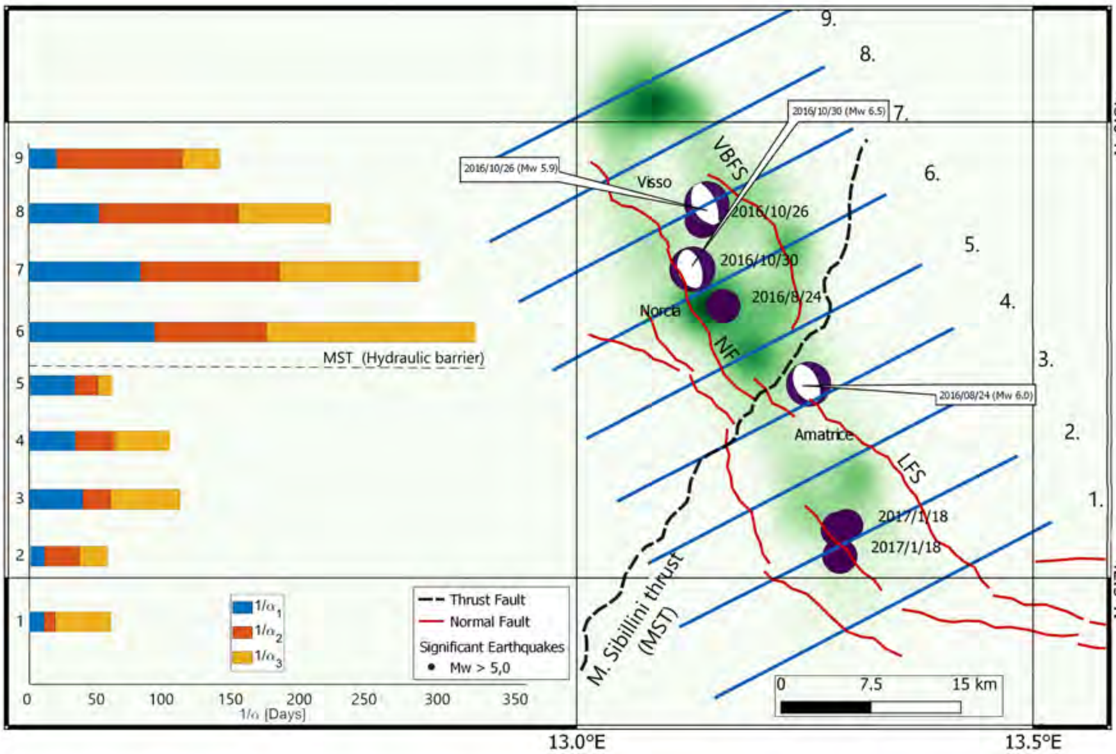

Figure 3.5: Summary of results. The earthquake density (green) shows significantly more activity north of the MST compared to south of the MST. Profiles 4 and 5 are connected to the southern hydraulic system because the shallow dip of the MST towards the NNW means that these aftershocks were located in the footwall. The bar chart summarizes $1/\alpha$ used in the simulations, and clearly indicates substantially more high pressure CO2 input from a deep reservoir and/or direct fluid source from thermal decomposition.

of thousand of well-located aftershocks. We intentionally kept the model simple by imposing a 3-fault system using the same material properties for simulating 9 profiles along the 60 km strike of the 2016 AVN aftershock sequence. Despite the vast differences in observed cumulative aftershock rates for each profile, the model accurately reproduced the observations by varying only one parameter. This parameter ($\alpha = \zeta$) controls the timescale for permeability recovery and the timescale for fluid input from either a deep source of CO_2 and/or direct fluid source from thermal decomposition of the ubiquitous carbonates of the Apennines.

The AVN sequence initiated with a magnitude $M_w 6.0$ earthquake with the epicenter just south of the MST north-dipping thrust fault. The largest aftershock of this earthquake occurred north of the MST with $M_w 5.3$, and the total along strike length of these events measured about 25 km. Therefore, these earthquakes affected two different hydraulic systems, separated by the MST, one hydraulic system to the north, and one to the south. Modeling indicates a more vigorous and energetic high pressure reservoir north of the MST because of the long-duration source and permeability recovery times (e.g. high $1/\alpha$) as compared to south of the MST (Figure 3.5).

Continuing with this reasoning, the subsequent $M_w5.9$ and $M_w6.5$ earthquakes occurring north of the MST also indicated long-duration source and permeability recovery times (e.g. high $1/\alpha$), while having little influence south of the MST. The three $M_w5.5$, $M_w5.4$ and $M_w5.1$ earthquakes on 18th January 2017 in the south (reflected in profile 1-Phase 3) shows an increase of $1/\alpha$ from 8 to 45 days, indicating additional influence of high pressure CO2. Overall, profiles 2-5 in phase 3 also shows a slight increase in permeability recovery and source generation compared to phase 2. In contrast, the northern extent of the AVN sequence (profiles 6-9), which experienced no further large aftershocks, continues to recover from the initial fluid source generation when compared to phases 2 and 3. The physical foundation of our model is that both earthquakes, and their aftershocks, can generate additional aftershocks because co-seismic decarbonization provides a direct high-pressure fluid source. These aftershocks create new pathways to propagate high-pressure pulses from the deeply generated and trapped fluid sources. This is consistent with the fundamental assumption of the Epidemic Type Aftershock Sequence (ETAS) model that aftershocks can generate their own (daughter) aftershock sequences. Studies of some aftershock sequences, including the AVN sequence, show that ETAS, by itself, is insufficient to reproduce aftershock time histories, but satisfactory comparisons are found when ETAS is combined with physical models such as Coulomb stress transfer and rate-and state friction [Cattania et al., 2018, Mancini et al., 2019]. These studies demonstrated the importance of crustal heterogeneity and stress field, which are well described by the Coulomb rate-state (CRS) model and the ETAS model.

Importantly, we do not assume the basis of ETAS in our model, but instead ETAS emerges from the underlying physics. We show that a simple physical model can match recorded observations from a complex faulting system in the Apennines, and model results suggest that high pressure CO_2, either deeply derived or co-seismically generated through thermal decomposition, is the primary driver of seismicity in the Apennines.

This study focused on the Apennines, but our approach is applicable to any tectonic environment where co-seismic devolatilization is likely to occur. We propose that aftershock rates that do not follow typical Omori-type behavior, such as the linear relationship observed for the 2011 Tohoku, Japan ($M_w = 9.1$), and the 2014 Iquique, Chile ($M_W = 8.2$) subduction zone earthquakes, are indicative of continuous sources of high pressure fluids from devolitization that both drive the sequences and restrict permeability recovery argued to control aftershock decay rates [Miller, 2020].

These results provide a new conceptual framework for interpreting seismological, geochemical, geophysical, and geological observations, and open up new experimental directions for quantifying volatile production at earthquake-relevant slip rates.

Chapter 4

3D modeling of internal generation of CO_2 in the Apennines: the relationship between the L'Aquila 2009 and Amatrice-Visso-Norcia 2016 earthquake sequences

4.1 Abstract

The extensional carbonate regime in the Apennines stores large quantities of mantle-derived CO_2. Groundwater and satellite observations provide evidence of CO_2 degassing, while other studies implicate CO_2 as an important contributor to seismogenesis in the Apennines. However, those studies usually focus on existing reservoirs at depth; we propose that co-seismic thermal decomposition of CO_2 also contributes significantly to seismogenesis. Thermal decomposition provides substantial quantities of internally derived high-pressure fluids that diffuse to the surroundings, triggering seismicity along the flow paths. In this work, we develop a 3-dimensional model of non-linear diffusion with a source term and compare model results with the spatial and temporal observations from the 2009 L'Aquila (M_w6.3) and the 2016 Amatrice-Visso-Norcia (M_w6.5) earthquake sequences. The model mimics the generation of additional fluid by thermal decomposition and shows good correlations in space by comparing the calculated fluid pressure field and of over 50,000 well-constrained hypocenters. We also show good correlations in time between the observed cumulative number of aftershocks and numerically triggered events. The results strongly suggest that thermal decomposition is a significant driver of Apennine seismicity. We also identify that the AVN sequence filled a seismic gap between the 2009 L'Aquila sequence and the 2016 AVN sequence and show that different fluid production rates activated different fault systems during both sequences.

4.2 Introduction

The tectonic environment in the central Apennines originated from the convergence and collision of the African and European plates [Di Domenica et al., 2014] and by the simultaneous opening of the Tyrrhenian Sea. The compressional orogeny resulted, among others, in the E-NE trending Mt. Sibillini thrust fault [Di Domenica et al., 2012]. The subsequent regional extensional regime, on the other hand, initiated numerous normal faults, including Mt. Vettore, Mt. Bove, Colfiorito, Mt. Laga, Mt. Marine, Mt. Pettino faults, among others, within the past 2-3 million years. A series of normal fault earthquakes from moderate to large magnitudes characterize the Central Apennines in the past millennia. For example, the 1703 (M_w 6.9), the 1762 (M_w 5.7), the 1859 (M_s 5.9), and the 1979 (M_s 5.9) earthquakes occurred all around the Norica, the Amatrice and L'Aquila basin [Galli et al., 2021, Tertulliani et al., 2009, Guidoboni et al., 2015].More recent earthquakes, including the 1997 Colfiorito (M_w 5.6), 2009 L'Aquila (M_w 6.3), and 2016 Amatrice-Visso Norcia (AVN) (M_w 6.5) show that the central Apennines are the very seismically active [Mancini et al., 2019], causing severe damage to the towns and surrounding villages and claiming more than 650 lives.

Recent groundwater monitoring studies and satellite observation showed changes in Piezometric levels, spring discharges, groundwater chemistry, and ground thermal emissions in central Italy [Martinelli et al., 2020]. More precisely, the central Apennines experience fluctuations of groundwater pressure and changes in the chemical composition of local groundwater [Barberio et al., 2017, Boschetti et al., 2019]. In addition, satellite-based techniques captured large-scale CO_2 degassing phenomena during seismic events [Genzano et al., 2009, Bonfanti et al., 2012]. These observations correlated to the spatio-temporal evolution of the earthquake sequences.

Between 2004 and 2017, the atmosphere experienced a high discharge rate of CO_2 (about 20 million tons/year) from cold gas venting and the dissolution of CO_2 under high pressure from thermal sources. This is one third of the total geological CO_2 degassing in Italy [Minissale, 2004, Frezzotti et al., 2009, Chiodini et al., 2011]. Evidence continuously mounts that the intensity of earthquake and aftershocks in the central Apennines are not only generated by the regional extensional tectonics but also by a significant fluid source (High-pressure CO_2) associated with carbonates in the Apennines [Barnes et al., 1978, Tamburello et al., 2018, Irwin and Barnes, 1980]. Notably, during the 2009 L'Aquila sequence, a gas vent located 80 km from the epicenter recorded significant variations in CO_2 degassing rates as well as in local groundwater [Heinicke et al., 2012]. In addition, during the 2016 AVN sequence, the carbonate-hosted aquifer showed a mantle-derived CO_2 flux [Barberio et al., 2017].

Our working hypothesis suggests that this extensional regime stores a large amount of CO_2, derived from the Earth's mantle and generated internally by thermal decomposition, and creates highly permeable fractures during seismic events from which the CO_2 can then escape to the Earth's surface. Consequently, seismic activity enables the uprising fluid and release of overpressurized CO_2.

In this paper, we numerically investigate this hypothesis by comparing a 3-dimensional numerical model with observed aftershock rates and the spatial distribution of more than 50,000 aftershocks from the L'Aquila and AVN earthquake sequences.

4.3 The Study Area and Conceptual Model

Figure 4.1a shows the hypocenters of all well-located events during the 2009 L'Aquila sequence for approximately 200 days after the onset of the largest earthquake, and color-coded by depth. Focal mechanisms for events M_w >4.7 indicate predominantly normal faulting. These earthquakes generated more than 20.000 aftershocks in the following year.

Figure 4.1b shows the hypocenters of all well-located events during the 2016 AVN sequence for approximately 200 days after the onset of the mainshock, and color-coded by depth [Spallarossa et al., 2021]. Focal mechanisms for events M_w >5 all indicate normal faulting, consistent the overall tectonics of the Apennines. The sequence initiated on August 24th, 2016, with a magnitude of M_w 6.0 in the town of Amatrice at a hypocentral depth of 8km. Two months later (October 26th), the next major earthquake with a magnitude of 5.9 occurred at a hypocentral depth of 7 km, near the town of Visso. The strongest earthquake with a magnitude of 6.5 on October 30th occurred in the town of Norcia, located between the previous prominent earthquakes [Chiaraluce et al., 2017]. Finally, in January 2017, a few significant earthquakes of $M_w > 5$ occurred near the town of Campotosto in the south [Michele et al., 2020]. The Istituto Nazionale di Geofisica e Vulcanologia (INGV) located more than 100,000 seismic events in 3 months [Bignami et al., 2019] with an affected area of $> 1000km^2$. Within a year, each of these earthquakes generated more than 450,000 aftershocks of which we consider approximately 35,000 very well-located events.

Figure 4.1c shows the geological units and significant fault systems for both

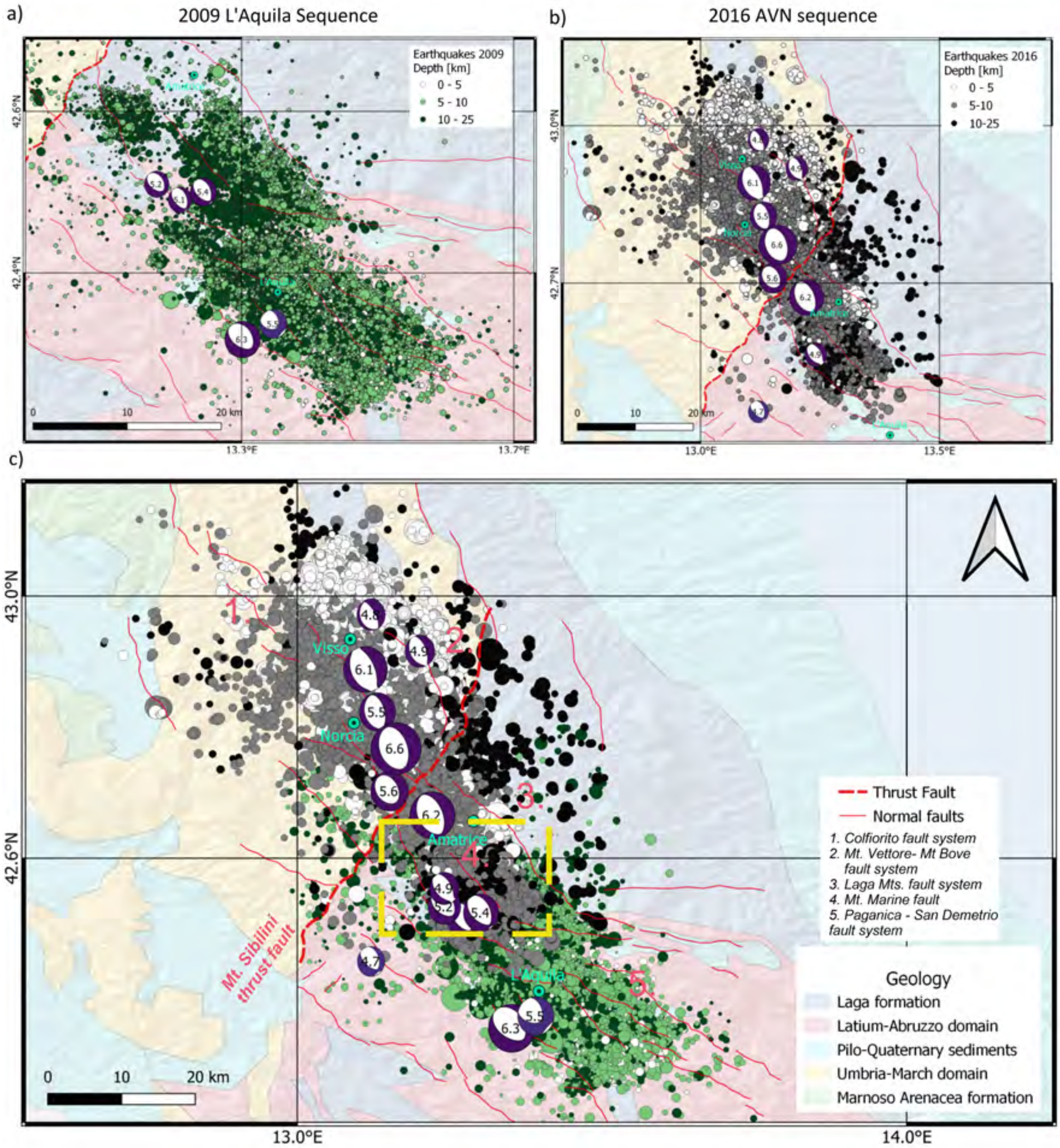

Figure 4.1: a/b) Hypocentral distribution of the 2009 L'Aquila sequence and the 2016 AVN sequence. color-coded by depth in gray and green, respectively. (b) Both earthquake sequences that seem to overlap in northern L'Aquila and southern Amatrice are associated with three dominant geologic units: (i) the Lazio-Abruzzo domain (pink), (ii) the Umbria-Marche domain (yellow), and the (iii) Laga Formation (purple). Numerous fault systems were activated during the earthquake sequences, including: the Colfiorito fault system (CI), Norcia fault system (NF), Mt. Vettore, Mt. Bove fault system (VBFS), Laga Mts. fault system (LFS), the Montereale fault system (MFS), and the Paganica-S. Demetrio fault system (PSDFS).

earthquake sequences. Two major lithological units developed during the Tethyan rifting stage and included the Latium-Abruzzi carbonate platform domain, and the

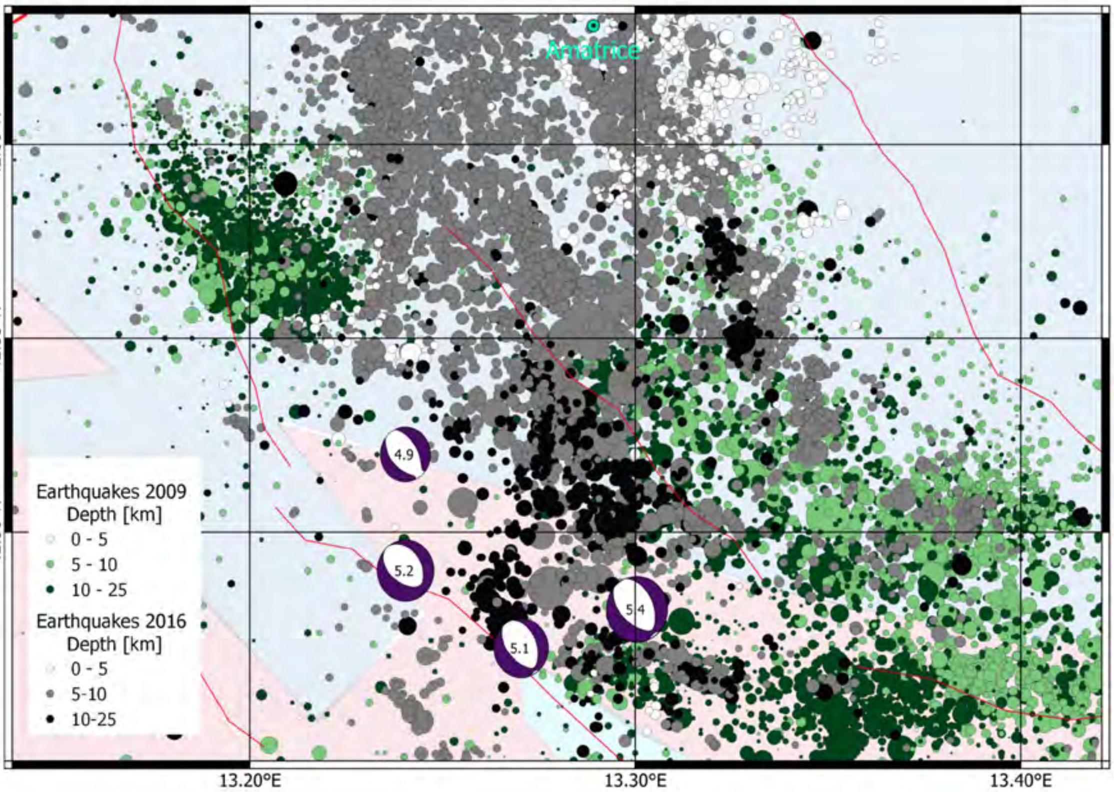

Figure 4.2: Close-up view (Yellow box in Fig. 4.1) of the hypocentral distribution of the northern 2009 L'Aquila and the southern 2016 AVN sequence showing a seismic gap during 2009 L'Aquila, but was filled during the 2016 sequence.

pelagic Umbria-Marche domain. The Umbria-Marche domain (yellow) consists of calcareous-cherty and marly rocks and the Latium-Abruzzi domain (pink) consists of limestone, dolomitic limestone, and dolostone [Tavani et al., 2021, Galluzzo and Santantonio, 2002]. Meanwhile, African/European collision resulted in the deposition of deep marine siliciclastic turbidites. These lithological deposits dominate the Laga Basin and are known as the Laga Formation (purple). Finally, the NW-SE striking normal faults produced numerous intermediate mountains filled with lacustrine, alluvial, and slope debris deposits (blue) [Koopman, 1983, Ettinger et al., 2021].

The 2009 L'Aquila earthquake sequence and the 2016 AVN sequence activated a considerable fault systems (Figure 1c). These include, from north to south, Colfiorito (CI), Norcia (NF), Mt. Vettore- Mt Bove (VBF) fault systems, the Laga Mountain fault system (LF), the Montereale (MF), and the Paganica-S. Demetrio fault system (PSDF). Note that we interchange both the names and their acronyms throughout the manuscript, as needed for clarity. The mainshock of the L'Aquila sequence (M_w

6.3 on April 6th, 2009) ruptured of the PSDF [Civico et al., 2015, Galli et al., 2010] system, which accumulates slip deficits between 0.5 and 0.9mm/yr. The events of M_w 5.4 and 5.2 on April 9th relate to the NW-SE striking MF system, with slip deficits of 1-3mm/yr [D'agostino et al., 2008, D'agostino et al., 2012]. This complex fault system is composed of the Capitignano fault (CF) and San Giovanni Fault (SGF) with an average strike of N145$\circ$. The Mount Marine fault bounds these two faults in SW and Configno fault in the north.

The 2016 AVN sequence ruptured the Laga fault system (LF) on August 24th, 2016 (M_w 6.0). The M_w 5.9 earthquake (October 26th, 2016) ruptured the Colfiorito and Norcia fault systems, whereas the M_w 6.5 event (October 30th) ruptured the Mt. Vettore- Mt Bove fault system.

The significant earthquake events at the beginning of January 2017 partially overlap with seismic events from L'Aquila 2009 sequence and are associated with ruptures of the Capitignano fault system. On closer inspection (yellow box expanded in Figure 4.2), the apparent overlap of seismic events mostly disappears in the hypocentral distribution, and shows that the 2016 events filled the seismic gap created during the 2009 earthquake sequence.

We propose a simple two or three fault system to investigate the dataset. Figure 4.3a shows the hypocentral distribution of the more than 50,000 well-located events. We investigate the catalog by dividing the dataset into four cross-sectional profiles to better visualize earthquake locations along the different fault systems. The 2009 L'Aquila sequence, separated by the Montereale fault (MF) system and the Paganica-s. Demetrio fault (PSDF) system defines L'Aquila's north and south profiles. Figure 4.3b shows the northern L'Aquila profile including both the LF and the MF system with two additional shallow east-dipping faults. Note that the entire study area consists of numerous unnamed and shallow east-dipping faults which are shown as green and brown in Figure 4.3. The 2016 AVN sequence is cut by the Mt. Sibillini thrust fault, resulting in a North and South profile (Figure 4.3d-e). The northern profile consists of a 3-normal fault system that includes the NE-SW dipping VBF system bounded by two shallow east-dipping faults within the first 8km of the upper crust. Figure 4.3e shows seismic events of the southern AVN profile and consists of the LF system (similar to the 2009 sequence) and two east-dipping normal faults.

This work aims to mimic the internal generation of high-pressure fluid via thermal decomposition of the carbonates. The recorded earthquakes reveal a propagation of seismicity along the fault systems and their surroundings, which guides our

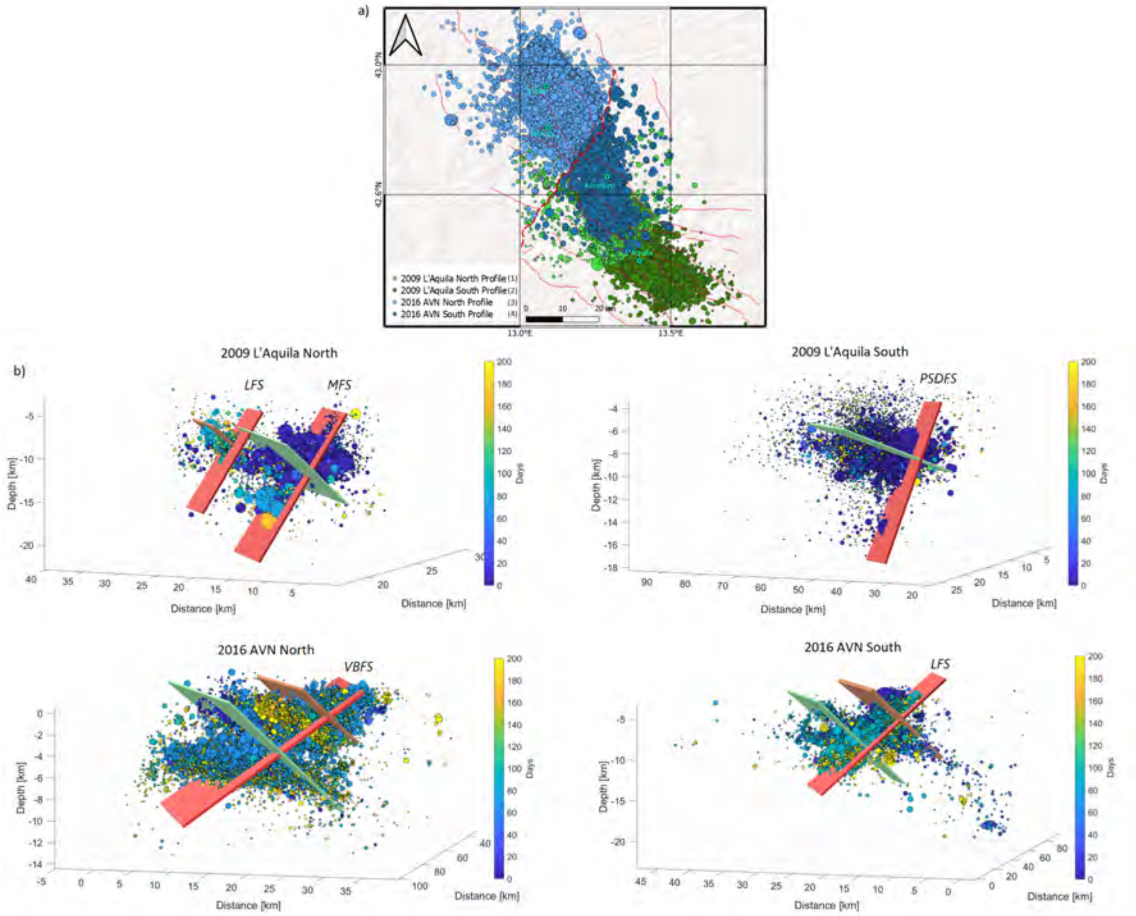

Figure 4.3: Simplified geometry for numerical experiments. a) For better illustration and understanding, we divide the study area into four sections: 1st AVN North profile (dark blue), 2nd AVN South profile (light blue), 3rd L'Aquila North profile (light green), and 4th L'Aquila South profile (dark green). b) A 3-dimensional distribution of the hypocenter of these four profiles allows us to constrain the faults and their direction from the study area. Therefore, a simple model with 2-3 faults is used to calculate the fluid pressure diffusion.

model development to include diffusion processes with a source term.

4.4 Physical Background

We extended the existing 2D model [Gunatilake and Miller, 2022] that includes internal generation of CO_2 to 3-dimensions to investigate the spatial distribuition of hypocenters and the rate of aftershocks.

The propagation of high fluid pressure through a fractured rock is mathematically formulated as a non-linear diffusion equation with a source term:

$$\frac{dP}{dt} = \frac{1}{\phi\beta} \bigtriangledown \cdot \left[\frac{k}{\eta} \bigtriangledown P\right] + \frac{S}{\phi\beta} \tag{4.1}$$

where P is fluid pressure [Pa] above hydrostatic, t is time [s], ϕ is porosity [-], β is the lumped compressibility of the pore space and fluid [Pa^{-1}] [Segall and Rice, 1995], k is permeability [m^2], η is fluid viscosity [Pa s], and S is a source term [s^{-1}].

The internal generation of fluid source S [s^{-1}] is mathematically written:

$$S = Q_0 e^{-\zeta_j t_j} \tag{4.2}$$

where ζ_j determines the timescale of source generation over a timescale t_j.

The distribution of high-pressure fluid depends, among other parameters, on the permeability dynamics within the model [Miller, 2020]. The permeability describes the ability of a fluid to flow through a porous medium and indicates the predominant flow path. Therefore, the heterogeneity of permeability in the subsurface is a crucial parameter that allows us to understand the evolution of seismic events and is defined as:

$$k = (kc_0 + d \cdot exp(-\alpha_j t_j)) \cdot exp(-\sigma_e/\sigma^*); \tau > \mu\sigma_n \tag{4.3}$$

where kc_o is a baseline permeability, d is a co-seismic step-increase in permeability at slip [m2] [Miller, 2015, Miller, 2020], $\alpha_j [s^-1]$ is the parameter controlling the permeability recovery for the duration t_j [s], σ^* [Pa] constrains the permeability response to the effective normal stress σ_e [Rice, 1992, Miller et al., 2004], τ is the shear stress [Pa], μ is the friction coefficient and σ_n is the normal Stress [Pa].

Increasing fluid pressure within the model leads to increased Coulomb stresses and thus regional poroelastic stress development. The Coulomb failure criterion measures static frictional strength. A numerical grid-point fails when $Tau(c) > 0$, resulting in a numerical earthquake. The fluid to redistribute activate or even generate more fractures. Postseismic fluid flow leads to stress re-charging and generates further aftershocks. The clogging of porous media by chemical precipitation and the relaxation of tectonic stresses reduce the permeability over time (controlled by α) and result in fewer and fewer aftershocks. Detailed information about simulating the mechanics is described elsewhere [Gunatilake and Miller, 2022].

4.5 Results

Simulations begin with the onset of the L'Aquila and AVN earthquake sequences and run for 200 days. Figure 4.4 shows the calculated three-dimensional pressure field for each case in figure 4.3 at two different times (left and right column). Figure 4.4a) shows L'Aquila North, figure 4.4b shows L'Aquila South, figure 4.4c shows 2016 AVN North and figure 4.4d shows the AVN South profile. The fault systems used in each simulation are shown embedded in the first column of figures, which shows the calculated fluid pressure (above hydrostatic) between 70-100 days. This period reflects the pressure state before the onset of a healing process, which is controlled by the $1/\alpha$ [days], and discussed in more detail below. In general, all these profiles shows comparably higher pressure in the interior of the fault system, which is then predominantly distributed along the low permeable faults and their surroundings. The high-fluid pressure reach the dominant part of the fault system and several kilometers surrounding the fault within approximately 70-100 days. The second column shows the evolution of the fluid pressure field (above hydrostatic) at the end of the 200 day simulation. All profiles, except AVN North (Profile 3), indicate lower fluid pressure values by the end of the simulation when compared to earlier times. (first column). Results show a pressure drop of approximately 20MPa, which reflects pressure diffusion in a recovering permeability network and cessation of internal fluid source generation. Profile 3, on the other hand, shows comparably higher pressure in the interior of the fault, that continues to diffusion into its surrounding because of sluggish permeability recover and continue internal fluid source generation.

Figure 4.5 shows the spatial distribution of hypocenters superposed on the calculated fluid pressure field from map view (left column), and in 3D perspective (right column). Overall the simulation results show that the calculated fluid pressure encases an overwhelming majority of hypocenters for all profiles considered. These results provides very strong evidence that this model captures the essence of these aftershock sequences. Of additional interest, the 2009 L'Aquila North profile clearly shows that the gap in observed seismicity correlates with very low calculated fluid-pressure generation. Also note that L'Aquila South, and the origin of the mainshock hypocenter shows a persistent root of hypocenters that provide compelling evidence for upwards migrating fluids and likely the driver of the extensive foreshock activity recorded.

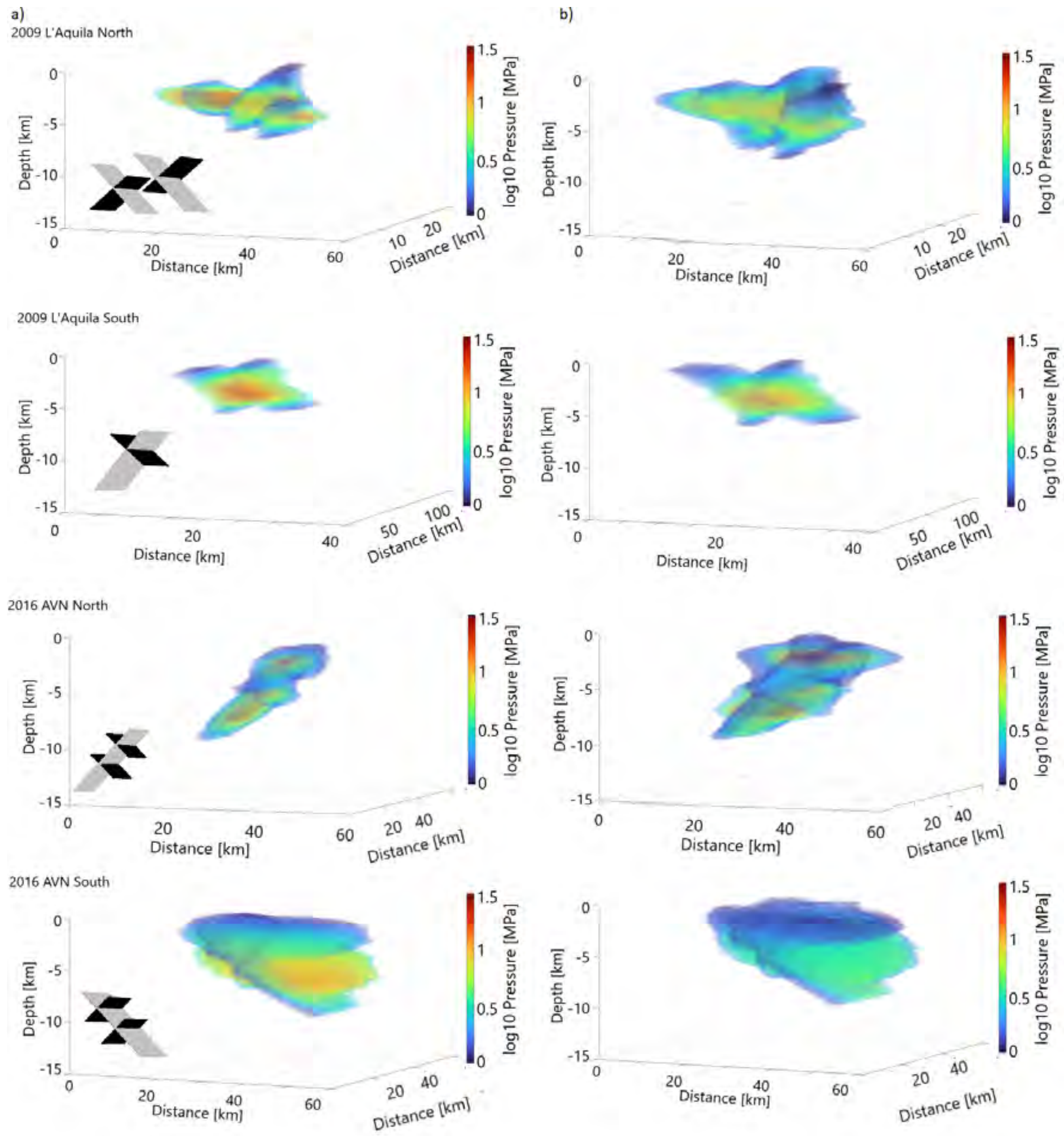

Figure 4.4: Calculated fluid pressure and subfigures showing fault orientation used. a) The first column corresponds to the fluid-pressure above hydrostatic before the beginning of the healing process for all four profiles. b) The second column shows the pressure above hydrostatic at the end of the simulation (200 days) for all four profiles. We generally observe a comparatively higher pressure value within the fault system, propagating along the lower permeable faults and their vicinity. At the end of the simulation, a wider range of fluid pressure and a decrease in pressure value is observed, consistent with the healing process. Although profile 3 (AVN North profile) shows a higher pressure value in the fault system that remains by the end of the simulation. See text for details.

Figure 4.6 shows observed cumulative aftershocks (blue) superposed with modeled cumulative aftershocks (red) for the four profiles across the study area over a

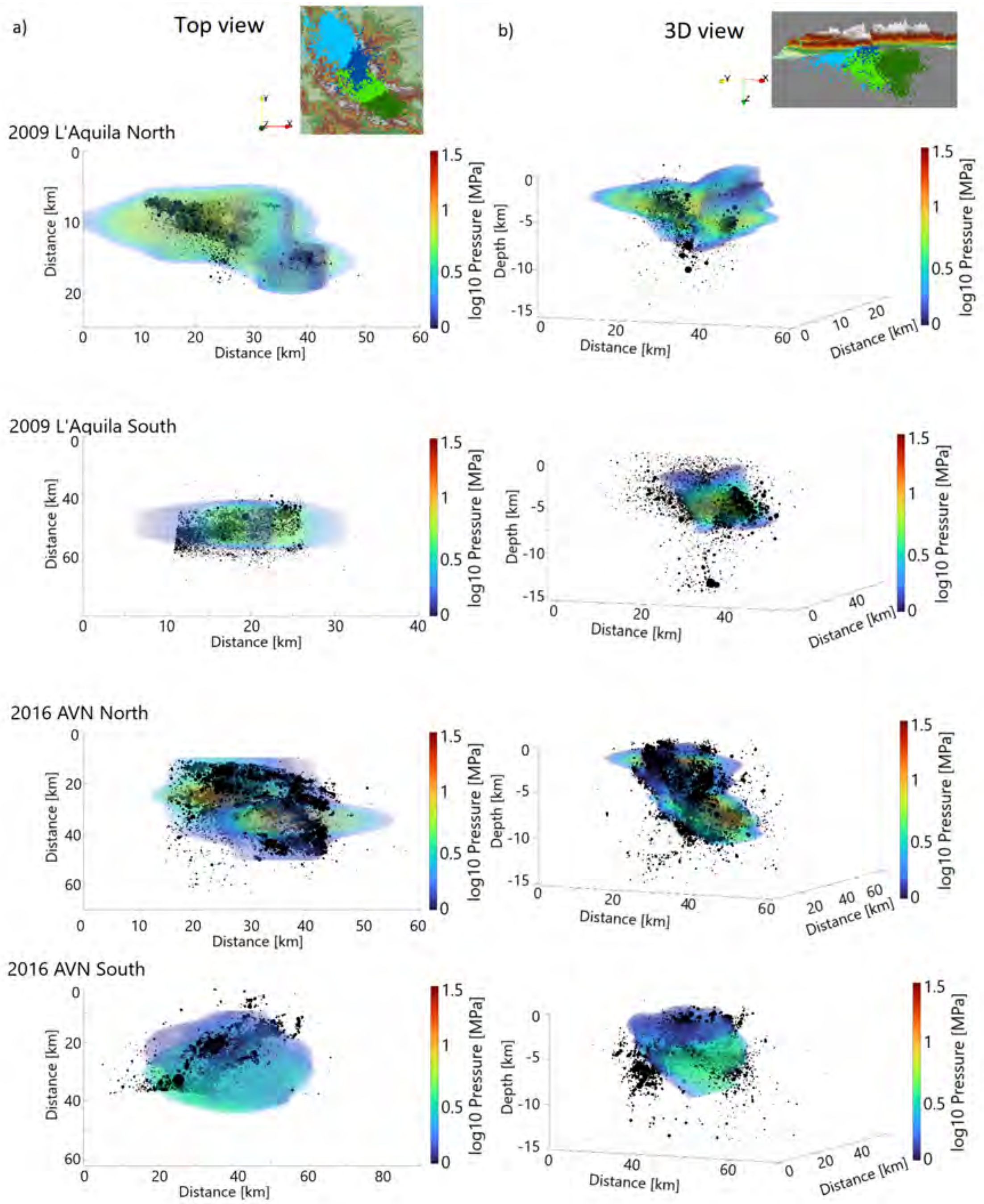

Figure 4.5: Spatial distribution of hypocenters superposed on the calculated fluid pressure field. a) The top view shows a strong correlation between the earthquake distribution and the area affected by the high-pressure fluid. b) The side view shows a strong correlation between the locations of the hypocenters and the calculated fluid pressure.

timescale of 200 days. The model results and observations show remarkable correlation. The dominant parameter, as discussed above, to control this aftershock production rate is the α value. The α value controls the permeability of pathways and the rate of internal CO_2 generation. Figure 4.6 shows the normalized cumulative number of aftershocks for each profile considered, with cumulative number of numerical aftershocks shown superposed. The stars in each figure indicate times of significant aftershocks. Figure 4.6a shows aftershock development over time for the 2009 northern L'Aquila profile indicating three significant earthquakes in the sequence, and not coincidentally the onset of an aftershock sequence. This three-phase sequence is captured in the model by varying α.

The 2009 southern L'Aquila profile (Figure 4.6b), on the other hand, is only characterized by one mainshock followed shortly by 5.4 event, resulting in a typical aftershock sequences usually empirically by Omori's Law because no additional fluid was generated. Figure 4.6c illustrates the temporal evolution of aftershocks from the 2016 AVN North profile, consisting of three significant events. The first M_w 5.3 event, according to our model, resulted in some internal fluid generation followed by a typical aftershock rate decay. About 70 days later, the two largest events of the entire AVN sequence occurred, and followed by a substantially greater aftershock rate, indicating the generation of significant internal fluid sources. This is modelled by including two phases for α. Figure 4.6d shows the temporal development of the aftershocks from the AVN South profile, consisting of four significant events spanning 200 days and modelled using four-phases for α.

The good agreement between model (blue) and observations (red), when combined with the spatial comparison of hypocenters and calculated fluid pressure field provides compelling evidence that this model captures the dominant physics of this system.

Figure 4.7a summarizes the α_j values varied in the simulations for each phase of each profile (blue shading). We discuss the behavior as $1/\alpha$ [days] for intuitive convenience. Profile one includes three significant earthquakes of M_w 5.0, 4.4, and 4.0, where the recovery duration decreases (from 40 to 20 to 5 days, blue shading) with decreasing number of earthquakes within the three phases (grey shading). Profile two, with only one phase but two major mainshocks within a short time period, reveals a permeability and source recovery of approximately 80 days, correlating directly to the number of earthquakes. Profile three initiated with a M_w 5.3 event and reveals a recovery time of $1/\alpha = 20$ days. In contrast, the production rate of the M_w 5.9 and 6.5 earthquakes correlates with very long recovery times 150 days (2nd phase), consistent with our hypothesis. The grey shading shows the number of aftershocks for each phase and which correlates with $1/\alpha$. Finally, profile four reveals a much smaller alpha value despite four large earthquakes. The first three phases show approximately less than five days of recovery each and a higher recovery time (approximately 30day) in the last phase. The last phase is related to the earthquake of M_w. 5.5 in January 2017. Again here, the number of aftershocks corresponds to the $1/\alpha$ values.

Figure 4.7b shows the numerical volume stimulated over the entire stimulation period, where stimulation is defined as a numerical gridpoint reaches the Mohr-Coulomb failure condition. Model results reflect the amount of CO_2 generated in the model, with L'Aquila south (green) showing a large initial increase that then relaxes to constant rate. L'Aquila North (purple), on the other shows stimulated volume increases in response to the significant aftershocks observed. However, the southern profile shows a much larger affected area than the northern profile because this hosted the hypocenter and the maximum co-seismic slip. AVN North (orange) stimulated a significantly larger volume than the AVN South (blue) because AVN North hosted the largest events in the entire earthquake sequence. The overlapping profiles (L'Aquila north and AVN south) show a similar amount of stimulated volume, because these events sampled the same lithological structures (Figure 1). However, the AVN south profile shows an additional stimulated volume on simulation day 150 that correlates with the January 2017 earthquakes, and which filled the seismic gap that existed between 2009 and 2016.

These results suggest that future InSAR or other co-and post-seismic deformation studies may identify the consequences of these stimulated volumes and their healing.

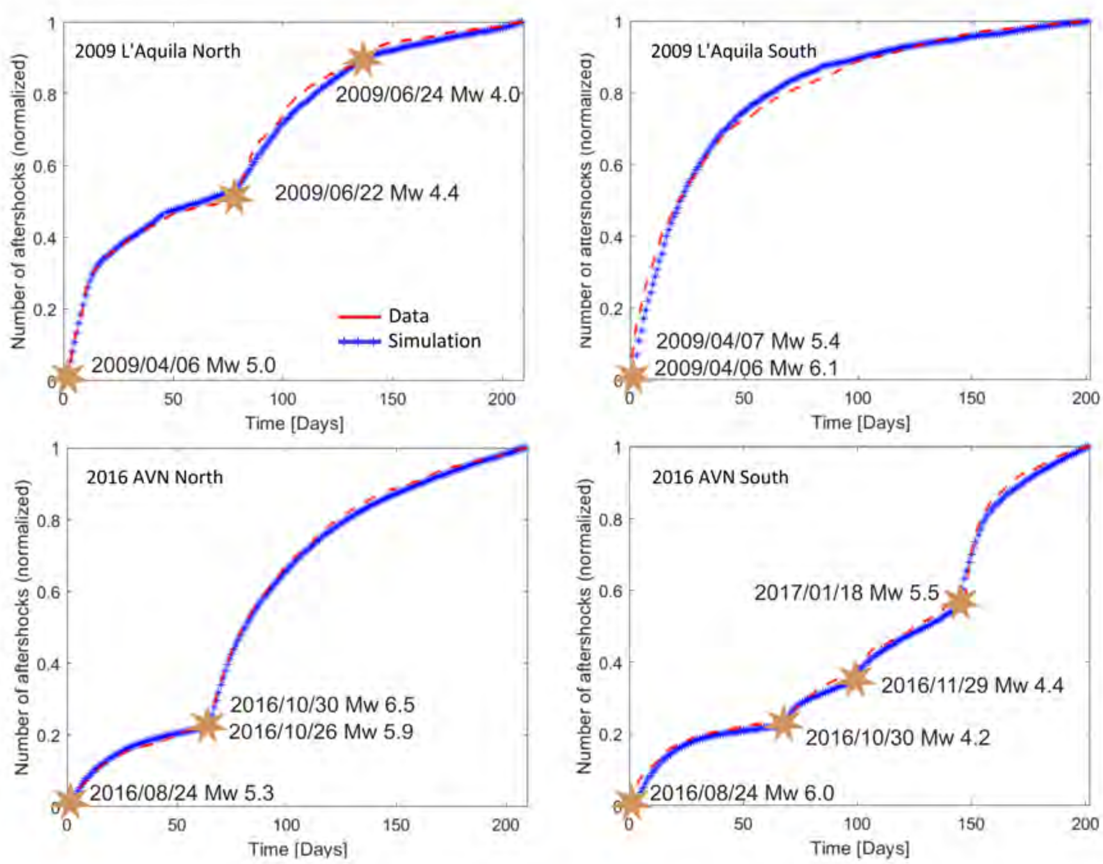

Figure 4.6: The temporal variation of earthquakes within 200 days shows excellent agreement with the numerically triggered earthquakes. All profiles in this study were initiated by the main earthquake. Over time, a few more main earthquakes resulted in additional aftershocks. Each of the main earthquakes defines the beginning of a new phase. The temporal variation is achieved by adjusting the α value that controls the permeability and source dynamics in each phase

.

4.6 Discussion and Conclusion

Deeply trapped and internally generated high-pressure fluid diffuses along permeable paths and subsequently reactivates faults that drive thousands of seismic events [Sibson, 2007, Miller, 2020, Gunatilake and Miller, 2022]. This behavior is observed for both the 2016 Amatrice-Visso-Norcia earthquake sequence and the 2009 L'Aquila earthquake sequence. These two earthquake sequences produced more than 53,000 aftershocks within 200 days. Several major earthquakes have been recorded repeatedly during this progression, which co-seismically generates internal sources (CO_2).

Using a 3-dimensional model of non-linear diffusion with a source term, we successfully reproduced the temporal aftershock production rates with a strong corre-

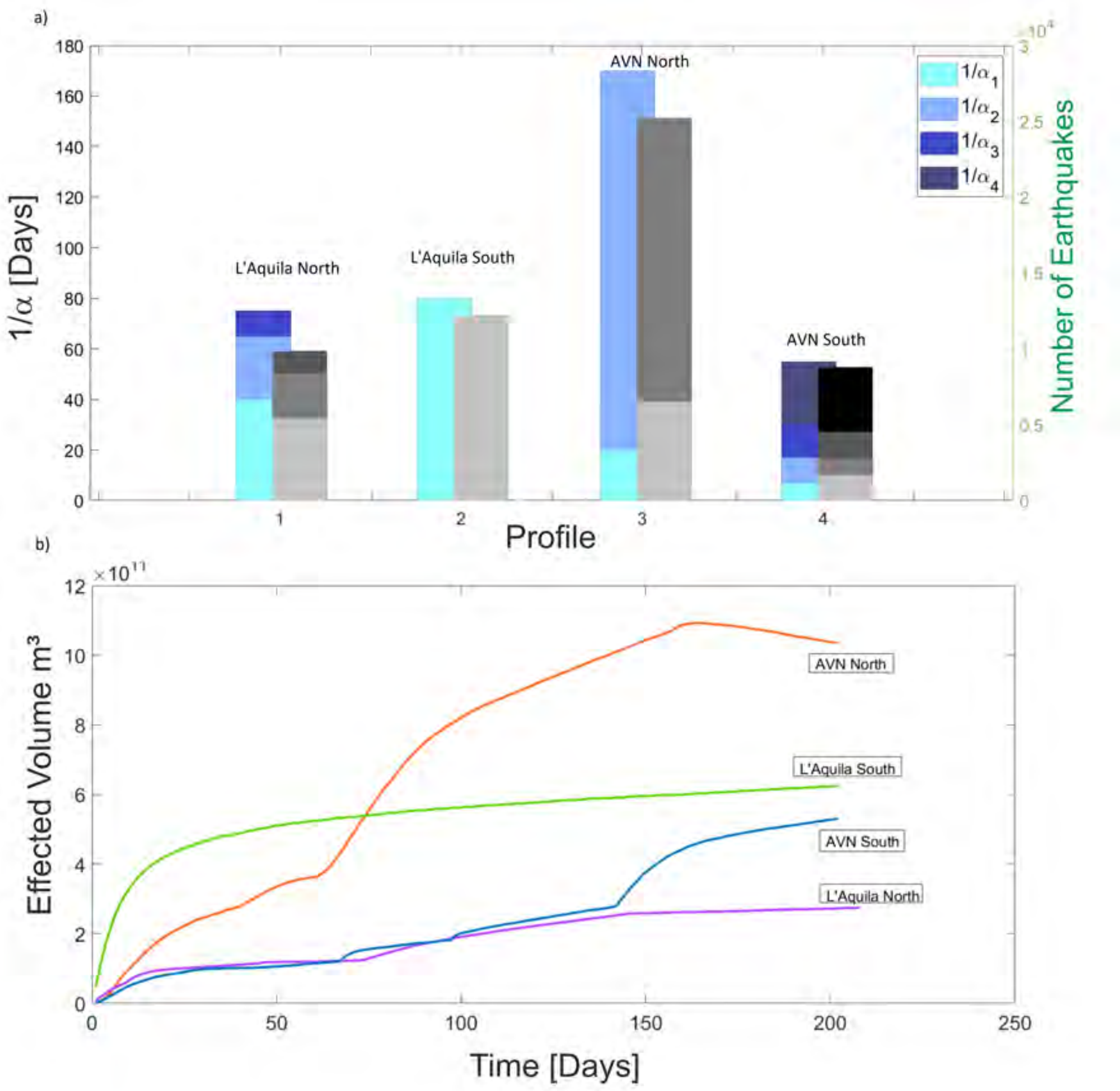

Figure 4.7: Summary of α values and stimulated volume of the study area. a) Alpha values defined for each profile phase are summarized in grey shading. The first and second shows similar alpha values, whereas the third profile (AVN north) shows a very high alpha value, during the second phase. The fourth profile (AVN south) with just one mainshock indicates a smaller alpha value. Interestingly, the alpha values used to fit the data correlate with number of earthquakes recorded at each phase (blue shading). b) The stimulated volume during these simulations reflects these alpha variations. The most affected areas are around the northern AVN and southern L'Aquila profiles. See text for details.

lation between numerically triggered and recorded seismic events.

Furthermore, the 3-dimensional model of calculated fluid over-pressure and the hypocentral locations of thousands of well-located aftershocks shows very strong correlation. In all simulations, we observe a high-pressure source within the fault system that diffuses along the fault and into its surrounding. These results were obtained by controlling the permeability network and the internal generation of fluid sources from the thermal decomposition of the carbonates in the Apennines. Both terms are regulated by varying one parameter, namely α over the time considered, which controls the permeability of the dynamics flowpaths as well as the internal generation of fluid. Lower $1/\alpha$ values indicate a less vigorous CO_2 reservoir at depth compared to the higher $1/\alpha$ value.

The L'Aquila North initiated with a M_w 5.0 earthquake on April 6th, 2009, and continued with M_w 4.4 and M_w 4.0 earthquakes and experienced more than seven thousand aftershocks. L'Aquila South, which hosted the M_w 6.1 mainshock and M_w 5.4 largest aftershock, generated more than twelve thousand aftershocks. According the model, both regions recovered after about 75-80 days. AVN North, which hosted the largest earthquake ($M_w 6.5$) in the sequence, generated two significant aftershocks ($M_w 5.3$, $M_w 5.9$), and produced more than twenty five thousand aftershocks in the first 200 days. In contrast to the L'Aquila sequence, the AVN North sequence continued to generate fluid with each significant aftershock and reflected in the model as long recovery times ($1/\alpha = 150$days). AVN South, on the other hand, initiated with a magnitude $M_w 6.0$ earthquake on August 24th, 2016, followed by subsequent large aftershocks ($M_w 4.2$ and $M_w 4.4$ and $M_w 5.5$), and experienced nearly nine thousand aftershocks in the first 200 days. This profile showed a total recovery time of 50 days, which is more or less consistent with the overlapping L'Aquila North area. The comparison of the numerically-determined affected volumes for each area shows that the northernmost study area (including the town of Norcia and Visso) was mainly affected by the internal generation of CO_2 and likely also mobilized trapped high pressure reservoirs at depth. The MST fault interestingly bounds the AVN North and AVN South areas, which has been suggested to act as a hydraulic barrier between these two regions [Gunatilake and Miller, 2022].

Our simulation results show that the overlapping L'Aquila North and AVN South (including the city of Amatrice) sequences stimulated a similar volume until 150 days. At 150 days, AVN South was re-stimulated by a swarm of aftershocks ($M_w 4.2$ and $M_w 4.4$ and $M_w 5.5$), which generated their own aftershock sequences and resulted in an increase of affected volume. Interestingly this sequence filled the seismic gap between between the 2009 sequence and the 2016 sequence. All of the four areas studied are entirely consistent with the internal generation of CO_2, and results suggest a clear scaling between earthquake magnitude and volume of fluid produced.

In this study we developed and numerically explored a 3-dimensional non-linear diffusion model with a source term approximating fluid generation by thermal decomposition. The very satisfying spatial and temporal comparisons between model results and observations of more than 50,000 well-constrained aftershocks strongly suggest that this model captures the dominant physic driving aftershocks in the Apennines. These results have potentially far-reaching implications in earthquake physics.

Chapter 5

Dynamics between earthquakes, volcanic eruptions, and geothermal energy exploitation in Japan

5.1 Abstract

Active volcanoes provide the richest geothermal energy sources because the intruding magma brings high temperatures close to the surface, thus offering possibilities for harnessing large amounts of heat for geothermal exploitation. The largest geothermal power plant in Japan, the Hatchobaru plant (capacity 112 M_w) is located near the Otake geothermal power plant with a capacity of 12.5 M_w. These geothermal power plants exploit high-temperature steam of Mount Aso, the largest volcano in Kyushu that showed frequent activity from February to April 2016 and erupted in October 2016. During this sequence, three successive large earthquakes (called the Kumamato sequence) occurred in April 2016 and followed by tens of thousands of aftershocks in the following year, likely driven by degassing of high pressure CO2. This unambiguous related volcanic activity and the earthquake sequence requires physical and quantitative explanations and is numerically explored using a non-linear advection/diffusion model of pore pressure and heat flow. The aim is to investigate the influence of earthquake/volcanic activity on the future productivity of nearby geothermal power plants to determine whether the activity is detrimental or beneficial to energy exploitation. Model results show excellent spatial and temporal correlation between modeled earthquake locations and aftershock decay rates along the entire sequence, showing that seismic activity opened pre-existing vertical cracks providing pathways for the ascending magma. The results also show that an increase in CO_2 pressure and temperature on the southwestern side of the caldera would have benefited power production at the nearby geothermal power plants in 2016, but earthquake destruction of the power line network prevented capitalizing on these hydro-thermal-mechanical processes. Interestingly, the Aso volcano in south-

ern Japan erupted in October 2021 and may have enhanced future local geothermal power generation. This smaller but still significant eruption of Mount Aso, was not accompanied by significant seismicity, indicating a vigorous and active system and a possible (and perhaps significant) increase in future geothermal power production.

Keywords: Geothermal energy potential; Kumamato earthquake sequence; fluid-driven aftershocks; thermo-hydro-mechanical processes; advection-diffusion thermal model; Mathematical, physical, and numerical modeling;

5.2 Introduction

Geothermal power plants close to active volcanic structures benefit from the elevated geothermal gradients [McCoy-West et al., 2011]. However, volcanic activity is often associated with fluid triggered earthquakes with numerous aftershocks [Miller et al., 2004, Walter et al., 2007, Seropian et al., 2021, Jousset et al., 2013]. Japan is situated on the Pacific Ring of Fire and is known for its active volcanoes in a complex tectonic environment, in which the Pacific and Philippine plates are subducting beneath the Okhotsk and Eurasia plates at rates of 8–9 cm/yr and 5–6 cm/yr, respectively [Kato et al., 2016, He et al., 2019, Bird, 2003]. Over the years, destructive earthquakes have been recorded along the subduction zone as well as shallow crustal earthquakes away from plate boundaries as a result of internal deformation of tectonic plates. Figure 5.1 shows the well-located 2016 Kumamoto earthquake-aftershock sequence on Kyushu Island in southwestern Japan compiled by the Japan Meteorological Agency (JMA). This sequence started on April 14 with a M_w 6.2 event at a hypocentral depth of 9 km, followed by another major earthquake (M_w 6.0) on April 15 along the northern part of the Hinagu fault at a depth of 8 km [Shirahama et al., 2016, Yagi et al., 2016]. On April 16, 2016, another earthquake (M_w 7.0) at a depth of 10 km was recorded along the active Futagawa Fault and designated the mainshock of this sequence [Yoshida et al., 2016, Hashimoto, 2020].

Simultaneously, volcanic activity was recorded in the Aso Caldera, one of the largest active volcanoes in the world and with a cross-sectional area of 380 km^2. This volcano is known for pyroclastic eruptions, including ash emissions, strombolian eruptions, and phreatomagmatic activity [Lin, 2017]. Previous studies revealed volcanic activity directly before and after the Kumamoto earthquake sequence, opening preexisting vertical cracks and allowing magmatic fluid to ascend [Nimiya et al., 2017]. Exsolution of high pressure gasses from the magma creates the pathways for the rising viscous magma [Wilson and Head Iii, 2007]. Volcanic eruptions then occur as a result of increased pressure in a shallow magma reservoir caused by upwelling fluids from a deep magma chamber [Shapiro et al., 2017]. The Aso volcano erupted about 7 hours after the April 14th main shock and continued its activity until October 8, 2016, where a major eruption occurred and discharging 15,000 tons of SO_2 [Morita, 2019, Song et al., 2019]. The seismic activity decreased after the October 8th eruption, indicating reduced pressure within the system.

The Hatchōbaru geothermal power plant capitalises on the high geothermal gradients in southern Kyushu [Himematsu and Furuya, 2020, Tanaka et al., 2004] and has been in operation since 1977. It is the largest geothermal power plant in Japan with a capacity of 112 M_w. The neighboring Otake Power Plant with a capacity of 12.5 M_w has been in operation since 1967 [Hirowatari, 1991, Taguchi and Nakamura, 1991, Ishitsuka et al., 2016]. The geothermal reservoir is located at depths between 500-1500 m at fluid temperatures ranging from 290-300°C [Fujino and Yamasaki, 1984, Manabe and Ejima, 1986].

Previous studies revealed the importance of fluid pressure on the entire 2016 Kumamoto earthquake aftershock sequence, based on co-seismic stress changes, inversion analysis of pore fluid pressure, with multiple geophysical investigation including resistivity structures and tomographic imaging [Nakagomi et al., 2021, Aizawa et al., 2021, Wang, 2019].The aim of this work is to numerically investigate possible effects of the Kumamoto earthquake and the subsequent volcanic eruption on the geothermal power plants in close vicinity of the Aso Caldera. The model, described in detail below, investigates hydraulic behaviour using a model of non-linear pressure diffusion with a source term coupled with an advection-diffusion thermal model. Fluid pressure diffusion and its influence on aftershock genesis, heat flow and its contribution to geothermal exploitation potential, and importantly the October 2021 volcanic eruption and how it might affect future geothermal power production is explored.

5.3 Geological Setting and Model Setup

Aftershocks of the Kumamoto earthquake occurred between Kumamoto City and the Aso Caldera located in the Beppu-Shimabara Trench (BST), a NE-SW volcanic belt that runs across central Kyushu [Lin, 2017, Ishimura et al., 2021]. This graben is characterized by numerous east-west trending normal faults and volcanic activity [Mitsuoka et al., 2020, Hirowatari, 1991]. The Aso caldera has a diameter of 24 km in the north-south direction and 18 km in the east-west direction [Scott et al., 2018, Handa et al., 1992]. In particular, the central cone, the Nakadake volcano with a composition ranging from basalt to basaltic andesite [Morita, 2019] is an active volcano that erupts frequently [Ozawa et al., 2016].It showed an increased level of activity during the Kumamoto earthquake sequence, compared to previous and subsequent years [Uchide et al., 2016]. This casual relationship occurs when Phreatic eruptions of high-temperature volcanic fluids (gases or magma) contact shallow groundwater in a closed system under low-permeability rock, disturbing the hydrothermal system and producing intense seismic activity [Stix and de Moor, 2018, Zhao et al., 2018]. A time history of volcanic activity and seismic events from 2013 to 2019 is shown in the supplementary.

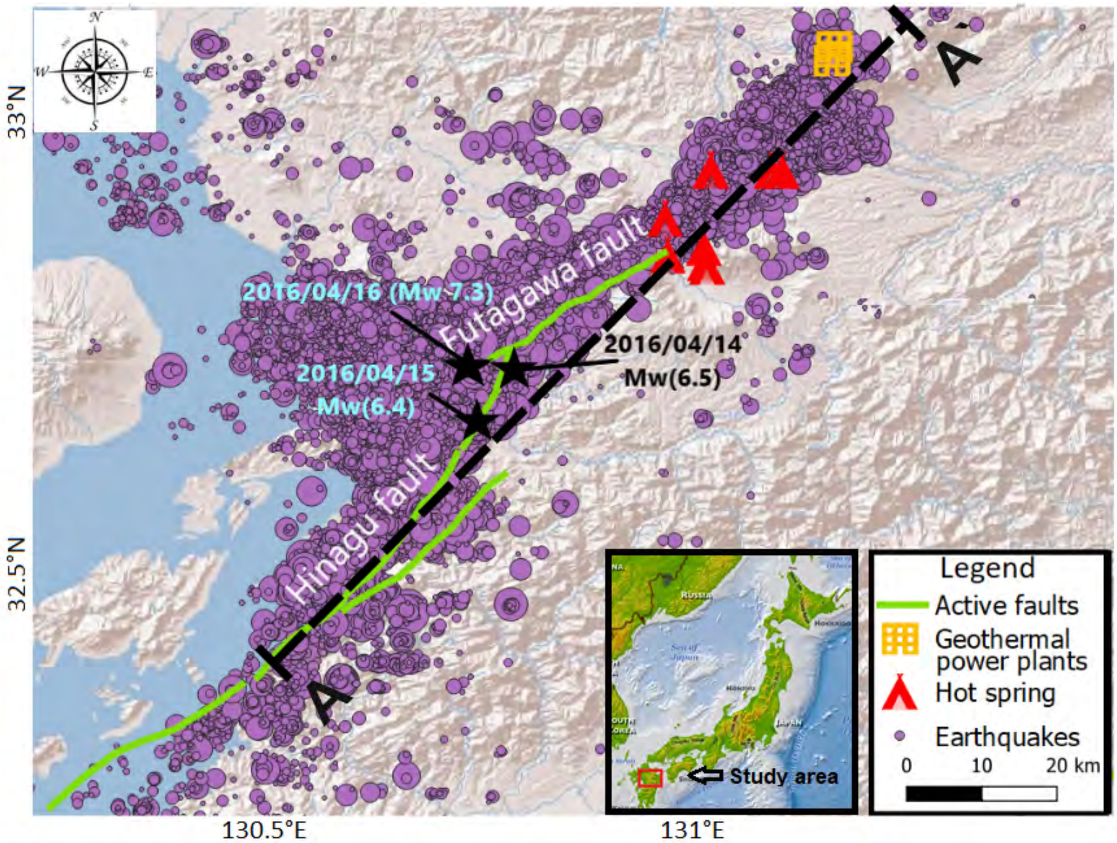

Figure 5.1: Digital elevation model of the study area, including hypocenters (purple dots) of 50.406 aftershocks from the Kumamoto earthquake sequence 2016 in southern Japan. Circle sizes relates to earthquake magnitude. Red symbols show volcanic hot springs of the Aso caldera and Geothermal Power plants (Hatchōbaru and Otake) in yellow.

Figure 5.1 shows more than 50,000 seismic events ($M_w > 1$) in the year following the April 14th, 2016 Kumamoto earthquake and the ENE-WSW-oriented Futagawa and SWS-NEN-oriented Hinagu faults that ruptured during the event. This right-lateral strike-slip fault system is one of the major active fault systems on Kyushu Island [Mitsuoka et al., 2020, Ishimura et al., 2021, Kobayashi, 2017]. Finally, Figure 5.1 presents volcanic hot springs of the Aso caldera and two geothermal power plants, located close to the caldera.

A conceptual model of the study area was derived from electrical resistivity inversions performed at the active crater of the Nakadake central cone of Aso volcano using audio frequency magnetotellurics (AMT) [Matsushima et al., 2020]. The crustal structure beneath the Aso caldera, is characterized by pre-Neogene basement rocks and Quaternary volcanics inferred from a low-resistivity (1–10 Ωm) signal. Seismic inversion studies and tomographic data confirm this sequence [Sudo and Kong, 2001, Unglert et al., 2011].

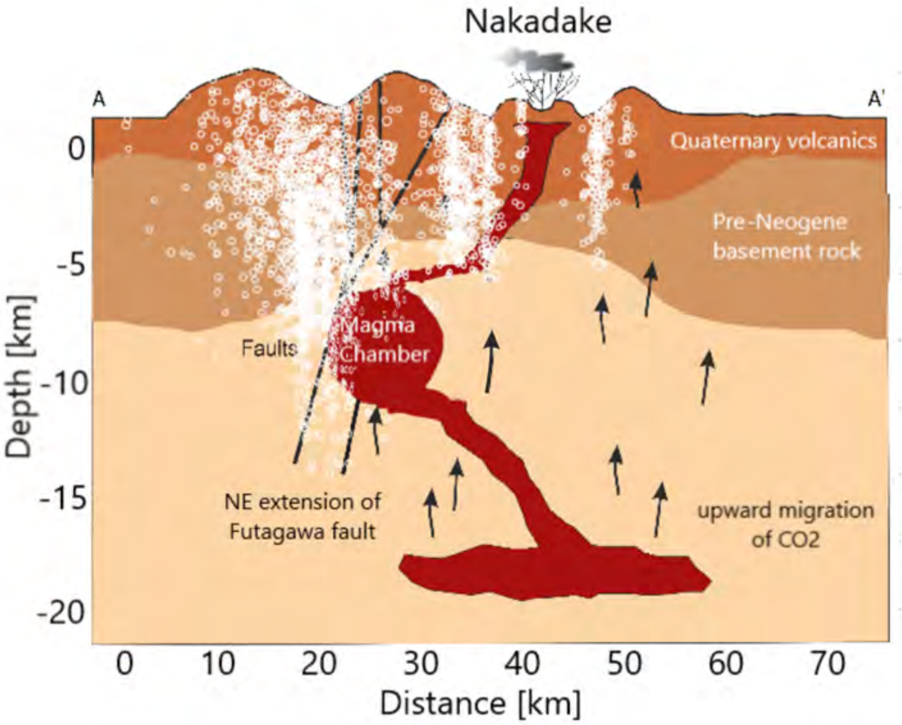

Figure 5.2: Conceptual model for the study area along profile A-A' (Fig. 5.1) based on previous geophysical investigation. The aftershocks of the 2016 earthquake sequence with $M_w > 2.5$ (white) is superposed to the conceptual model.

Further geophysical observations reveal a conductive zone that dips steeply to the north-northeast, which is highly fractured, and is filled with acidic hydrothermal fluids [Matsushima et al., 2020, Kanda et al., 2019]. These fluids are transported from the low-lying main magma chamber into the Nakadake crater [Shinohara et al., 2018]. The core of the magma chamber is located at a depth of 5-6 km below the

Aso caldera with an almost spherical shape of radius of 2 to 3 km and a volume of about 100 km^3 [Abe et al., 2010, Tsutsui and Sudo, 2004]. However, this chamber cannot explain the massive volcanic eruption of ejecta, which covered more than 600 km^3 of space 90,000 years ago [Ono et al., 1995].

Recent studies of petrological analyses provide insight into the ongoing degassing process and revealed an over-pressurized magma chamber at a depth of 6 to 11km caused by gas accumulation [Niu and Song, 2021, Kawaguchi et al., 2021]. Previous studies discovered another low-velocity layer at depths between 10 and 24 km below the southwestern part of the caldera [Sudo and Kong, 2001, Abe et al., 2010]. Based on those geophysical studies, figure 5.2 shows a conceptual model of the study area, with the three different lithological units, the magma chamber, the fault system (to the southwest of the magma chamber) and micro fractures (to the northeast of the magma chamber). The orientation of the faults is constrained by both the recorded 2016 Kumamoto earthquake-aftershock sequence and dip angles and slip distribution of the faults presented in other studies ([Wang, 2019, Fukahata and Hashimoto, 2016]. The geometry of the model is secured by geophysical observations, especially through seismic and electrical resistivity studies [Hata et al., 2016, Kanda et al., 2019]. Therefore, the environmental setting shown in Figure 5.2 is used as the geological background model for the numerical simulations in this work. Figure 5.2 also shows the 2016 Kumamoto seismic sequence superposed on the conceptual model and suggests a correspondence of earthquake locations with the identified fault structures on the southwestern side of the magma chamber. The seismicity on the northeastern side of the magma chamber agrees with the identified micro fractures. Thus, the conceptual model coincides with the dynamics of the earthquake propagation and formed the basis if this study.

5.4 Methods - Mathematical and Numerical Model

For completeness, the physical and numerical model is briefly described below, although a more detailed description can be found elsewhere [Miller, 2020]. The mathematical model is based on diffusion of fluid pressure in a porous medium and is governed by:

$$\frac{dP}{dt} = \frac{1}{\phi\beta}\nabla\cdot\left[\frac{k}{\eta}\nabla P\right] + \frac{S}{\phi\beta} \tag{5.1}$$

where P is fluid pressure [Pa] above hydrostatic, t is time [s], ϕ is porosity [-], β is

the lumped compressibility of pore space and fluid [Pa^{-1}], k is permeability [m^2], η is fluid viscosity [Pa s], S is a source term [s^{-1}],
Permeability is further defined as:

$$k = (kc_0 + d \cdot exp(-\alpha_j t_j)) \cdot exp(-\sigma_e/\sigma^*) \tag{5.2}$$

where kc_o is a baseline permeability, α [s^-1] is the parameter controlling the permeability recovery for the duration t [s] and σ^* [Pa] constrains the permeability response to the effective normal stress σ_e [Pa]. Permeability recovery is related to chemical precipitation and tectonic stresses reducing the permeability over time [Miller, 2020].
The source term S is written:

$$S = Q_0 e^{-\zeta t} \tag{5.3}$$

where Q_0 [s^{-1}] is introduced along activated faults to mimic decarbonization and dehydration, and ζ determines the timescale t of this internal source generation. Decarbonization and dehydration describe the release of large amounts of CO_2 and water at timescales similar to the ones of the permeability recovery [Mitchell and Faulkner, 2012, Miller, 2020]. Therefore, I assume $\alpha_j = \zeta_j$ in both the permeability and source terms minimizing the number of free parameters.

The Darcy velocity q [m/s] is,

$$q = \frac{-k}{\eta} \nabla P \tag{5.4}$$

which is used to calculate the advective heat transport term in the diffusion advection equation:

$$\rho c_p \frac{dT}{dt} = \lambda \nabla^2 T - \phi(\rho c_p)_f v \nabla T \tag{5.5}$$

where c_p is specific heat capacity [J/kg/°C], T is temperature [°C], v is pore fluid velocity ($v = q/\phi$) and λ is thermal conductivity [W/m/°C] of the fluid-solid system. Local thermal equilibrium is assumed. Thus, specific heat capacity and density on the right-hand side of the equation are system parameters, so fluid and rock properties weighted by porosity, similar to the thermal conductivity. After the weighting parameter variation for the different rock types is negligible, therefore, thermal conductivity is assumed homogeneous. The advection term on the right-hand side only incorporates fluid parameters as only the fluid is flowing relative to the porous matrix [Kolditz, 1995].
A simple model of mechanics is assumed, whereby a random distribution of incip-

ient slip planes relative to principal stress directions is scattered throughout the numerical domain. The random distribution mimics heterogeneity around an optimal orientation of the slip planes at 45 degree [Miller, 2015]. The effective normal stress on incipient slip planes is calculated as:

$$\sigma_n = \frac{\sigma_1 + \sigma_3 - 2P_f}{2} - \frac{\sigma_1 - \sigma_3}{2}\cos(2\theta) \tag{5.6}$$

where σ_1 is vertical and σ_3 is the minimum horizontal principal stresses [Pa] since the geological setting is a characterized by numerous normal faults, θ is the randomly distributed angle relative to the maximum principal stress, P_f is the fluid pressure above hydrostatic. A normal distribution of 45 degree and a standard deviation of 8 degree is assumed for the fault orientations (θ). Note that σ_3 is out of plane and assumed to be 0.62 $\cdot\sigma_1$ to reflect the extensive environment [Miller et al., 2004]. The shear stress τ on the virtual planes are:

$$\tau = \frac{\sigma_1 - \sigma_3}{2}\sin(2\theta) \tag{5.7}$$

A numerical aftershock is defined as a nodal grid point reaching the Mohr-Coulomb failure condition:

$$\tau \geq \sigma_n \mu \tag{5.8}$$

where μ is the friction coefficient [-].

The time and location of a each triggered numerical aftershock is recorded, and only one event is permitted for each computational node. Equations 5.1 (pressure diffusion) and 5.5 (Heat advection-diffusion) are solved numerically using implicit finite differences on a regular grid of 300x300 nodal points. No-flow boundary conditions are imposed on the side and bottom boundaries for the hydraulic model, and a constant hydrostatic pressure at the surface. The model includes a temperature-dependent viscosity for supercritical CO_2 with a value of $\eta = 1e^{-4}$ Pa s at the surface, resulting in $\eta = 1e^{-5}$ Pa s at the depth of the fault system. Following [Segall and Rice, 1995] a lumped compressibility of fluid and pore space is assumed and with a value of $\beta = 4e^{-9}$ Pa^{-1}. Both parameters are in the range of supercritical CO_2 at relevant temperature and pressure values shown elsewhere [Sulem and Famin, 2009].

CO_2 degassing in magma controls the eruptive power of volcanic systems due to rapid decompression of the rising magma. The magma ascending in a conduit

Symbol	Quantity	Value	Unit
β	Pore compressibility	$1e^{-10}$	1/Pa
c_p	Rock heat capacity	1.02	J/k/°C
λ	Thermal conductivity	0.6	W/m/°C
ρ_r	Rock density	2700	kg/m^3
ρ_f	Fluid density	900	kg/m^3
μ	friction coefficient	0.8	-

Table 5.1: Fluid and rock parameters used in the numerical model.

is decompressed and volatiles dissolve as bubbles in the magma. As the bubbles in the magma grow during decompression, an interconnected bubble network forms through which permeable degassing can occur [Christenson et al., 2015]. Consequently, a porosity of 0.5 for the magmatic fluid is assumed [Lamy-Chappuis et al., 2020]. A porosity of 0.03 is assumed for the rock matrix [Schön, 2011]. Finally, σ^* is assumed to be 35 MPa [Miller, 2020]. Permeability is constrained by laboratory experiments on ejected material and showed a permeability of $2.5e^{-13}$ m^2 [Namiki et al., 2018]. Table 5.1 list all other fluid and rock parameters used in the model.

For the heat transport, I assume a background geothermal gradient of 50°C/km, while the viscous magma chamber is assumed to be range from 140°C to 1000°C at 10km depth. Temperature at the top boundary is set to 30°C in general, but to 140°C around the Nakedake volcano crater [Sudo and Hurst, 1998, Terada et al., 2012]. Zero thermal flux boundary conditions are assumed for the left, right and bottom boundaries. The steady state background model in combination with the zero flux boundary condition results in a constant temperature at the lower boundary.

I assume and apply an initial 40 MPa fluid overpressure pressure within the chamber and maintain the pressure until the October 8th, 2016 the volcanic eruption. The imposed pressure temperature field diffuses to a steady state before starting the simulation. At time=0 (corresponding to 15. April 2016) a source term $Q_0 = 10^{-9}s^{-1}$ is imposed on the activated faults and in the magma chamber to simulate the degassing process of an active volcanic systems. Based on literature sources and previous studies, the only unknown value is α_j. To obtain this value, the parameter is varied during simulations of the 2016 Kumamato earthquake sequence and is constrained by this data.

5.5 Results

Simulations run for 365 days, which covers the duration of the aftershock sequence from April 2016 and volcanic eruption until volcanic silence in April 2017. Figure 5.3 a shows the initial equilibrium pressure field at the start of the simulation. Figures 5.3 b-c include the first phase of the Kumamoto earthquake sequence and the volcanic eruption on the 8th of October. Figures 5.3 d-e show the calculated fluid pressure field from the end of the eruption until the overall cessation of significant seismicity. Pressure diffuses from the high-pressure magma chamber into the fault structures and tends to migrate both upwards and downwards along the faults. The simulation results of day 155 (one day before the eruption) reveals an increase in pressure within the fault structures southwest of the caldera (Figure 5.2), which triggers the subsequent seismicity. Figure 5.3 d shows the decreased conduit pressure consequently reducing the pressure in the faults, due to volcanic eruption. At the end of the simulation (Fig. 5.3 e), a further decrease in the pressure gradient within the fault structure and conduit is observed, although an overpressure of about 20 MPa leads to further seismicity. Figure 5.3 f shows the Darcy velocity vectors from the pressure field (equation 5.4) at each nodal point at 150 days. The flow vectors show both upwards and downwards flow and reflects the migration of fluid pressure along the conduit and its surrounding. The flow downwards is a result of a fault cutting the magma chamber and instigating a fluid pressure gradient towards the depth. Additionally, the fluid pressure migrates along the conduit and expends to its surrounding. The observed seismic activity in the northeastern and southwestern part of the Nakedake volcano can be explained by the fluid-pressure increase along the fault structures and the conduit.

Figure 5.4 a shows observed cumulative aftershocks (black) superposed with modelled cumulative aftershocks (red) for the profile A-A' across the study area. It shows good agreement, which is achieved by varying the dominant parameter in the model, α, that appears in both the permeability (Equ. 5.2) and source pressure (Equ. 5.3). When tectonic stresses shut down the permeability network created by the earthquake/aftershock, the healing process begins. Conceptually, α reflects the duration needed for the permeability to heal and the timescale of the source generation [Miller, 2020]. The value for α is constrained by the data and shows a recovery time $1/alpha = 100$ days. Figure 5.4 b shows the calculated fluid pressure field (at 365 days) and recorded seismic data (white) superposed with the numerically triggered earthquakes (gold). The evolved fluid pressure field is controlled by

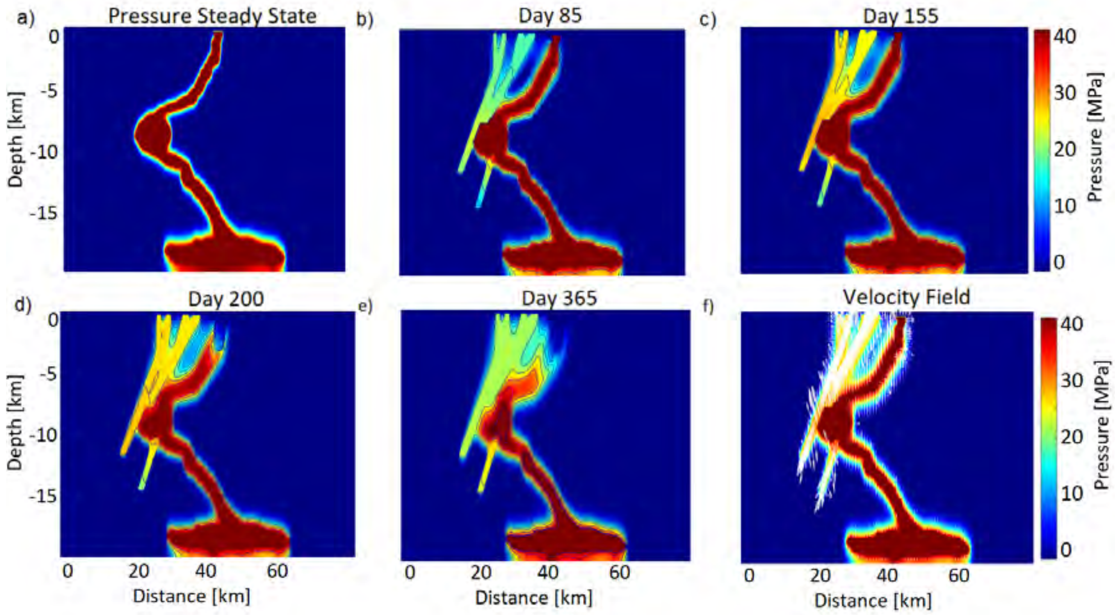

Figure 5.3: Calculated fluid pressure. a) The steady state pressure distribution at the beginning of the simulation. b-c) The fluid pressure is increasing within the faults toward the surface. d-e) After the massive volcanic eruption on October 8, 2016, the fluid pressure decreases. The contour lines clearly illustrate these changes along the model. f) The velocity field reflects the stream of the fluid pressure through the porous medium and show both the pressure propagation into the lower part of the chamber along the faults and into the upward oriented faults, allowing the rising of magmatic fluid towards the surface.

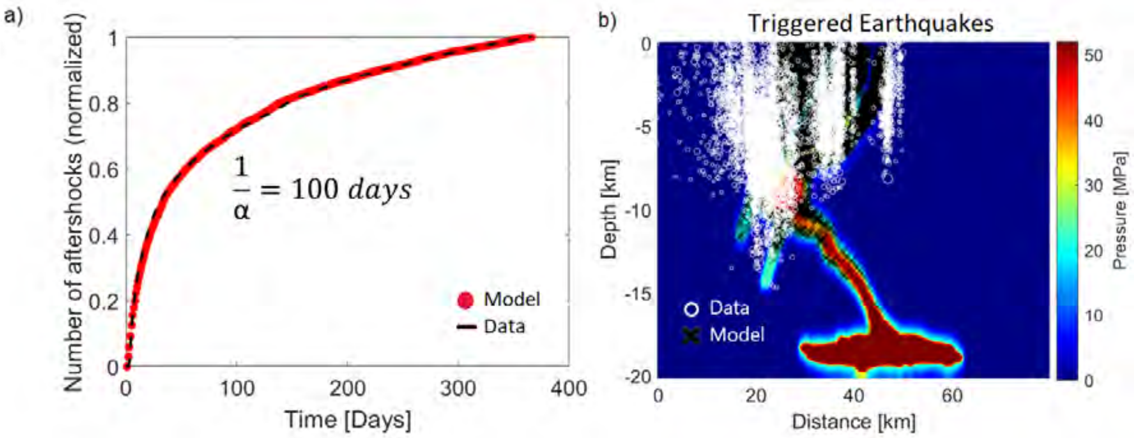

Figure 5.4: Temporal and spatial comparison. a) Comparison of observed cumulative aftershocks for the profile A-A' with numerically triggered earthquakes shown superposed. The data constrains the value of α, which in this case is $1/\alpha = 100$ days. b) Comparison of spatial distribution of the recorded seismic data (white) and numerically triggered hypocenters (black).

the permeability dynamics within the model, which is controlled by α. The fluid pressure increases within the fault structure and around the conduit and trigger earthquakes at the corresponding nodal points. These results compare very well with Figure 5.2, which shows the 50,000 aftershocks detected from the Kumamoto earthquake. These results, using a simple model and fault system, indicate that this model captures the dynamics between volcanic eruption and seismic activity. The entire spread of fluid pressure, temperature and fluid velocity field throughout the simulation is attached as a video in the supplementary.

Figure 5.5 a shows the temperature field in a steady state before the start of the simulation, reflecting a slight temperature rise in the predefined magma conduit. A gradual increase in temperature is observed within the conduit and fault system, indicating an advection-dominant heat transport process for various time steps. At day 85 (Fig. 5.5 b), heat is transported away from the chamber as it migrates upwards along the faults (Fig. 5.5 b-c). 5.5 d shows the temperature distribution at the end of the simulation (day 365), indicating the temperature near the surface around the volcano has increased from 30°C to roughly 160°C. Ubiquitous heat transport to the northeast and southwest can be observed, which would directly impact geothermal exploitation potential. The direct temperature increase around the geothermal power plants is obviously limited. Note that microfractures in the northeast are not implemented, but this would create additional pathways for heat transport towards the geothermal power plants. The comparably small temperature increase outside of preferential pathways is in agreement with other thermo-hydro-mechanical models of natural seismicity [Heinze et al., 2017b].

An examination of vertical profiles (V1-V8) and horizontal profiles (H1-H6) at a depth of 3 km quantifies the temperature evolution at various observation points along the fault structure (Fig. 5.6 a). Figure 5.6 b shows the temperature variations for the horizontal locations, and much more diversity compared to the vertical locations. Locations H1 to H5, within the fault structure, show a rapid increase in temperatures over the simulated time span. H6 located in the vicinity of the geothermal power plants shows slight temperature increase (10°C) Figure 5.6 c quantifies temperature profiles, aligned along the fault from bottom to top, and shows significant temperature increases due to advective heat flow. As expected, temperature cools towards the surface but all locations experience significant temperature increases in the southwestern part of the system. Figure 5.6 c also shows a fairly rapid temperature increase that stabilizes over the simulated time. In general, the temperature increased up to approximately 75-100°C at each depth investigated.

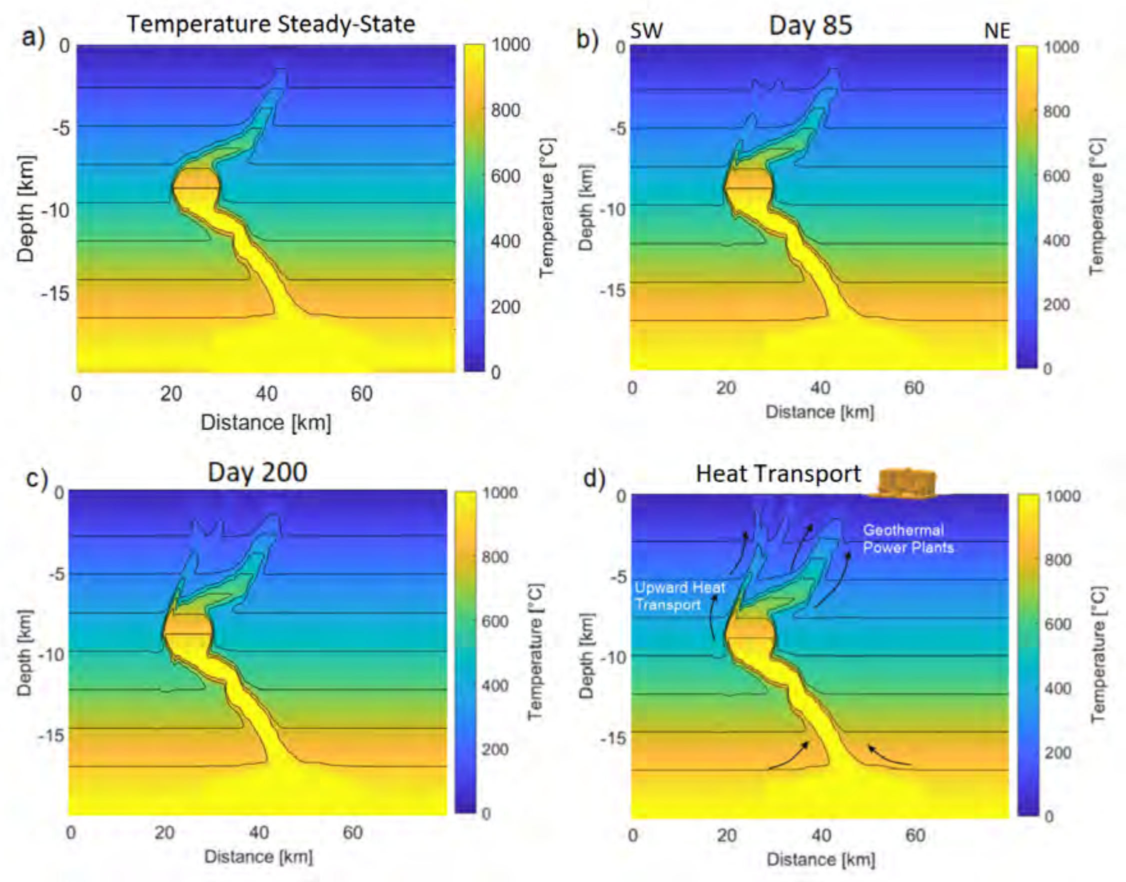

Figure 5.5: Advection-diffusion of temperature for different time steps. a) Steady-state temperature distribution. b-c) The heat migrate from the magma chamber to the faults and upwards within the conduit. d) Temperature distribution at day 365 and location of geothermal power plants illustrating the upward migration of the heat. The entire temperature evolution is attached as a video in the supplementary.

These results demonstrate that the active Aso volcano causes a step-like geothermal gradient and provides large amounts of heat for geothermal use. This model, which replicates thermo-hydro-mechanical processes, can be used to better understand, and potentially predict the temperature increase during an eruption and to determine whether it is detrimental or beneficial to energy exploitation. In addition, the analysis can also be used in deciding the location of future geothermal power plants.

5.6 Discussion

This work employed a coupled thermo-hydro-mechanical model to examine the pore pressure and temperature evolution in the year following the Kumamoto earthquake and dramatic aftershock sequence beginning April 15, 2016. The results suggest a conceptual model where the earthquake/aftershock sequences ruptured hydraulic

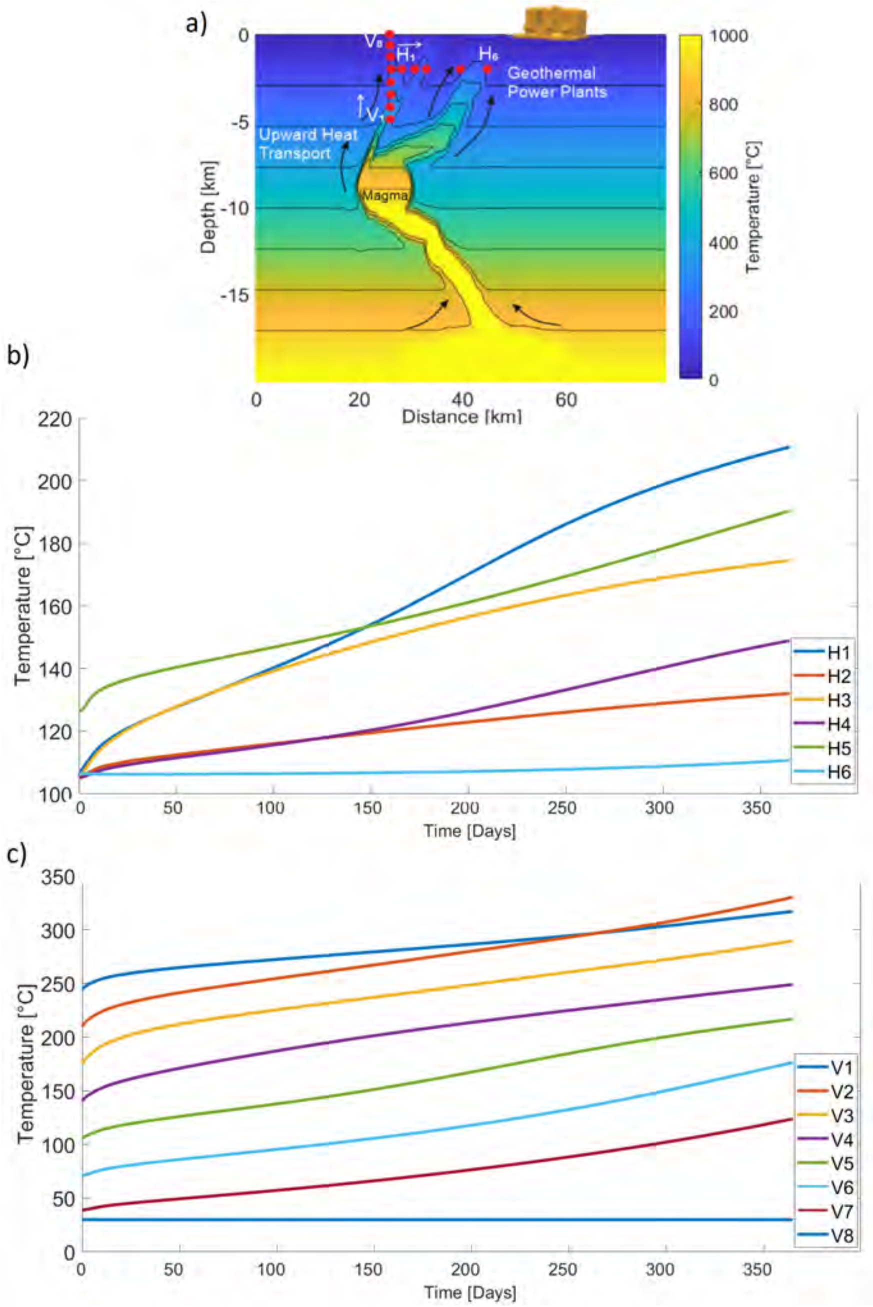

Figure 5.6: Temperature profiles. a) Temperature distribution at 365 simulation day. The red dots indicate the location of the vertical and horizontal profiles. b) Nine temperature distribution profiles show the temperature increase from top (V1) to bottom (V8). c) Horizontally aligned Temperature profiles (H1-H6) with a vast difference in temperature distribution.

seals and established hydraulic connections between the fault system and the magmatic chamber. This is in agreement with the the quantitatively examined work of [Nakagomi et al., 2021] that demonstrated pore fluid pressures controlling the aftershock generation. The subsequent migration of high pore pressures triggered aftershocks primarily within and around the fault system and instigated advective heat transport. The model reproduces the temporal and spatial aftershock behavior of the earthquake catalog and shows excellent agreement with the recorded data. To capture the temporal and spatial evolution of the 2016 Kumamato earthquake sequence, I adjusted α_j until a suitable fit was obtained for the entire data set, as α_j directly influences the occurrence of aftershocks in the model. Thus, the model accurately reproduced observations with the variation of a single parameter α with $1/\alpha = 100$ days, roughly corresponding to the inflexion point of the temporal aftershock occurrence (Fig. 5.4). Starting the simulation with the first mainshock on April 14th 2016, the 100 days of dehydration processes and permeability recovery correspond to late July 2016. From a geodynamic perspective, this might be related to the inflation of the volcanic magma detected at the surface around this time [Hendriyana and Tsuji, 2019]. This result suggests that the decrease in fluid pressure surrounding the chamber allowed the chamber to expand resulting in inflation detected at the surface. This is supported by the recorded and modeled aftershock rates, showing a significant reduction in the rate of aftershocks after approximately 100 days.

Heat transport is dominated by advection inside of the faults and volcanic structures, with comparably small temperature changes (via diffusion) in the vicinity of the fluid pathways. Determination of advective heat transport is usually challenging, as temperature measurements at greater depth are rarely available. Therefore, constraining the advective heat flow using the earthquake propagation allows the reduction of uncertainties with respect to heat transport by providing a solid estimate of the flow velocity. The simulation results suggest that the water temperature near the geothermal power plants was somewhat effected by the volcanic and seismic activity in 2016. However, the major earthquake destroyed power lines and the power plant had to be shut down for some time. The recent volcanic eruption in October 2021 possibly influence the geothermal energy potential. Interestingly, this eruption was unaccompanied by concomitant seismic activity, suggesting that the high fluid pressure needed to drive seismic sequences remained subdued. Additional studies are clearly warranted to investigate the October 2021 eruption and its influence on geothermal power production.

5.7 Conclusion

The April 2016 Kumamoto earthquake and subsequent aftershocks directly influenced volcanic activity at the Aso caldera. Observations and modeling suggest that the seismicity is directly related to pressure variations associated with the magmatic activity of the volcano. It can be speculated that the rupture of the mainshock initiated from the deep portion of a northwest-dipping fault plane along the Hinagu fault, which then triggered the Futagawa fault, propagated northeastward and upward, opening fluid pathways along the way. Entrained high pressure fluids likely drove the aftershock sequence, and the subsequent fluid pressure dissipation allowed expansion of the magmatic chamber and eventual eruption of the Aso volcano. The heat around the geothermal power plant increased to some degree, and suggests that the 2021 Aso eruptions are beneficial for geothermal energy potential and power generation.

Chapter 6

Adapting a physical epidemic-type aftershock model to simulate the spread of COVID19

6.1 Abstract

There exists a need for a simple, fast, deterministic, scalable, and accurate model that captures the dominant physics of pandemic propagation. Here we propose such a model by adapting a physical earthquake/aftershock model to the COVID19 problem. The aftershock model revealed the physical basis for the statistical Epidemic Type Aftershock Sequence (ETAS) model as a highly non-linear diffusion process, thus permitting a grafting of the underlying physical equations into a formulation for calculating infection pressure propagation in a pandemic-type model. The COVID19 pandemic propagates through an analogous porous media with the hydraulic properties approximating beach sand and water. Model results show good correlations with reported cumulative infections for all cases studied to date. In alphabetical order, these include Austria, Belgium, Brazil, France, Germany, Italy,New Zealand, Spain, Sweden, Switzerland, UK, and the USA. We also compare to Melbourne (AU) to demonstrate that the model scales. Importantly, the model is predominantly controlled by one parameter (α), which modulates the societal recovery from the spread of the virus. The obtained recovery times for the different pandemic waves vary considerably from country to country and are related to the temporal evolution of registered infections. These results provide an intuition-based approach to designing and implementing mitigation measures, with potential predictive capabilities for various mitigation scenarios.

Keywords:COVID19, Modelling pandemic, Earthquake aftershock model, Nonlinear diffusion

6.2 Introduction

The global COVID19 pandemic demonstrates that modelling the infection propagation is essential for managing and mitigating its spread and containment [Holmdahl and Buckee, 2020]. Models describing infections during pandemics can be roughly separated into three categories; (1) the widely-used SEIR (Susceptible-Exposed-Infected-Removed) model [Li and Muldowney, 1995, Carcione et al., 2020, Thompson et al., 2020], and many of its variations [Mwalili et al., 2020, Adiga et al., 2020]; (2) ABM models [Makarov et al., 2020, Batty et al., 2012, Gharakhanlou and Hooshangi, 2020, Gilbert and Bankes, 2002, Silva et al., 2020]; and (3) models based on reaction-diffusion processes [Nauman Ahmed, 2020, Fisher, 1937, Viguerie et al., 2020]. The SEIR model couples sets of ordinary differential equations constrained by numerous variables including the important (but difficult to constrain [Vespignani et al., 2020]) infection rate (R) to produce predictive outcomes. ABM models track up to 6.5 billion numerical people interacting with, and infecting, other numerical people based on (uncertain) rules of human-behaviour. Other approaches include concepts of Self-Organized Criticality (SOC) [Contoyiannis et al., 2020] or Monte-Carlo simulations [Xie, 2020]. Each of these modelling approaches contain multiple and sometimes intractable variables [Thompson et al., 2020, Vespignani et al., 2020], resulting in large uncertainties in outcomes, thus restricting their utility in guiding local, national, and international governmental decisions for managing and controlling pandemics.

Here we adapt a simple model [Miller, 2020] of non-linear fluid pressure diffusion through a porous media to the COVID19 problem. We propose a different perspective for viewing pandemic propagation, and presented a physical and numerical model that we consider simple because it contains fewer parameters. We view this simplicity as a benefit because uncertainty rapidly grows with parameter space. The model was originally developed to simulate aftershock sequences of earthquakes and showed superior fits to data than the well-known empirical Omori-Utsu Law of aftershocks. [Omori, 1894, Utsu, 1961]. The basic assumption of the Epidemic Type Aftershock Sequence (ETAS) model is that aftershocks can generate their own aftershock sequences [Ogata et al., 1993, Helmstetter and Sornette, 2003, Passarelli et al., 2015], which is consistent with the physical basis of the model presented here. We do not assume ETAS in our model, but ETAS-type behavior emerges from the underlying physics. Since pandemics are large-scale epidemics, a physical aftershock model can be viewed as an epidemic/pandemic model. Therefore, we have adapted our physical aftershock model to a Pandemic Type Aftershock Sequence (PTAS) model because infected humans can infect other humans.

Further the physical earthquake/aftershock model showed that aftershock decay rates are controlled by the tectonic ability to heal co-seismic and post-seismically generated permeability networks. In the pandemic analog, the decay of infection rates are determined by societal ability to suppress infection networks through mitigation measures. Hence, the physics are adapted and applied to epidemiological problems.

6.3 Physical Model

Diffusion of fluid pressure in a porous medium is governed by:

$$\frac{dP}{dt} = \frac{1}{\phi\beta} \bigtriangledown \cdot \left[\frac{k}{\eta} \bigtriangledown P \right] + \frac{Q}{\phi\beta} \tag{6.1}$$

where P is fluid pressure [Pa] above hydrostatic, t is time [s], ϕ is porosity [-], β is compressibility [Pa^{-1}], k is the permeability [m^2], η is fluid viscosity [Pa s], and Q is a source term [s^{-1}].

In the pandemic analogy, we apply an infection source rate (S_i), and calculate the time evolution of infection pressure (P_i) as it diffuses through societies. Thus, infection pressure is an abstract quantity that reflects the spread of the virus and can be written as:

$$\frac{dP_i}{dt} = \frac{1}{\phi\beta} \bigtriangledown \cdot \left[\frac{k_i}{\eta} \bigtriangledown P_i \right] + \frac{S_i}{\phi\beta} \tag{6.2}$$

where P_i is infection pressure [Pa], t is time [s], ϕ is a measure of the population distribution [-], β is compressibility [Pa^{-1}] interpreted as societal compliance, k_i is the infection permeability [m^2] reflecting the resistance to infection pressure gradients, η [Pa s] is the viscous term describing the ease of flow (e.g. internal friction), and S_i [s^{-1}] is the infection source rate. We purposely preserve, for clarity, the physical units of the porous media analogy.

The diffusivity κ reflects the rate of infection pressure propagation throughout each country:

$$\kappa = \frac{k_i}{\eta\phi\beta} \tag{6.3}$$

while permeability is further defined as:

$$k_i = k_0 e^{\pm\alpha_j t_j} \tag{6.4}$$

where k_0 [m^2] is the initial resistance to infection diffusion. A reduction in k_0 over a timescale α_j [s^{-1}] reflects the increased resistance to flow in response to mitigation measures. Note that diffusivity, which is composed of the dynamics of permeability, viscosity, compressibility and porosity, accounts for the reduction in usage of public transport, enforced shutdowns, mask requirements, and social distancing controlled by α_j over the timescale of t_j.
The source term S_i is defined in similar way:

$$S_i = Q_0 e^{\pm\zeta_j t_j} \tag{6.5}$$

where Q_0 [s^{-1}] is introduced throughout the domain. Initially the source term is concentrated at airports and major transportation hubs because that is where the virus entered. The source term takes a positive value when the virus enters the system, and a negative sign in response to mitigation measures. ζ_j [s^{-1}] as used in Equation 6.5 reflects the response of infection pressure sources based on mitigation measures.

We distinguish between α_j (Eq. 6.4) and ζ_j (Eq. 6.5) to allow for their exploration independently in future studies, but in this work we assume $\alpha_j = \zeta_j$ to limit the number of free parameters used to fit the data. Equation 6.2 is the mathematical formulation for calculating pressure propagation. When the pressure propagates through the model and reaches an arbitrary (but constant) critical state, which is defined by a threshold, numerical infections are triggered, accumulated, and counted. The growth and decay of infections is subsequently controlled by diffusivity, with pressure gradients diffusing along high diffusivity pathways (e.g. high-speed trains, high population density, etc.). We compare normalized cumulative numerical infections with the number of reported cases of each country. The cumulative number of infections in a country can be best modelled by considering the heterogeneity of the entire system. For example, the transport infrastructure and population density are included in the diffusivity, which controls the rate of infection pressure propagation. All parameters in all simulations were defined a priori and remained unchanged throughout the simulation, with the exception of α_j. We intentionally limited our parameter choices to maintain our analogy with the porous media counterpart, which limits permeability, viscosity, and compressibility to limited ranges. The terms α_j

were our fitting parameters, and the values constrained by the data for each observed infection wave. α_j in Equations 6.4 and 6.5 modulates the system compliance $\phi\beta$ in both the diffusion and source terms, and dominates the model behavior. The concavity observed in the data constrains the sign of α_j. Conceptually we might decompose β into political compliance β_p and economic compliance β_e because a country's economic health might also affect a country's response. Such a decomposition is analogous to a separation between fluid compressibility and pore space compressibility in the earthquake model. In this work, β is unconstrained, so we assume a lumped compressibility with a constant value of ($\beta = 10^{-8}$ Pa^{-1}) for all countries. We use the porosity in the model as a measure of population density. We define porosity as $\phi = 0.5 - \left(\frac{f_s}{f_c}\right)$, where f_s is the population of a state and f_c is the population of the entire country. The 0.5 term is constrained by demographics and limits the range of ϕ to reasonable values of the model's geological analog ($0.2 < \phi < 0.49$). For each simulation, we defined parameters ϕ, k, η, and S, for each state within that country. Parameter space was extensively investigated, and we arrived at the parameters that best matched the data. The initial permeability k_0 takes on values of either 10^{-12}m^2 or 10^{-13}m^2, with the former applied to high population density and their corresponding transportation networks, and the latter for sparsely populated regions. The viscous term (η) takes on values of 10^{-3} or 10^{-2} Pa s^{-1} with the lower value reflecting the degree of public transport use. As an example, more than 20% of the populations of New York and California used public transport regularly prior to the pandemic and are thus assigned $\eta = 10^{-3}$ Pa s^{-1}. Conversely, the populations of Utah and Oklahoma rarely used public transportation prior to the pandemic and are thus assigned an order of magnitude higher viscosity using $\eta = 10^{-2}$ Pa s^{-1}. In addition, New York and California also had a higher influx of visitors prior to the pandemic, so we assume a higher initial permeability $k_0 = 10^{-12}$ m^2 compared to $k_0 = 10^{-13}$ m^2 for Utah and Oklahoma. Finally, Q is 10^{-8} s^{-1} at points of entry and 10^{-9} s^{-1} throughout the remainder of the domain and is mostly the same on average for all studies cases (Supplementary Figure 3). These values of all parameters were chosen to mirror (to some degree) their geological analog, and interestingly, the initial values best-suited for this model of infection pressure propagation have the hydraulic properties of water and beach sand as their porous media counterpart. Supplemental Table 1 lists the source of our input for population demographics and the viscous term η, which we equate to the use of public transportation and the probability of human interaction.

Figure 6.1 shows the cumulative number of reported cases normalized by the

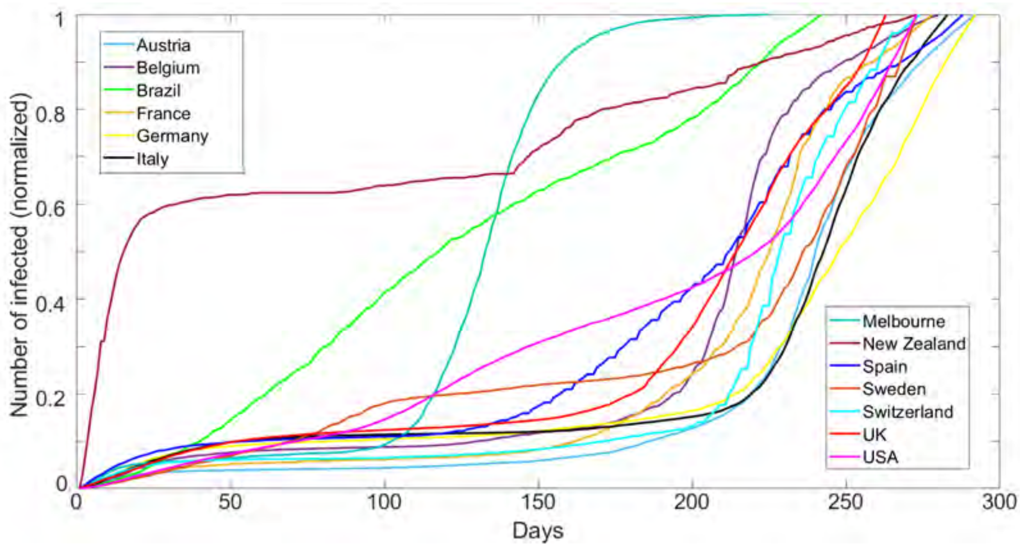

Figure 6.1: Compilation of reported cumulative infections for all cases studied and identified in the legend. The time range was March 15, 2020 to January 4, 2021 for all countries (Source: ECDC and Australian Government).

maximum reported cases for each data set over 300 days (March 15, 2020 to Jan. 4, 2021) for Austria, Belgium, Brazil, France, Germany, Italy, Melbourne (AU), New Zealand, Spain, Sweden, Switzerland, UK, and the USA. The data is published by the European Centre for Disease Prevention and Control (ECDC) [ECDC,], which monitors the COVID19 pandemic. The Melbourne data was obtained from the Australian government of health and human services [DHHS,]. The data shows a very broad range of behavior, which we show below to be modelled only by varying α.

6.4 Results

From this input, the initial conditions at the start of each simulation (Figure 6.2 a) are heterogeneous and approximate at a large scale the overall societal setup. We use a timestep of one day, which results in a total simulation time of about 2 minutes on a typical laptop running a MATLAB script. (We also tested timesteps of 430 seconds, with no change in results). Our comparisons with data extend to 300 days, which covers the onset of the pandemic in each country until both virus mutations and the introduction of vaccines modify the data sets in yet unknown ways.

Figures 6.2b-c show typical model results for four different countries (see Supplemental Figures 1 and 2 for the remaining cases). The calculated infection pressure concentrates in large urban areas (Figure 6.2 b), reflecting high population density and ease of flow (e.g. viscosity) but also shows pervasive elevated pressures throughout each country. This figure visualises the dramatic differences in infection pressure (and thus modelled infections) for the different countries. Unsurprisingly, the calculated number of cumulative infections also correlates with population concentration and ease of flow (Figure 6.2 c).

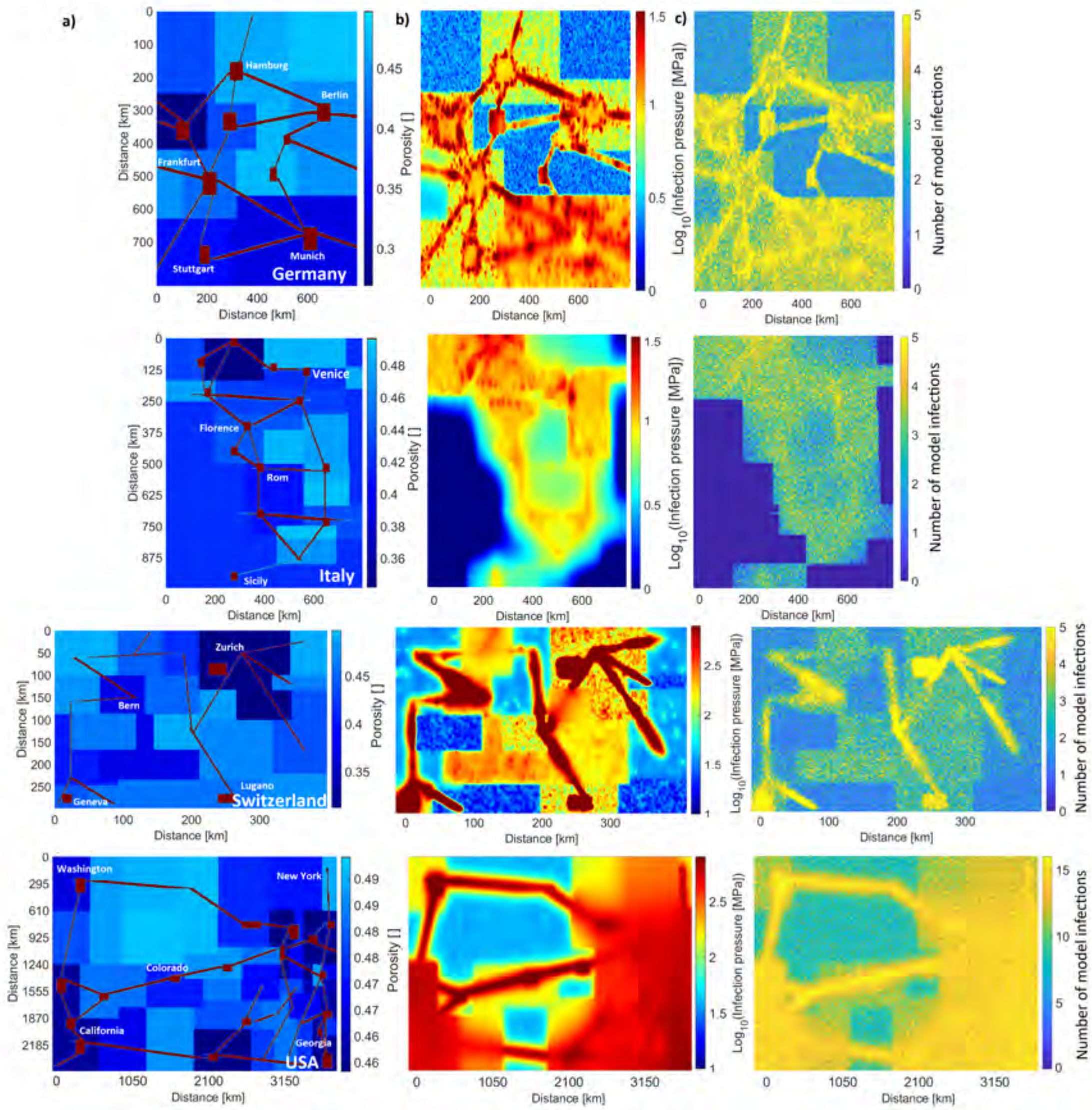

Figure 6.2: a) Model setup for Germany, Italy, Switzerland and the USA showing the source locations (red) signifying airports and intercity rail lines, and the various shades of blue scale with population density reflecting the "porosity" distribution and delineate federal states. b) Calculated infection pressure at the end of the 300 day simulation. Note change in scale bar for each country because of the very large variations in infection pressure. c) The number of repeated infections calculated in the model highlights the regions most affected and shows how elevated infection pressures (Figure 2b) continue to generate model infections. Similar plots for all other cases studied are found in Supplementary Information.

Figure 6.3 shows the observed cumulative infections (i.e. Figure 6.1) superposed with modelled cumulative infections for all countries studied. Good agreement between model and observations is found for all countries, and model scaling is demonstrated by comparing results with observations at the local scale of Melbourne, Australia. We chose Melbourne, Australia, because they underwent two severe lock downs. The model successfully matches cumulative infection observations for large countries, small countries, and states. This agreement is observed despite the vast differences in governmental and societal response, and importantly, good agreement is achieved by modifying the parameter α, with different values for α chosen to fit the dynamics of COVID19 propagation (Figure 6.3 a). The parameter α dominates the model behavior because it modulates the system compliance $\phi\beta$ that appears in both the diffusion and source terms in Equation (6.2).

Figure 6.4 shows time histories of calculated infection pressure P_i and diffusivity κ, for all cases studied. The diffusivity reflects the rate of infection pressure propagation throughout each country (6.3. For intuitive reference the diffusivity of water and beach sand is roughly 15 [m^2 s^{-1}], so from a physics perspective, the virus propagates very quickly. The initial rapid drops in diffusivity reflect pro-active societal response to government measures in all presented countries. Reduced diffusivity consequently results in rising infection pressure and pressure gradients, which remain in the system, to then subsequently diffuse upon relaxation of mitigation measures. Looking at an exemplary EU state (e.g. Austria), the diffusivity initially decreases to a value of approximately 2 [m^2 s^{-1}] in response to mitigation efforts. Meanwhile, pressure increases over this timescale constrained by ζ (where $\zeta = \alpha$ in this study) in Equation (6.5), and which subsequently diffuses, resulting in a mild pressure decrease. A sudden rise in κ correlates with imposition of α_2, and thus the consequent pressure drop, followed by a mild apparent reduction in κ. Imposition of α_3 correlates with mitigation efforts that again reduce κ and increase P_i. This results in the onset of the 2^{nd} wave, which we model by imposing $-\alpha_2$ that dramatically increases diffusivity and the consequent reduction in P_i. Finally, α_3 reflects additional mitigation measures, and subsequent waves can be modelled with additional values for α.

Figure 6.5 quantifies the values for α, plotted for intuitive convenience as $1/\alpha$ [days], used in the simulations to fit the data (e.g. Figure 6.3). We note a few important points. First, Brazil Sweden and USA reveal the longest recovery times $1/\alpha_1$, indicating that people are longer exposed to the virus. The modeling results show that Italy, Spain and the United Kingdom have longer recovery times (slightly

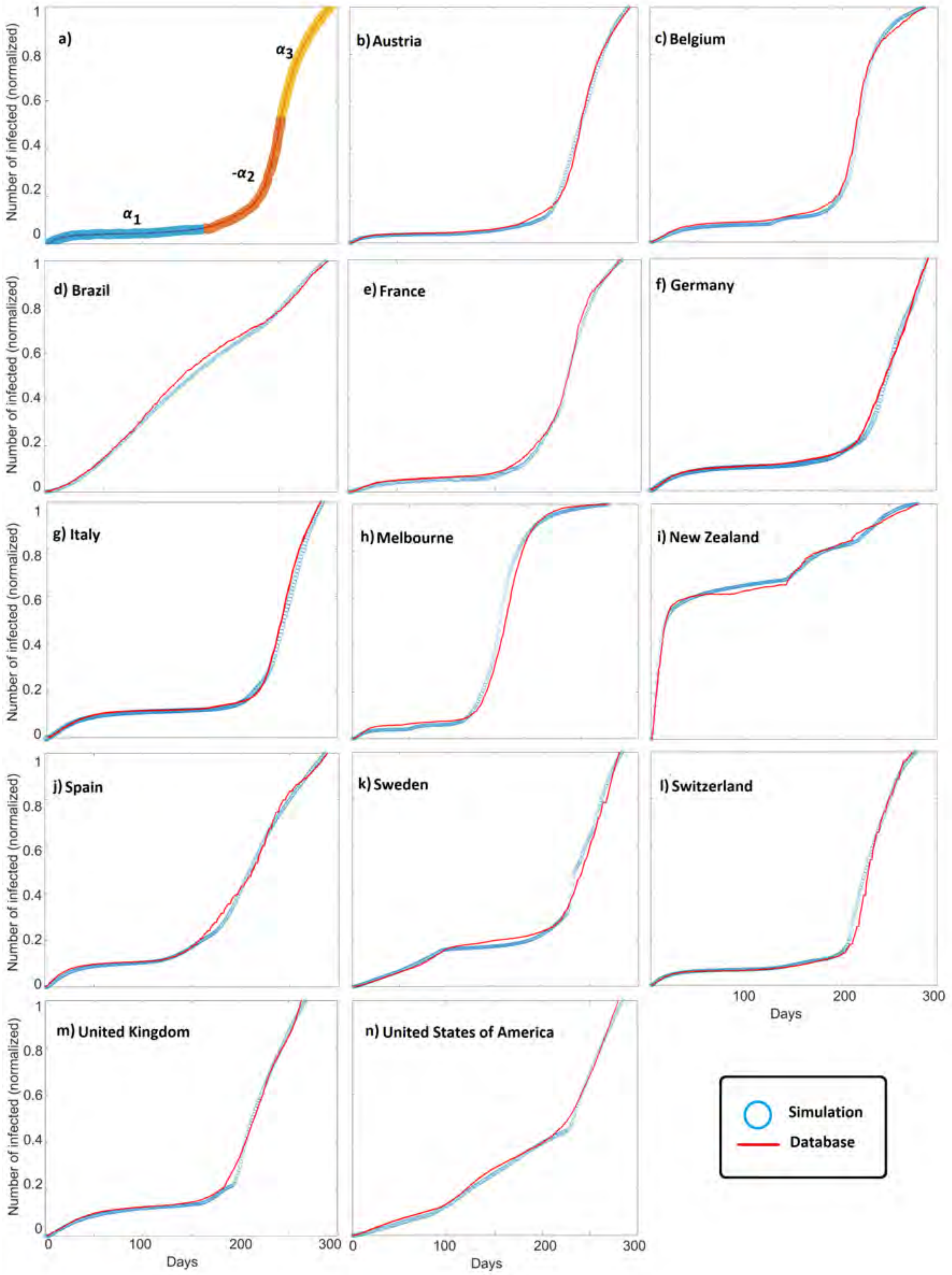

Figure 6.3: Comparison of all data in Figure 6.1 superposed with the corresponding model results. The data constrains $\pm\alpha = \pm\zeta$ and how this is achieved is demonstrated in Figure 3a. Excellent agreement in all cases is observed.

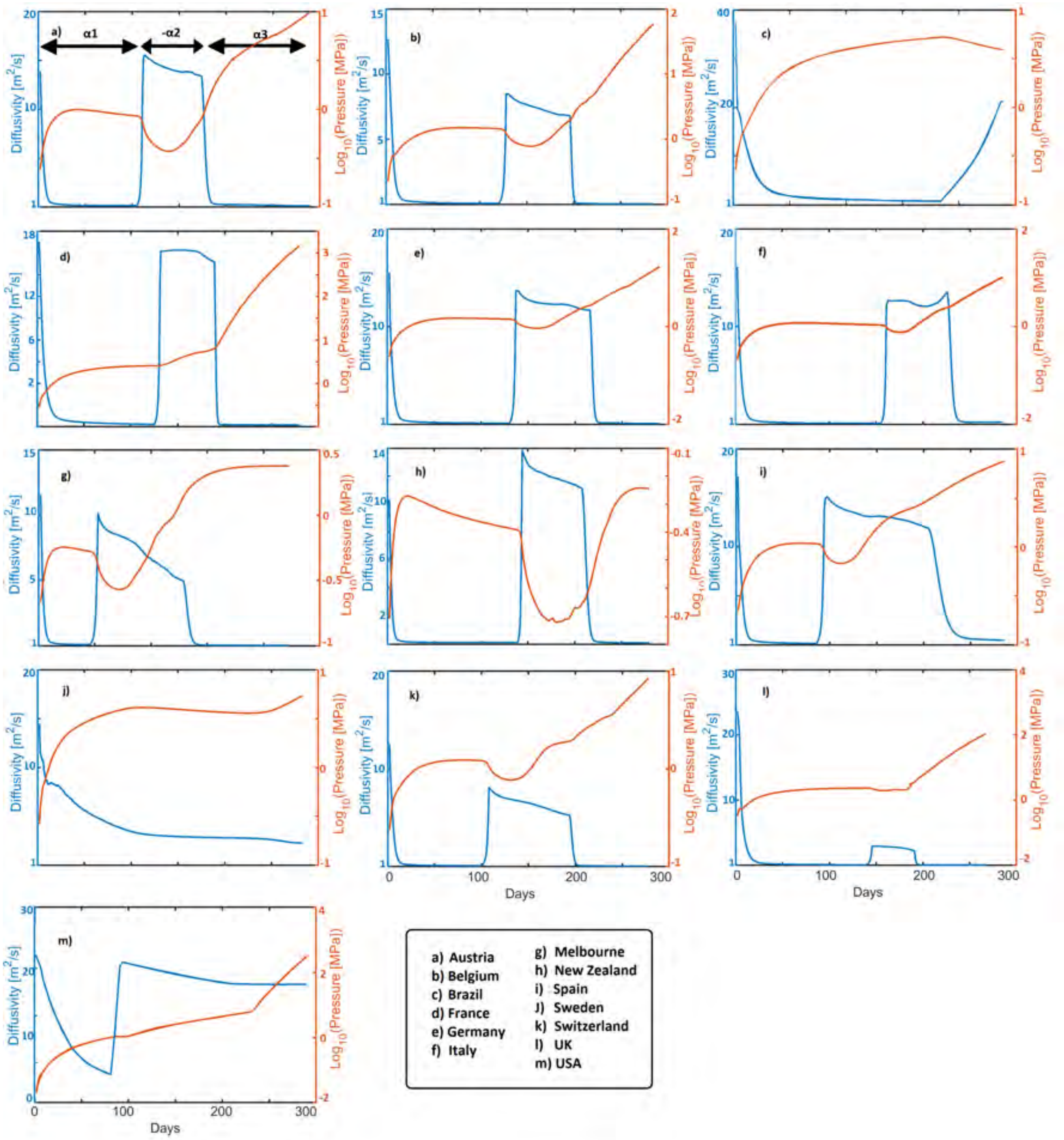

Figure 6.4: Modelled diffusivity and pressure time histories for each individual country (and Melbourne) showing the hydro-dynamical response to mitigation measures. For reference, the hydrogeological properties of beach sand and water is roughly $15 m^2 s^{-1}$.

more than one month) than the other EU countries (and Switzerland), where recovery times are approximately less than two weeks. The fastest recovery times were observed for Austria, New Zealand and Melbourne. The acceleration in infections at the onset of the 2^{nd} wave is quantified by $-1/\alpha_2$, and shows rapid acceleration in Belgium, USA, Spain, Switzerland, and the UK. This acceleration during the second wave is explained in the model as the onset of diffusion (instigated by relaxation of mitigation measures) of latent infection pressure gradients stored in the system. Finally, α_3 reflects the ongoing situation, and may change depending on governmental measures and societal response. Note that the concavity for New Zealand at the onset of the second wave (Figure 3i) required $+\alpha_2$, and that Sweden and Brazil had essentially no recovery from the first wave, so α_2 and α_3 are essentially zero.

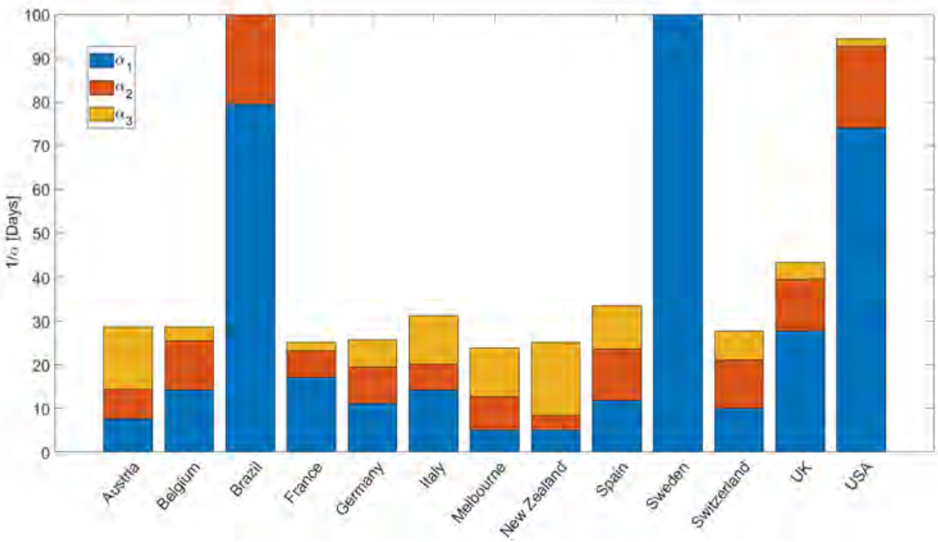

Figure 6.5: Summary of α values used in the simulations, showing a wide range of recovery times for different countries. α_1 (blue) represents the recovery time of the first wave, α_2 (orange) represents the second wave, and α_3 (yellow) represents the recovery of the on-going third wave

.

6.5 Discussion and Conclusions

We presented a simple model for the propagation of infection pressure through societies and compared model results with global COVID19 data. We find good agreement for all cases studied, and importantly, fits to the data are achieved by varying parameter α, where α quantifies the response to mitigation efforts. The purpose of this work is to present a new formulation of infection propagation using a deterministic model, and which matches a very wide range of data using only a few (and intuitive) parameters.

The result that only slight variations in model parameters can reproduce all observations of infection rates across the globe strongly indicates that this model captures the essence of the physics of pandemics. This physical deterministic model reproduces the cumulative number of COVID19 cases in a dozen countries including an island (New Zealand), and a confined city (Melbourne, AU). Importantly, this model scales. We have shown it to be successful in matching data for large countries, small countries, and countries with wide ranging social-political-economic conditions. The influence of vaccines and mutations can be addressed in future modeling, which our findings suggest may be further advanced by invasion percolation approaches. Finally, the model suggests that future strategies should be explored for reducing the latent infection pressure remaining in societies after successful mitigation measures. Once the model has been calibrated against observations (at any time), parameters can be varied to predict alternative outcomes.

For a general understanding of our findings, imagine the following: You are sitting on the beach with a hollow steel pipe, sealed at the bottom but with holes along part of its length. The part of the pipe with holes is driven into the sand. Water is then poured into the hollow pipe. The fluid quickly diffuses into the sand (infection propagation), and at rates that depend on the height of the water column in the steel pipe. At some distance from the pipe, a metal barrier surrounding the pipe is inserted into the sand (e.g. masks, lockdown, etc.), and the fluid (infection) propagation is curtailed. However, the pressure to drive the system is still in the pipe, so when lock-downs or mask restrictions are eased, fluid pressure (infection) quickly propagates (2nd wave), until mitigation measures are re-applied. Now further imagine a number of pipes inserted in the sand (e.g. airports) scattered across regions. Each system acts independently, but interacts dynamically with all other pipes inserted into the system. In our model, the initial pipes are the airports and α controls the barriers. With this conceptual understanding, one goal would then to be establish strategies that bleed off the pressure in the pipe (infection pressure in our model) during the lock-down/mask phases, so that when the restrictions are eased, there is much less fluid (infection) pressure in the pipe to drive the subsequent wave or waves.

6.6 Methods

The numerical model used in this study is the same as described in reference[Miller, 2020], but now includes a source term. It is useful to describe in detail the model setup for Switzerland as one particular case, which is then applied to all other simulations. The Swiss Confederation consists of 26 member states, and each state is implemented with its geographical boundaries. The often-used transportation network primarily links the major cities of Geneva, Lausanne, Basel, Zurich, and

Lugano, and is modelled as a highly permeable, low viscosity channel within the model. Additionally, significant airport hubs as point of entry, ranked by passengers per year, are included as groups of nodal points with high infection source rates. These statistics (for 2020) are provided by the Swiss federal office, which also provides population density and percentage of public transport use per federal state. At time zero, infection sources at points of entry develop infection pressure that then diffuses over time along infection pressure gradients and through highly permeable channels, triggering model infections along the way. The model setup of the eleven other countries and Melbourne are defined using this same procedure. This initialization of model geometry establishes domains of population density, transportation networks, etc. that controls the initial spread of the virus, and we assign the corresponding parameters (ϕ, β, k, η and S). The design of each model is based on the infrastructure, considering all states as a subunit of each country. Infections can propagate throughout the model, and the no flow boundary conditions are at boundaries of the entire model (e.g. border closures). We numerically solve Equation 6.2 using implicit finite differences on a regular grid of 300x300 nodal points, and calculate infection pressure diffusion in the numerical domain associated with each country. In the aftershock model [Miller, 2020], the triggering threshold is defined by the Mohr-Coulomb failure condition, but no such similar constraint exists on infection triggering. Therefore, we arbitrarily set the threshold to 1 MPa for all simulations. When the threshold is reached, time (t_i) in Equations 6.4 and 6.5 initiates at that numerical grid point, which influences subsequent solution of Equation 6.2. To allow multiple infections at the same nodal point, we double the threshold necessary to trigger each subsequent infection. Heterogeneity is inherent in the model through the characteristics of each country.

Chapter 7

Conclusion

In this thesis, I explored the working hypothesis that the dynamic hydrogeological properties dominate earthquake and aftershock sequences at depth in the vicinity of large earthquakes. In earthquake physics, in addition to deeply derived CO_2, thermal decomposition can generate significant quantities of high-pressure fluid, that then must diffuse through an evolving permeability network. A non-linear diffusion equation with a source term solves the fluid pressure field as a function of time and is then compared to the 2016 Amatrice-Visso-Norcia sequence of 35,000 aftershocks. The dominant parameter ($\alpha = \zeta$) controls the timescale for permeability recovery and the timescale for fluid input from either a deep source of CO_2 and/or a direct fluid source from thermal decomposition of the ubiquitous carbonates of the Apennines. The results reveal hydraulically isolated deep reservoirs in the central Apennines (Chapter 3). Specifically, the aftershock behavior in the northern study area is substantially more robust than in the south due to both (i) a more vigorous high-pressure reservoir at depth and (ii) significantly more CO_2 produced from co-seismic thermal decomposition. Interestingly, the Mt. Sibillini thrust fault (MST) transects the aftershock sequence and acts as a barrier separating two isolated high-pressure CO_2 sources at depth. This model result emerges even though the MST is not explicitly modelled. The results show excellent spatial and temporal correlation of 35,000 well-located aftershocks from the 2016 Amatrice-Visso-Norcia sequence, and provide strong evidence that this sequence is predominantly, in not entirely, driven by high-pressure CO_2. Model results also suggest that aftershock sequences that differ from the standard Omori-type decay rate (e.g., the 2011 Tohoku earthquake, Japan, and the 2014 Iquique earthquake, Chile), implicate internal generation of fluids from either dehydration or decarbonization. I developed a 3-dimensional model of high-pressure fluid propagation to further investigate the central Apennines (Chapter 4). I consider the 2009 L'Aquila (M_w6.3) and the 2016 Amatrice-Visso-Norcia (M_w6.5) earthquake sequences that overlap in this study area. However, upon closer inspection, I identified that the AVN sequence filled a seismic gap between the 2009 L'Aquila sequence and the 2016 AVN sequence. Using a non-linear diffusion equation with a source term to mimic the generation of additional fluid by thermal decomposition, I show good correlations in space by comparing the calculated fluid pressure field and the locations of over 50,000 well-constrained hypocenters. The results also show that different fluid production rates activated different fault systems during both sequences causing seismic gaps. In addition, the temporal development of the observed cumulative number of aftershocks and numerically triggered events show a good agreement. The α parameter controlling the permeability network and internal source generation suggests that AVN North is highly affected by a vigorous high-pressure reservoir and is by far not comparable with the reservoir state towards the southern central Apennines. I then extended the model to an advection-diffusion thermal model (Chapter 5) to investigate hydraulic behaviors and study the dynamics between earthquakes, volcanic eruptions, and geothermal enengy potential in Japan. The results showed how geothermal power plants were affected by the eruption of the nearby Aso volcano. The seismic activity opened pre-existing vertical cracks providing pathways for the ascending high-temperature magma, which is beneficial for geothermal production. The April 2016 Kumamoto aftershock sequence, with three major earthquakes, directly affected volcanic activity of Mt. Aso. Results show that temperature would have slightly increased observation of spatial and temporal correlation of the increased on the southwestern side of the caldera in response to the aftershock sequence. Unfortunately, this could not be verified because the plants were destroyed an shut down due the M7.3 mainshock. This thermo-hydro-mechanical model can be applied to any volcanic-seismic activity system to quantify and possibly forecast eruption duration and determine if the seismic activity is detrimental or advantageous for energy exploitation.

I also capitalized on the observation that the acronym (ETAS) for statistical models used to study aftershocks sequences means Epidemic Type Aftershock Sequences. The equations governing non-linear diffusion with a source term were reformulated to capture infection pressure propagation through a porous and healing society (Pandemic Type Aftershock model), and reported in Chapter 6. The numerical model reproduces the spatial distribution of the virus (COVID19) in a society and the cumulative number of infections for one year after the first recorded infection. This quantitative and deterministic model matches the cumulative number of COVID19 cases for 12 countries (studied to date) and the city of Melbourne, Australia. It provides an intuitive and quantifiable understanding of the COVID19 pandemic and possible future pandemics. The source term in this study was essential to consider internal infection with the virus from person to person and the introduction of the virus to country occurring at airports and major transportation hubs. These exciting results demonstrate that non-linear diffusion in a porous media coupled with source terms can adequately model two seemingly disparate systems.

7.1 Future perspective

The results of this thesis are potentially ground-breaking, and thus opens up numerous avenues for future advances in laboratory studies, numerical experiments, and geophysical and geological measurement and observations. The internal generation of fluids by dehydration or decarbonization not only results in a massive release of fluids throughout the region [Bessat et al., 2021, John et al., 2009] but also escapes as CO_2 at the Earth's surface. One of a few future objectives is to develop, install, and monitor geochemical stations around seismogenic areas to retrieve continuous flux measurements and isotopic determination of the CO_2 emitted by soils and transported by aquifers. Furthermore, laboratory experiments of fluid mass generation as a function of slip, slip velocity, and confining stress, would quantify the amount of CO_2 produced by decarbonization at earthquake-relevant slip velocities. The laboratory results can then constrain the source term included in the model to simulate both spatially and temporally aftershock sequences. In addition, laboratory experiments can include the devolatilization of carbonate samples obtained in the field to measure pore fluid pressure development during shear heating. High slip-speed experiments on serpentinites and other hydrous minerals obtained in the field can constrain volatile production earthquake relevant slip rates. I recently discovered that the hypocentral distribution of earthquake events in subduction zones (including the brittle and ductile environment) shows upward and downward migration of seismic events. Given the importance of fluids in earthquake sequences, a future goal would be to understand the effects of high-pressure fluids on megathrust earthquakes in subduction zones that exhibit dynamic processes. The near-surface earthquakes can be explained with a brittle mechanical formulation where shear stress is directly proportional to shear strain. In contrast, the deeper earthquakes require a ductile formulation to understand the apparent viscosity at higher stress rates. The instability of thermal runaway requires high stresses and can be resolved by considering metamorphic reactions (e.g., serpentinization) that create orders-of-magnitude reductions in the effective viscosity. The coherence of these two earthquake localization mechanisms may be the presence of overpressure pulses propagating in fluid channels connecting the deep plate to the shallow seismogenic zone. Therefore, a future objective would be to explore the fluid migration in poroelastic and poro-viscous media, and quantify the dehydration process while considering the chemical reactions based on thermodynamic equilibrium calculations. These investigations will explore the consequences and implications of high-pressure fluids on the earthquake cycle. A unified model for fluid-driven earthquake cycles that captures the dynamic distribution of earthquake aftershocks in a subduction zone from shallow to deep depths is essential to the scientific society. A successful outcome of these studies would set the stage for possibly major advances in our understanding of earthquake physics and the earthquake process, and may open up an entirely new methodology for understanding fluid dynamics in the Earth's interior, with significant implications for seismic hazard assessment and mitigation.

APPENDICES

A Appendix for 'Spatio-temporal complexity of aftershocks in the Apennines controlled by permeability dynamics and decarbonization'

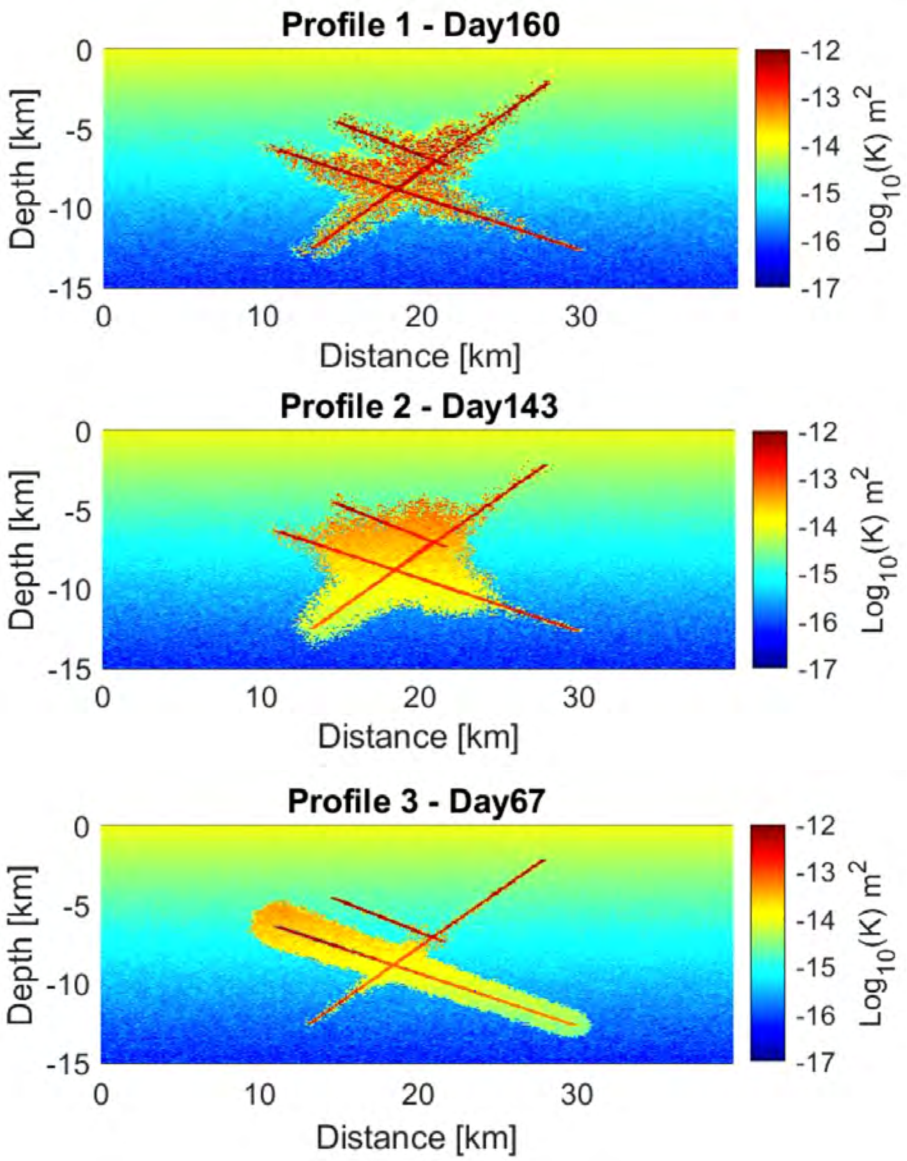

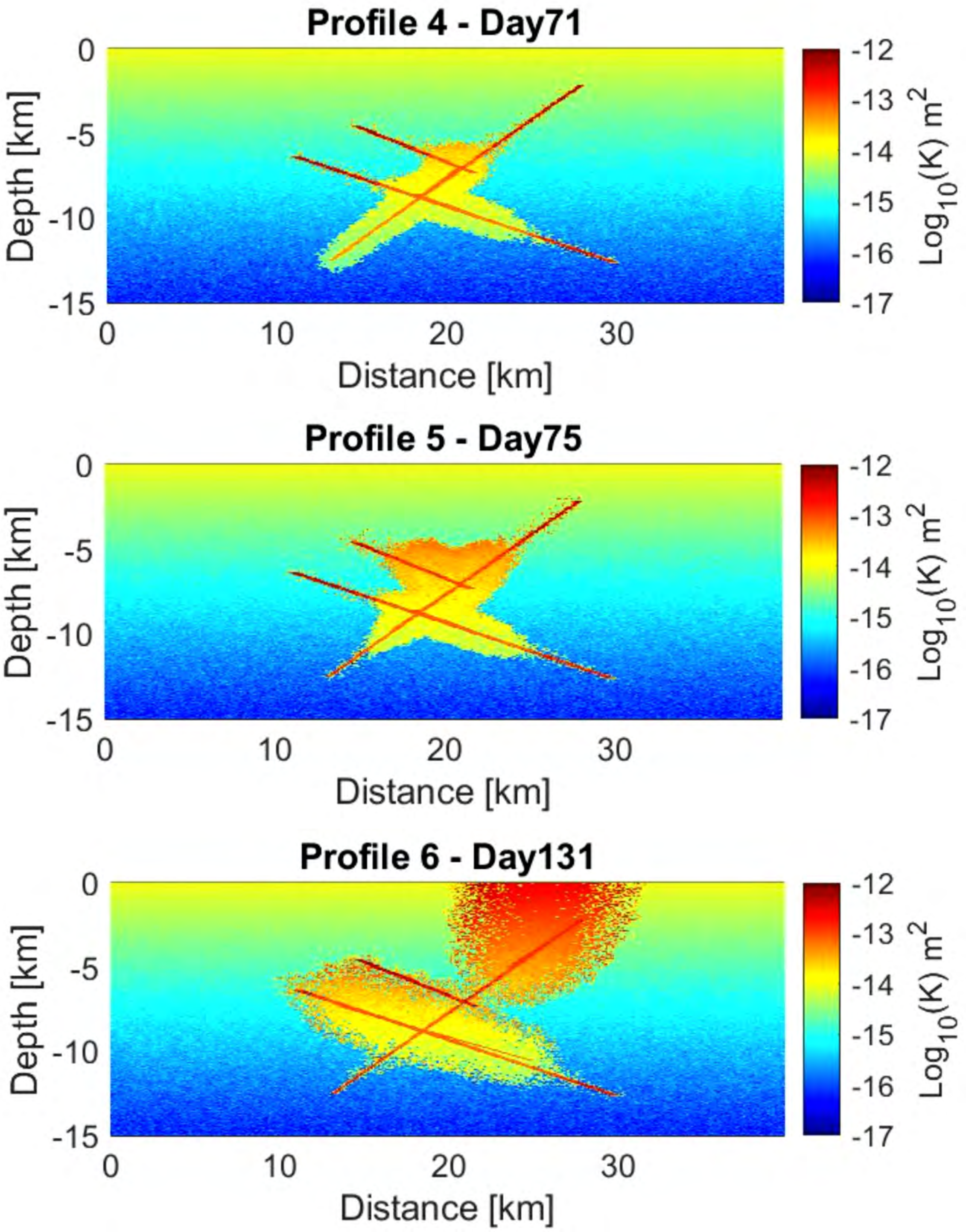
Profile 4 - Day71
Depth [km]
Distance [km]
$Log_{10}(K)$ m^2
Profile 5 - Day75
Depth [km]
Distance [km]
$Log_{10}(K)$ m^2
Profile 6 - Day131
Depth [km]
Distance [km]
$Log_{10}(K)$ m^2

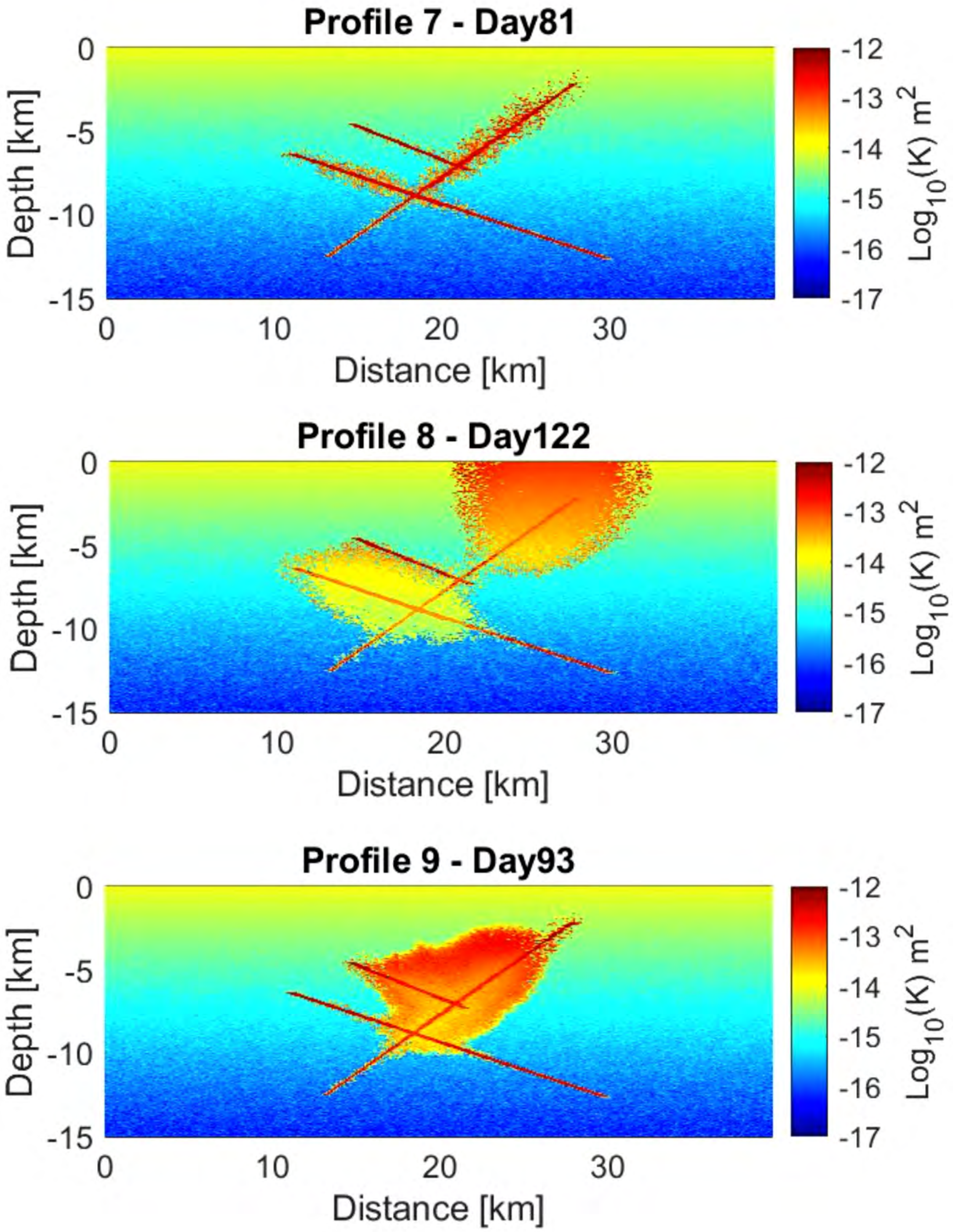

Figure A.1: Panels showing snapshots of the modelled permeability field at various timesteps for each profile modelled. Visualization of the entire permeability evolution are available.

B Appendix for 'Dynamics between earthquakes, volcanic eruptions, and geothermal energy exploitation in Japan'

Phreatic eruptions are vaporized fluid that occur when high-temperature volcanic fluids (gases or magma) contact shallow groundwater in a closed system under low-permeability rock [Stix and de Moor, 2018]. These vaporized fluids fill cracks, which in turn increases the formation pressure. This physical process leads to disturbances in hydrothermal systems and intense seismic activity [Zhao et al., 2018]. From January 2014 until February 2014 small phreatomagmatic eruptions were observed. From November 2014 to September 2015, the Aso caldera experienced strong eruptions with intermittent ash emissions, strombolian explosions, and phreatomagmatic explosions [Hendriyana and Tsuji, 2019, Minami et al., 2018]. Following this event, a series of major explosions with pyroclastic flows and ejections affected the immediate vicinity of the crater from August to October 23, 2015. From February 2016 to April 2016, a new eruption with emission of lapilli and ash fall was recorded at Nakadake vulconp around the same time as the Kumamoto earthquake. Thereafter, continuous volcanic activity was recorded until October 8th, when the large explosion occurred. Large volcanic bombs dispersed around the crater. After these events, there were no significant eruptions in 2017 and 2018.

Figure B.1 shows a time history of volcanic activity and seismic events from 2013 to 2019. This phenomenological comparison supports the well-known statement that volcanoes are responding to earthquakes and that they are always in interplay with each other. This volcano is known for pyroclastic eruptions, including ash emissions, strombolian eruptions, and phreatomagmatic activity [Ono et al., 1995, Lin, 2017]. The January and February 2014 preatomagmatic eruptions are accompanied by a number of earthquakes, with decreasing frequency in both number and magnitude of earthquakes observed. This might be explained by a pressure release through the eruptions. Similarly, in August to October 2015 larger volcanic explosions are associated with increased magnitudes and an increased frequency of earthquakes indicating the presence of high pressure fluids in the system. The highest magnitudes and the largest numbers of earthquakes are observed during February to April 2016

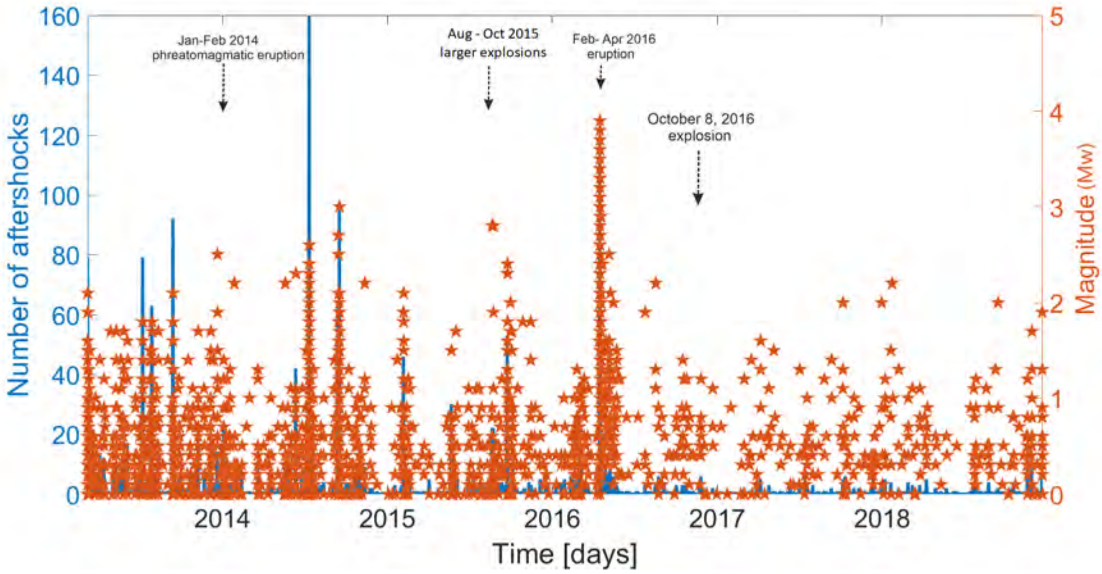

Figure B.1: Volcanic activity and seismicity. Earthquakes in the vicinity of the Aso caldera from 2013 to 2019 with their magnitude (Mw) compared to the volcanic activity of Mount Aso.

Symbol	Quantity	Value	Unit
c_s	Pore compressibility	$1e^{-10}$	1/Pa
c_p	Rock heat capacity	1.02	J/k/°C
λ	Thermal conductivity	0.6	W/m/°C
ρ_r	Rock density	2700	kg/m^3
ρ_f	Fluid density	900	kg/m^3
μ	friction coefficient	0.8	-

Table B.1: Fluid and rock parameters used in the numerical model.

which coincide with volcanic eruptions. The seismic activity decreases remarkably after the large volcanic explosion on October 8, 2016, possibly due to the pressure release in the volcanic system. There are increases in seismic activity in June to August 2014, which are not related to volcanic activity at the surface. However, those can possibly be explained with subsurface dynamics of the volcano and fluid pressure increases in structures not connected to the surface. There are continuous observations at the surface measuring increased degassing of CO_2 and SO_2 during the whole period [Morita et al., 2019].

C Appendix For 'Adapting a physical epidemic-type aftershock model to simulate the spread of COVID19'

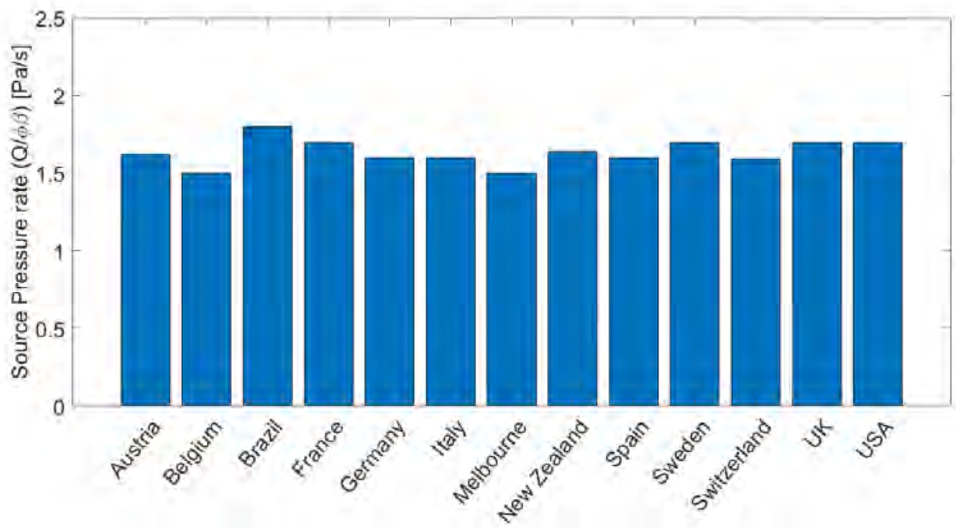

Figure C.1: Average initial source pressure rate for each studied case.

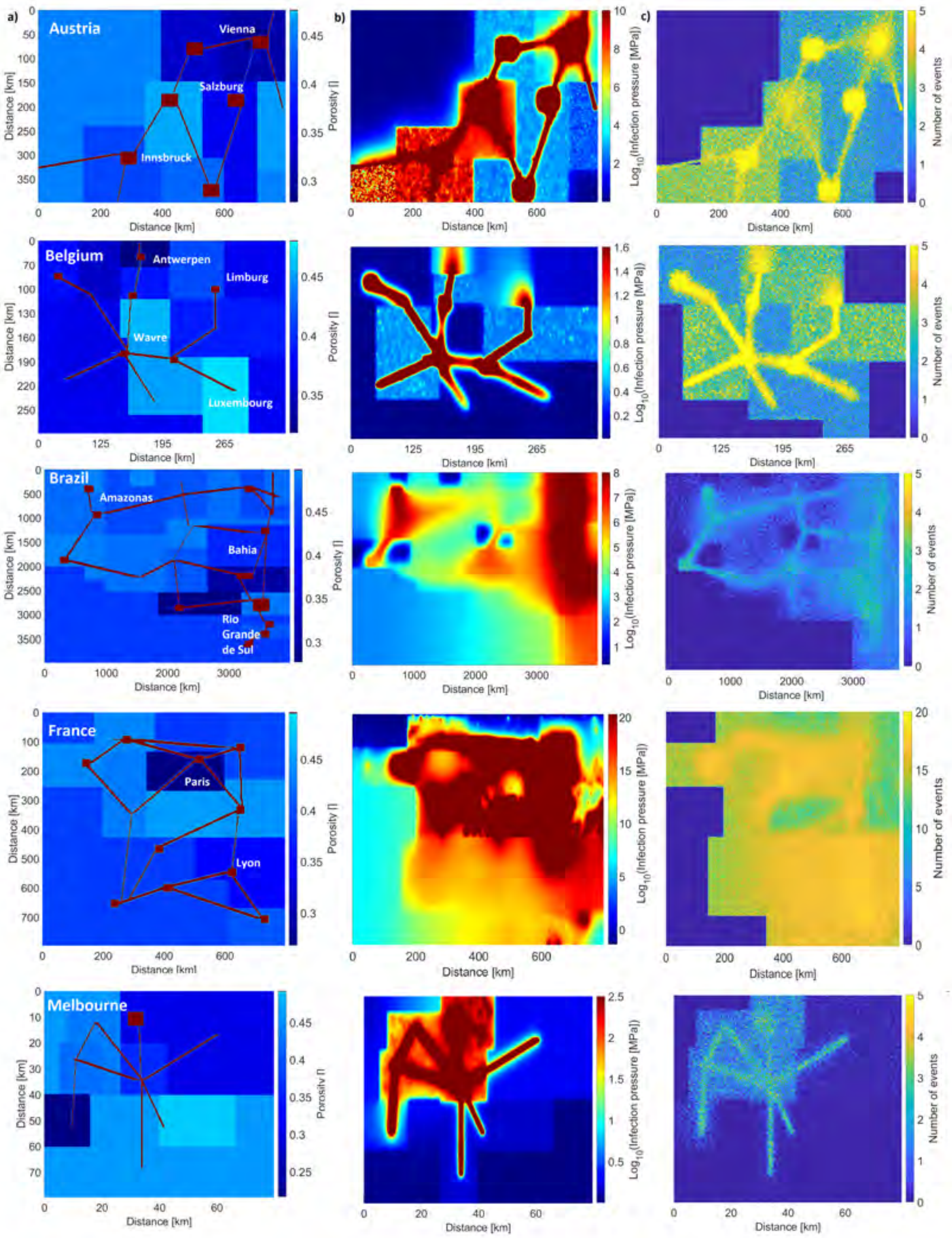

Figure C.2: a) Model setup for Austria, Belgium, Brazil, France and Melbourne showing the source locations (red) signifying airports and intercity rail lines, and the various shades of blue scale with population density and delineate federal states. b) Calculated infection pressure at the end of the simulation. Note change in scale bar for each country. c) The number of repeated infections calculated in the model highlights the most affected regions and shows how elevated infection pressures b) continue to generate model infections.

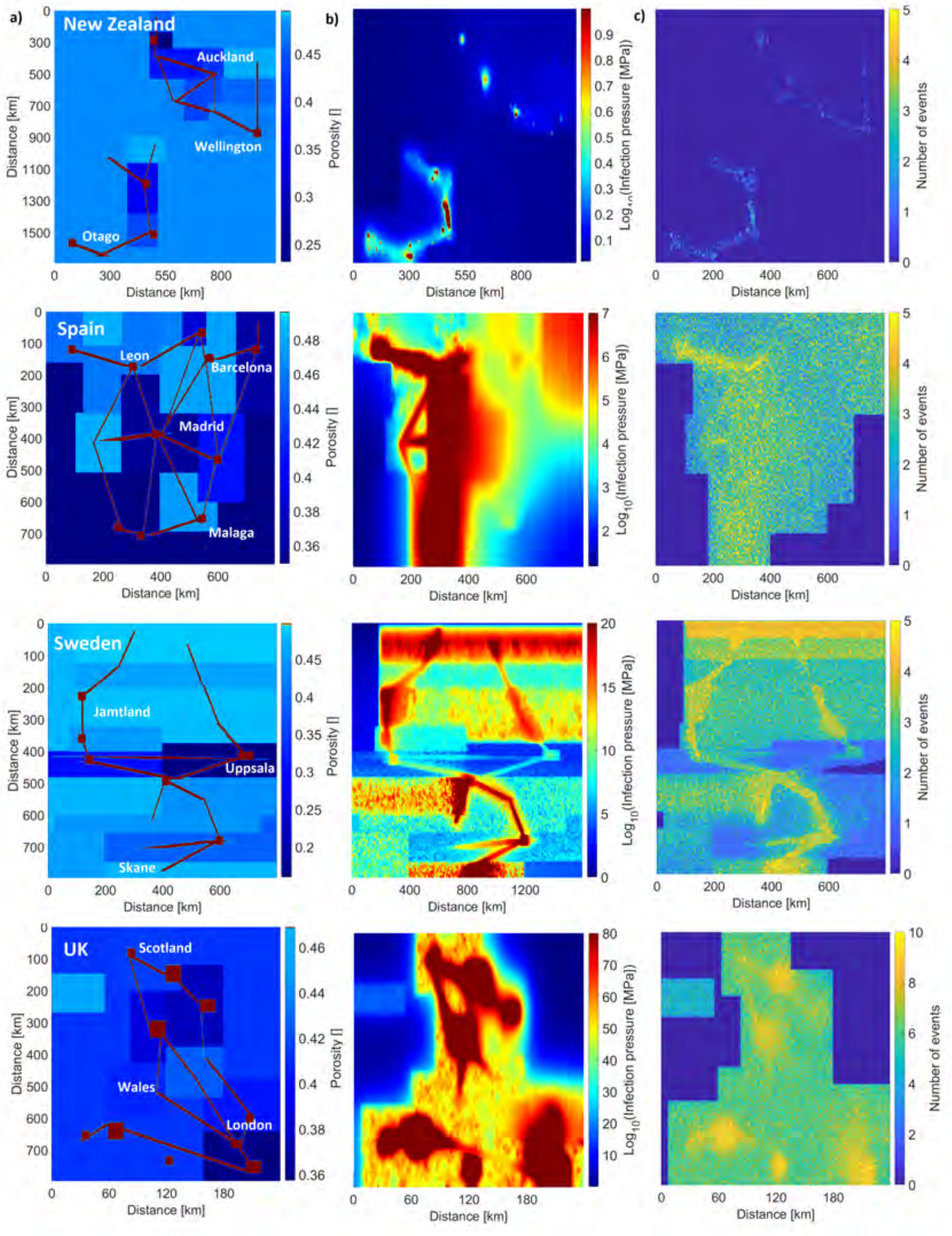

Figure C.3: a) Model setup for New Zealand, Spain, Sweden and the UK showing the source locations (red) signifying airports and intercity rail lines, and the various shades of blue scale with population density and delineate federal states. b) Calculated infection pressure at the end of the simulation. Note change in scale bar for each country. c) The number of repeated infections calculated in the model highlights the most affected regions and shows how elevated infection pressures b) continue to generate model infections.

Country	Difference
Italy	-0.9%
Germany	-3%
Switzerland	-0.1%
Spain	-3%
UK	-1%
USA	-0.7%
Austria	-0.9%
France	-0.2%
Brazil	-0.5%
Sweden	-0.5%
Belgium	-0.9%
New Zealand	-0.05%
Melbourne	-0.1%

Table C.1: Difference between model and observations averaged for entire record (in percent). We estimate errors by comparing, point for point, the difference between the (normalized) observed cumulative infections, with the (normalized) cumulative model infections. We then take the average of these differences for the entire record.

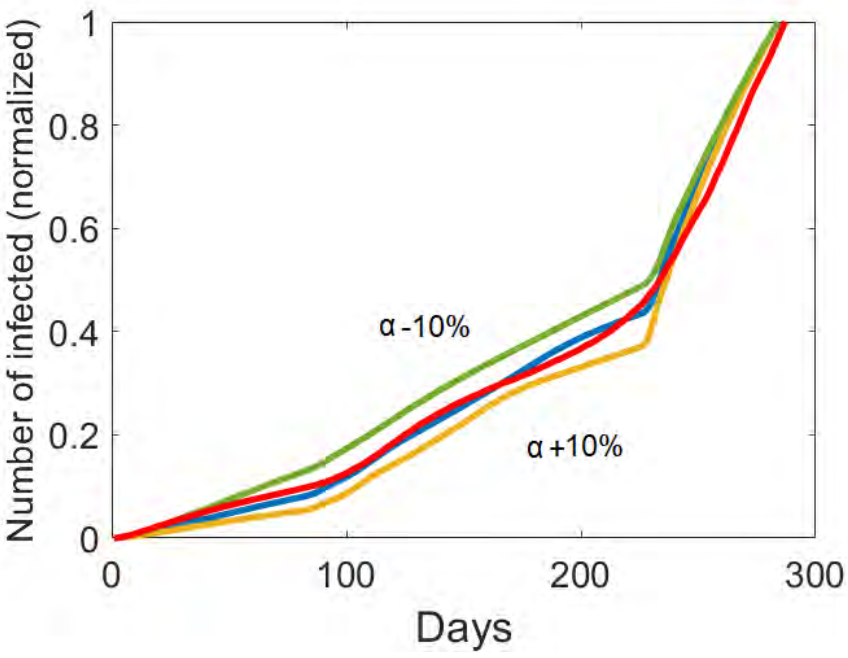

Figure C.4: Results with parameter variation for the USA. Comparison of model and data in the manuscript (red and blue lines). Model results varying alpha by plus or minus 10% (yellow and green line) show poor comparisons with data, demonstrating further tight constraints on model parameters.

Country	Website	Link
Austria	Statistik Austria - Die Informationsmanger	https://www.statistik.at/atlas
Belgium	Statbel, the Belgian statistical office	https://statbel.fgov.be/en
Brazil	Instituto Brasileiro de Geografia e Estatistica	https://cidades.ibge.gov.br/brasil
France	Insee - National Institute of Statistics and Economic Studies	https://www.insee.fr/en/accueil
Germany	Statistische Ämter des Bundes und der Länder Gemeinsames Statistikportal	https://www.statistikportal.de/de
Italy	Istat Statistics	https://www.istat.it/en/
Melbourne	Research and statistics - City of Melbourne	https://www.melbourne.vic.gov.au
New Zealand	Stats New Zealand	https://www.stats.govt.nz
Spain	INE- National Statistics Institute. Spain	https://www.ine.es/en/
Sweden	Statistics Sweden	https://www.scb.se/en/
Switzerland	Bundesamt für Statistik-Statistischer Atlas der Schweiz	https://www.atlas.bfs.admin.ch/maps
UK	Research and statistics - GOV.UK	https://www.gov.uk/search/research-and-statistics
USA	United States Census Bureau	https://www.census.gov

Table C.2: Supplementary Table 1. Sources used in this study.

References

[Abe et al., 2010] Abe, Y., Ohkura, T., Shibutani, T., Hirahara, K., and Kato, M. (2010). Crustal structure beneath aso caldera, southwest japan, as derived from receiver function analysis. *Journal of volcanology and geothermal research*, 195(1):1–12.

[Adiga et al., 2020] Adiga, A., Dubhashi, D., Lewis, B., Marathe, M., Venkatramanan, S., and Vullikanti, A. (2020). Mathematical models for covid-19 pandemic: a comparative analysis. *Journal of the Indian Institute of Science*, pages 1–15.

[Aharonov and Scholz, 2018] Aharonov, E. and Scholz, C. H. (2018). A physics-based rock friction constitutive law: Steady state friction. *Journal of Geophysical Research: Solid Earth*, 123(2):1591–1614.

[Aizawa et al., 2021] Aizawa, K., Takakura, S., Asaue, H., Koike, K., Yoshimura, R., Yamazaki, K., Komatsu, S., Utsugi, M., Inoue, H., Tsukamoto, K., et al. (2021). Electrical conductive fluid-rich zones and their influence on the earthquake initiation, growth, and arrest processes: observations from the 2016 kumamoto earthquake sequence, kyushu island, japan. *Earth, Planets and Space*, 73(1):1–12.

[Antonioli et al., 2005] Antonioli, A., Piccinini, D., Chiaraluce, L., and Cocco, M. (2005). Fluid flow and seismicity pattern: Evidence from the 1997 Umbria-Marche (central Italy) seismic sequence. *Geophysical Research Letters*, 32(10):1–4.

[Bai et al., 1997] Bai, M., Meng, F., Elsworth, D., Zaman, M., and Roegiers, J.-C. (1997). Numerical modeling of stress-dependent permeability. *International Journal of Rock Mechanics and Mining Sciences*, 34(3-4):135–e1.

[Barazangi and Isacks, 1979] Barazangi, M. and Isacks, B. L. (1979). Subduction of the nazca plate beneath peru: evidence from spatial distribution of earthquakes. *Geophysical Journal International*, 57(3):537–555.

[Barberio et al., 2017] Barberio, M. D., Barbieri, M., Billi, A., Doglioni, C., and Petitta, M. (2017). Hydrogeochemical changes before and during the 2016 amatrice-norcia seismic sequence (central italy). *Scientific Reports*, 7(1):1–12.

[Barnes et al., 1978] Barnes, I., Irwin, W. P., and White, D. E. (1978). *Global distribution of carbon dioxide discharges, and major zones of seismicity*, volume 78. US Geological Survey, Water Resources Division.

[Barnes et al., 2005] Barnes, P. M., Sutherland, R., and Delteil, J. (2005). Strike-slip structure and sedimentary basins of the southern alpine fault, fiordland, new zealand. *Geological Society of America Bulletin*, 117(3-4):411–435.

[Batty et al., 2012] Batty, M., Crooks, A. T., See, L. M., and Heppenstall, A. J. (2012). Perspectives on agent-based models and geographical systems. In *Agent-based models of geographical systems*, pages 1–15. Springer.

[Becker et al., 2022] Becker, J. S., McBride, S. K., Vinnell, L. J., Saunders, W. S., Leonard, G. S., Sullivan, T. J., and Gledhill, K. (2022). Earthquakes and tsunami. In *Routledge Handbook of Environmental Hazards and Society*, pages 13–32. Routledge.

[Bennett et al., 1995] Bennett, R. A., Reilinger, R. E., Rodi, W., Li, Y., Toksöz, M. N., and Hudnut, K. (1995). Coseismic fault slip associated with the 1992 m w 6.1 joshua tree, california, earthquake: Implications for the joshua tree-landers earthquake sequence. *Journal of Geophysical Research: Solid Earth*, 100(B4):6443–6461.

[Bessat et al., 2021] Bessat, A., Pilet, S., Podladchikov, Y. Y., and Schmalholz, S. M. (2021). Melt migration and chemical differentiation by reactive porosity waves. *Geochemistry, Geophysics, Geosystems*, page e2021GC009963.

[Bignami et al., 2019] Bignami, C., Valerio, E., Carminati, E., Doglioni, C., Tizzani, P., and Lanari, R. (2019). Volume unbalance on the 2016 Amatrice - Norcia (Central Italy) seismic sequence and insights on normal fault earthquake mechanism. *Scientific Reports*, 9(1):1–13.

[Bilham and King, 1989] Bilham, R. and King, G. (1989). The morphology of strike-slip faults: Examples from the san andreas fault, california. *Journal of Geophysical Research: Solid Earth*, 94(B8):10204–10216.

[Bird, 2003] Bird, P. (2003). An updated digital model of plate boundaries. *Geochemistry, Geophysics, Geosystems*, 4(3).

[Bizzarri and Cocco, 2006] Bizzarri, A. and Cocco, M. (2006). A thermal pressurization model for the spontaneous dynamic rupture propagation on a three-dimensional fault: 1. methodological approach. *Journal of Geophysical Research: Solid Earth*, 111(B5).

[Boncio and Lavecchia, 2000] Boncio, P. and Lavecchia, G. (2000). A geological model for the colfiorito earthquakes (september-october 1997, central italy). *Journal of Seismology*, 4(4):345–356.

[Bonfanti et al., 2012] Bonfanti, P., Genzano, N., Heinicke, J., Italiano, F., Martinelli, G., Pergola, N., Telesca, L., and Tramutoli, V. (2012). Evidence of co 2-gas emission variations in the central apennines (italy) during the l'aquila seismic sequence (march-april 2009). *Bollettino di Geofisica Teorica ed Applicata*, 53(1).

[Boschetti et al., 2019] Boschetti, T., Barbieri, M., Barberio, M., Billi, A., Franchini, S., and Petitta, M. (2019). Co2 inflow and elements desorption prior to a seismic sequence, amatrice-norcia 2016, italy. *Geochemistry, Geophysics, Geosystems*, 20(5):2303–2317.

[Bosl and Nur, 2002] Bosl, W. and Nur, A. (2002). Aftershocks and pore fluid diffusion following the 1992 landers earthquake. *Journal of Geophysical Research: Solid Earth*, 107(B12):ESE–17.

[Burg, 2018] Burg, J.-P. (2018). Geology of the onshore makran accretionary wedge: Synthesis and tectonic interpretation. *Earth-Science Reviews*, 185:1210–1231.

[Cacas et al., 1990] Cacas, M.-C., Ledoux, E., de Marsily, G., Tillie, B., Barbreau, A., Durand, E., Feuga, B., and Peaudecerf, P. (1990). Modeling fracture flow with a stochastic discrete fracture network: calibration and validation: 1. the flow model. *Water Resources Research*, 26(3):479–489.

[Carcione et al., 2020] Carcione, J. M., Santos, J. E., Bagaini, C., and Ba, J. (2020). A simulation of a covid-19 epidemic based on a deterministic seir model. *Frontiers in public health*, 8:230.

[Carcione and Tinivella, 2001] Carcione, J. M. and Tinivella, U. (2001). The seismic response to overpressure: a modelling study based on laboratory, well and seismic data. *Geophysical Prospecting*, 49(5):523–539.

[Carro et al., 2005] Carro, M., De Amicis, M., and Luzi, L. (2005). Hydrogeological changes related to the Umbria-Marche earthquake of 26 September 1997 (Central Italy). *Natural Hazards*, 34(3):315–339.

[Cattania et al., 2018] Cattania, C., Werner, M. J., Marzocchi, W., Hainzl, S., Rhoades, D., Gerstenberger, M., Liukis, M., Savran, W., Christophersen, A., Helmstetter, A., et al. (2018). The forecasting skill of physics-based seismicity models during the 2010–2012 canterbury, new zealand, earthquake sequence. *Seismological Research Letters*, 89(4):1238–1250.

[Cherniawsky et al., 2007] Cherniawsky, J. Y., Titov, V. V., Wang, K., and Li, J.-Y. (2007). Numerical simulations of tsunami waves and currents for southern vancouver island from a cascadia megathrust earthquake. *Pure and Applied Geophysics*, 164(2):465–492.

[Chëry et al., 2001] Chëry, J., Carretier, S., and Ritz, J.-F. (2001). Postseismic stress transfer explains time clustering of large earthquakes in mongolia. *Earth and Planetary Science Letters*, 194(1-2):277–286.

[Chiarabba et al., 2009] Chiarabba, C., Amato, A., Anselmi, M., Baccheschi, P., Bianchi, I., Cattaneo, M., Cecere, G., Chiaraluce, L., Ciaccio, M., De Gori, P., et al. (2009). The 2009 l'aquila (central italy) mw6. 3 earthquake: Main shock and aftershocks. *Geophysical Research Letters*, 36(18).

[Chiarabba et al., 2020] Chiarabba, C., Buttinelli, M., Cattaneo, M., and De Gori, P. (2020). Large Earthquakes Driven by Fluid Overpressure: The Apennines Normal Faulting System Case. *Tectonics*, 39(4):2–3.

[Chiaraluce et al., 2017] Chiaraluce, L., Di Stefano, R., Tinti, E., Scognamiglio, L., Michele, M., Casarotti, E., Cattaneo, M., De Gori, P., Chiarabba, C., Monachesi, G., Lombardi, A., Valoroso, L., Latorre, D., and Marzorati, S. (2017). The 2016 central Italy seismic sequence: A first look at the mainshocks, aftershocks, and source models. *Seismological Research Letters*, 88(3):757–771.

[Chiaraluce et al., 2003] Chiaraluce, L., Ellsworth, W., Chiarabba, C., and Cocco, M. (2003). Imaging the complexity of an active normal fault system: The 1997 colfiorito (central italy) case study. *Journal of Geophysical Research: Solid Earth*, 108(B6).

[Chiodini et al., 2011] Chiodini, G., Caliro, S., Cardellini, C., Frondini, F., Inguaggiato, S., and Matteucci, F. (2011). Geochemical evidence for and characterization of co2 rich gas sources in the epicentral area of the abruzzo 2009 earthquakes. *Earth and Planetary Science Letters*, 304(3-4):389–398.

[Chiodini et al., 2004] Chiodini, G., Cardellini, C., Amato, A., Boschi, E., Caliro, S., Frondini, F., and Ventura, G. (2004). Carbon dioxide Earth degassing and seismogenesis in central and southern Italy. *Geophysical Research Letters*, 31(7):2–5.

[Chiodini et al., 2013] Chiodini, G., Cardellini, C., Caliro, S., Chiarabba, C., and Frondini, F. (2013). Advective heat transport associated with regional earth degassing in central apennine (italy). *Earth and Planetary Science Letters*, 373:65–74.

[Chiodini et al., 2020] Chiodini, G., Cardellini, C., Di Luccio, F., Selva, J., Frondini, F., Caliro, S., Rosiello, A., Beddini, G., and Ventura, G. (2020). Correlation between tectonic co2 earth degassing and seismicity is revealed by a 10-year record in the apennines, italy. *Science advances*, 6(35):eabc2938.

[Chiodini et al., 1999] Chiodini, G., Frondini, F., Kerrick, D. M., Rogie, J., Parello, F., Peruzzi, L., and Zanzari, A. R. (1999). Quantification of deep CO2 fluxes from Central Italy. Examples of carbon balance for regional aquifers and of soil diffuse degassing. *Chemical Geology*, 159(1-4):205–222.

[Chiodini et al., 1995] Chiodini, G., Frondini, F., and Ponziani, F. (1995). Deep structures and carbon dioxide degassing in central italy. *Geothermics*, 24(1):81–94.

[Chiodini et al., 2012] Chiodini, G., Tassi, F., Caliro, S., Chiarabba, C., Vaselli, O., and Rouwet, D. (2012). Time-dependent co2 variations in lake albano associated with seismic activity. *Bulletin of volcanology*, 74(4):861–871.

[Christenson et al., 2015] Christenson, B., Németh, K., Rouwet, D., Tassi, F., Vandemeulebrouck, J., and Varekamp, J. C. (2015). *Volcanic Lakes*. Springer.

[Civico et al., 2015] Civico, R., Pucci, S., De Martini, P. M., and Pantosti, D. (2015). Morphotectonic analysis of the long-term surface expression of the 2009 l'aquila earthquake fault (central italy) using airborne lidar data. *Tectonophysics*, 644:108–121.

[Collettini and Barchi, 2002] Collettini, C. and Barchi, M. R. (2002). A low-angle normal fault in the Umbria region (Central Italy): A mechanical model for the related microseismicity. *Tectonophysics*, 359(1-2):97–115.

[Collettini et al., 2013] Collettini, C., Viti, C., Tesei, T., and Mollo, S. (2013). Thermal decomposition along natural carbonate faults during earthquakes. *Geology*, 41(8):927–930.

[Connolly and Podladchikov, 2015] Connolly, J. A. and Podladchikov, Y. Y. (2015). An analytical solution for solitary porosity waves: dynamic permeability and fluidization of nonlinear viscous and viscoplastic rock. *Geofluids*, 15(1-2):269–292.

[Console et al., 2007] Console, R., Murru, M., Catalli, F., and Falcone, G. (2007). Real time forecasts through an earthquake clustering model constrained by the rate-and-state constitutive law: Comparison with a purely stochastic etas model. *Seismological research letters*, 78(1):49–56.

[Contoyiannis et al., 2020] Contoyiannis, Y., Stavrinides, S. G., P Hanias, M., Kampitakis, M., Papadopoulos, P., Picos, R., and M Potirakis, S. (2020). A universal physics-based model describing covid-19 dynamics in europe. *International Journal of Environmental Research and Public Health*, 17(18):6525.

[Cortés-Aranda et al., 2015] Cortés-Aranda, J., González, G., Rémy, D., and Martinod, J. (2015). Normal upper plate fault reactivation in northern chile and the subduction earthquake cycle: From geological observations and static coulomb failure stress (cfs) change. *Tectonophysics*, 639:118–131.

[D'agostino et al., 2008] D'agostino, N., Avallone, A., Cheloni, D., D'anastasio, E., Mantenuto, S., and Selvaggi, G. (2008). Active tectonics of the adriatic region from gps and earthquake slip vectors. *Journal of Geophysical Research: Solid Earth*, 113(B12).

[D'agostino et al., 2012] D'agostino, N., Cheloni, D., Fornaro, G., Giuliani, R., and Reale, D. (2012). Space-time distribution of afterslip following the 2009 l'aquila earthquake. *Journal of Geophysical Research: Solid Earth*, 117(B2).

[Darcy, 1856] Darcy, H. (1856). The public fountains of the city of dijon. *Victor Dalmont, Paris, France.*

[De Paola et al., 2011] De Paola, N., Chiodini, G., Hirose, T., Cardellini, C., Caliro, S., and Shimamoto, T. (2011). The geochemical signature caused by earthquake propagation in carbonate-hosted faults. *Earth and Planetary Science Letters*, 310(3-4):225–232.

[DHHS,] DHHS. Department of health and human services - victorian coronavirus (covid-19) data. `https://www.dhhs.vic.gov.au/victorian-coronavirus-covid-19-data`. Online; accessed 31 January 2021.

[Di Domenica et al., 2014] Di Domenica, A., Bonini, L., Calamita, F., Toscani, G., Galuppo, C., and Seno, S. (2014). Analogue modeling of positive inversion tectonics along differently oriented pre-thrusting normal faults: An application to the Central-Northern Apennines of Italy. *Bulletin of the Geological Society of America*, 126(7-8):943–955.

[Di Domenica et al., 2012] Di Domenica, A., Turtù, A., Satolli, S., and Calamita, F. (2012). Inherited discontinuities in curved belt development: The oblique thrust front of the Central-Northern Apennines. *Rendiconti Online Societa Geologica Italiana*, 21(PART 1):30–32.

[Di Domenica et al., 2012] Di Domenica, A., Turtù, A., Satolli, S., and Calamita, F. (2012). Relationships between thrusts and normal faults in curved belts: new insight in the inversion tectonics of the central-northern apennines (italy). *Journal of Structural Geology*, 42:104–117.

[Di Donato and Blunt, 2004] Di Donato, G. and Blunt, M. J. (2004). Streamline-based dual-porosity simulation of reactive transport and flow in fractured reservoirs. *Water Resources Research*, 40(4).

[Di Luccio et al., 2010] Di Luccio, F., Ventura, G., Di Giovambattista, R., Piscini, A., and Cinti, F. R. (2010). Normal faults and thrusts reactivated by deep fluids: The 6 April 2009 Mw 6.3 L'Aquila earthquake, central Italy. *Journal of Geophysical Research: Solid Earth*, 115(6).

[Di Toro et al., 2011] Di Toro, G., Han, R., Hirose, T., De Paola, N., Nielsen, S., Mizoguchi, K., Ferri, F., Cocco, M., and Shimamoto, T. (2011). Fault lubrication during earthquakes. *Nature*, 471(7339):494–498.

[Dieterich, 1979] Dieterich, J. H. (1979). Modeling of rock friction: 1. experimental results and constitutive equations. *Journal of Geophysical Research: Solid Earth*, 84(B5):2161–2168.

[Dobrynina et al., 2017] Dobrynina, A., Albaric, J., Deschamps, A., Perrot, J., Ferdinand, R., Déverchère, J., San'kov, V., and Chechel'nitskii, V. (2017). Seismic wave attenuation in the lithosphere of the north tanzanian divergence zone (east african rift system). *Russian Geology and Geophysics*, 58(2):253–265.

[Dong et al., 2019] Dong, Y., Fu, Y., Yeh, T.-C. J., Wang, Y.-L., Zha, Y., Wang, L., and Hao, Y. (2019). Equivalence of discrete fracture network and porous media models by hydraulic tomography. *Water Resources Research*, 55(4):3234–3247.

[ECDC,] ECDC. European centre for disease prevention and control - an agency of the european union. `https://www.ecdc.europa.eu/en/covid-19/data`. Online; accessed 31 January 2021.

[Ellsworth et al., 1981] Ellsworth, W., Lindh, A., Prescott, W., and Herd, D. (1981). The 1906 san francisco earthquake and the seismic cycle. *Earthquake prediction: An international review*, 4:126–140.

[Enescu et al., 2009] Enescu, B., Mori, J., Miyazawa, M., and Kano, Y. (2009). Omori-utsu law c-values associated with recent moderate earthquakes in japan. *Bulletin of the Seismological Society of America*, 99(2A):884–891.

[Ettinger et al., 2021] Ettinger, N. P., Larson, T. E., Kerans, C., Thibodeau, A. M., Hattori, K. E., Kacur, S. M., and Martindale, R. C. (2021). Ocean acidification and photic-zone anoxia at the toarcian oceanic anoxic event: Insights from the adriatic carbonate platform. *Sedimentology*, 68(1):63–107.

[Evans, 2009] Evans, J. P. (2009). Historical seismicity analysis of the mainshock and aftershocks of the 1857 ft. tejon earthquake, san andreas fault, from ft. tejon. *Final Rept. US Geol. Surv. Contract 02HQGR0010.*

[Fisher, 1937] Fisher, R. A. (1937). The wave of advance of advantageous genes. *Annals of eugenics*, 7(4):355–369.

[Frezzotti et al., 2009] Frezzotti, M. L., Peccerillo, A., and Panza, G. (2009). Carbonate metasomatism and co2 lithosphere–asthenosphere degassing beneath the western mediterranean: an integrated model arising from petrological and geophysical data. *Chemical Geology*, 262(1-2):108–120.

[Frondini et al., 2019] Frondini, F., Cardellini, C., Caliro, S., Beddini, G., Rosiello, A., and Chiodini, G. (2019). Measuring and interpreting co2 fluxes at regional scale: the case of the apennines, italy. *Journal of the Geological Society*, 176(2):408–416.

[Fujino and Yamasaki, 1984] Fujino, T. and Yamasaki, T. (1984). Geologic and geothermal structure of the hatchobaru field, central kyushu, japan. *Geotherm. Resour. Counc. Trans*, 8:425–430.

[Fukahata and Hashimoto, 2016] Fukahata, Y. and Hashimoto, M. (2016). Simultaneous estimation of the dip angles and slip distribution on the faults of the 2016 kumamoto earthquake through a weak nonlinear inversion of insar data. *Earth, Planets and Space*, 68(1):1–10.

[Galadini and Galli, 2003] Galadini, F. and Galli, P. (2003). Paleoseismology of silent faults in the Central Apennines (Italy): The Mt. Vettore and Laga Mts. faults. *Annals of Geophysics*, 46(5):815–836.

[Galli et al., 2010] Galli, P., Giaccio, B., and Messina, P. (2010). The 2009 central italy earthquake seen through 0.5 myr-long tectonic history of the l'aquila faults system. *Quaternary Science Reviews*, 29(27-28):3768–3789.

[Galli et al., 2021] Galli, P., Peronace, E., and Messina, P. (2021). Archaeoseismic evidence of surface faulting in 1703 norcia earthquake (central italian apennines, mw 6.9). *Geosciences*, 12(1):14.

[Galluzzo and Santantonio, 2002] Galluzzo, F. and Santantonio, M. (2002). The sabina plateau: a new element in the mesozoic palaeogeography of central apennines. *Bollettino della Società Geologica Italiana*, 1:561–588.

[Genzano et al., 2009] Genzano, N., Aliano, C., Corrado, R., Filizzola, C., Lisi, M., Mazzeo, G., Paciello, R., Pergola, N., and Tramutoli, V. (2009). Rst analysis of msg-seviri tir radiances at the time of the abruzzo 6 april 2009 earthquake. *Natural Hazards and Earth System Sciences*, 9(6):2073–2084.

[Gharakhanlou and Hooshangi, 2020] Gharakhanlou, N. M. and Hooshangi, N. (2020). Spatio-temporal simulation of the novel coronavirus (covid-19) outbreak using the agent-based modeling approach (case study: Urmia, iran). *Informatics in Medicine Unlocked*, 20:100403.

[Gilbert and Bankes, 2002] Gilbert, N. and Bankes, S. (2002). Platforms and methods for agent-based modeling. *Proceedings of the National Academy of Sciences*, 99(suppl 3):7197–7198.

[Girault et al., 2018] Girault, F., Adhikari, L. B., France-Lanord, C., Agrinier, P., Koirala, B. P., Bhattarai, M., Mahat, S. S., Groppo, C., Rolfo, F., Bollinger, L., et al. (2018). Persistent co 2 emissions and hydrothermal unrest following the 2015 earthquake in nepal. *Nature communications*, 9(1):1–10.

[Guidoboni et al., 2015] Guidoboni, E., Valensise, G., et al. (2015). On the complexity of earthquake sequences: a historical seismology perspective based on the l'aquila seismicity (abruzzo, central italy), 1315-1915. *Earthquakes and structures*.

[Gunatilake and Miller, 2022] Gunatilake, T. and Miller, S. A. (2022). Spatio-temporal complexity of aftershocks in the apennines controlled by permeability dynamics and decarbonization. *Journal of Geophysical Research: Solid Earth*, page e2022JB024154.

[Guo et al., 2017] Guo, X., Zou, G., Wang, Y., Wang, Y., and Gao, T. (2017). Investigation of the temperature effect on rock permeability sensitivity. *Journal of Petroleum Science and Engineering*, 156:616–622.

[Han et al., 2007] Han, R., Shimamoto, T., Hirose, T., Ree, J.-H., and Ando, J.-i. (2007). Ultralow friction of carbonate faults caused by thermal decomposition. *Science*, 316(5826):878–881.

[Handa et al., 1992] Handa, S., Tanaka, Y., and Suzuki, A. (1992). The electrical high conductivity layer beneath the northern okinawa trough, inferred from geomagnetic depth sounding in northern and central kyushu, japan. *Journal of geomagnetism and geoelectricity*, 44(7):505–520.

[Hashimoto, 2020] Hashimoto, M. (2020). Postseismic deformation following the 2016 Kumamoto earthquake detected by ALOS-2/PALSAR-2. *Earth, Planets and Space*, 72(1).

[Hata et al., 2016] Hata, M., Takakura, S., Matsushima, N., Hashimoto, T., and Utsugi, M. (2016). Crustal magma pathway beneath aso caldera inferred from three-dimensional electrical resistivity structure. *Geophysical Research Letters*, 43(20):10–720.

[Hauksson et al., 1995] Hauksson, E., Jones, L. M., and Hutton, K. (1995). The 1994 northridge earthquake sequence in california: Seismological and tectonic aspects. *Journal of Geophysical Research: Solid Earth*, 100(B7):12335–12355.

[Hauksson et al., 1993] Hauksson, E., Jones, L. M., Hutton, K., and Eberhart-Phillips, D. (1993). The 1992 landers earthquake sequence: Seismological observations. *Journal of Geophysical Research: Solid Earth*, 98(B11):19835–19858.

[He et al., 2019] He, P., Wen, Y., Xu, C., and Chen, Y. (2019). Complete three-dimensional near-field surface displacements from imaging geodesy techniques applied to the 2016 Kumamoto earthquake. *Remote Sensing of Environment*, 232(July):111321.

[Heinicke et al., 2012] Heinicke, J., Martinelli, G., and Telesca, L. (2012). Geodynamically induced variations in the emission of co2 gas at san faustino (central apennines, italy). *Geofluids*, 12(2):123–132.

[Heinze et al., 2017a] Heinze, T., Hamidi, S., Galvan, B., and Miller, S. A. (2017a). Numerical simulation of the 2008 west-bohemian earthquake swarm. *Tectonophysics*, 694:436–443.

[Heinze et al., 2017b] Heinze, T., Hamidi, S., Galvan, B., and Miller, S. A. (2017b). Numerical simulation of the 2008 west-bohemian earthquake swarm. *Tectonophysics*, 694:436–443.

[Helmstetter and Sornette, 2003] Helmstetter, A. and Sornette, D. (2003). Predictability in the epidemic-type aftershock sequence model of interacting triggered seismicity. *Journal of Geophysical Research: Solid Earth*, 108(B10).

[Hendriyana and Tsuji, 2019] Hendriyana, A. and Tsuji, T. (2019). Migration of Very Long Period Seismicity at Aso Volcano, Japan, Associated With the 2016 Kumamoto Earthquake. *Geophysical Research Letters*, 46(15):8763–8771.

[Himematsu and Furuya, 2020] Himematsu, Y. and Furuya, M. (2020). Coseismic and Postseismic Crustal Deformation Associated With the 2016 Kumamoto Earthquake Sequence Revealed by PALSAR-2 Pixel Tracking and InSAR. *Earth and Space Science*, 7(10):1–19.

[Hinga, 2015] Hinga, B. D. R. (2015). *Ring of Fire: An Encyclopedia of the Pacific Rim's Earthquakes, Tsunamis, and Volcanoes: An Encyclopedia of the Pacific Rim's Earthquakes, Tsunamis, and Volcanoes*. ABC-CLIO.

[Hirowatari, 1991] Hirowatari, K. (1991). Development-related changes in the hatchobaru geothermal system, japan. *Geochemical journal*, 25(4):283–299.

[Holmdahl and Buckee, 2020] Holmdahl, I. and Buckee, C. (2020). Wrong but useful—what covid-19 epidemiologic models can and cannot tell us. *New England Journal of Medicine*, 383(4):303–305.

[Igarashi and Kato, 2021] Igarashi, T. and Kato, A. (2021). Evolution of aseismic slip rate along plate boundary faults before and after megathrust earthquakes. *Communications Earth & Environment*, 2(1):1–7.

[Improta et al., 2019] Improta, L., Latorre, D., Margheriti, L., Nardi, A., Marchetti, A., Lombardi, A. M., Castello, B., Villani, F., Ciaccio, M. G., Mele, F. M., et al. (2019). Multi-segment rupture of the 2016 amatrice-visso-norcia seismic sequence (central italy) constrained by the first high-quality catalog of early aftershocks. *Scientific reports*, 9(1):1–13.

[Irwin and Barnes, 1980] Irwin, W. P. and Barnes, I. (1980). Tectonic relations of carbon dioxide discharges and earthquakes. *Journal of Geophysical Research: Solid Earth*, 85(B6):3115–3121.

[Ishimura et al., 2021] Ishimura, D., Tsutsumi, H., Toda, S., Fukushima, Y., Kumahara, Y., Takahashi, N., Ichihara, T., and Takada, K. (2021). Repeated triggered ruptures on a distributed secondary fault system: an example from the 2016 Kumamoto earthquake, southwest Japan. *Earth, Planets and Space*, 73(1).

[Ishitsuka et al., 2016] Ishitsuka, K., Tsuji, T., Matsuoka, T., Nishijima, J., and Fujimitsu, Y. (2016). Heterogeneous surface displacement pattern at the Hatchobaru geothermal field inferred from SAR interferometry time-series. *International Journal of Applied Earth Observation and Geoinformation*, 44:95–103.

[Jaeger et al., 2009] Jaeger, J. C., Cook, N. G., and Zimmerman, R. (2009). *Fundamentals of rock mechanics*. John Wiley & Sons.

[John et al., 2009] John, T., Medvedev, S., Rüpke, L. H., Andersen, T. B., Podladchikov, Y. Y., and Austrheim, H. (2009). Generation of intermediate-depth earthquakes by self-localizing thermal runaway. *Nature Geoscience*, 2(2):137–140.

[Jousset et al., 2013] Jousset, P., Budi-Santoso, A., Jolly, A. D., Boichu, M., Dwiyono, S., Sumarti, S., Hidayati, S., Thierry, P., et al. (2013). Signs of magma ascent in lp and vlp seismic events and link to degassing: an example from the 2010 explosive eruption at merapi volcano, indonesia. *Journal of Volcanology and Geothermal Research*, 261:171–192.

[Kanda et al., 2019] Kanda, W., Utsugi, M., Takakura, S., and Inoue, H. (2019). Hydrothermal system of the active crater of Aso volcano (Japan) inferred from a three-dimensional resistivity structure model. *Earth, Planets and Space*, 71(1).

[Karabulut et al., 2011] Karabulut, H., Schmittbuhl, J., Özalaybey, S., Lengline, O., Kömeç-Mutlu, A., Durand, V., Bouchon, M., Daniel, G., and Bouin, M. (2011). Evolution of the seismicity in the eastern marmara sea a decade before and after the 17 august 1999 izmit earthquake. *Tectonophysics*, 510(1-2):17–27.

[Kato et al., 2016] Kato, A., Nakamura, K., and Hiyama, Y. (2016). The 2016 Kumamoto earthquake sequence. *Proceedings of the Japan Academy Series B: Physical and Biological Sciences*, 92(8):358–371.

[Kawaguchi et al., 2021] Kawaguchi, M., Hasenaka, T., Koga, K. T., Rose-Koga, E. F., Yasuda, A., Hokanishi, N., Mori, Y., Shimizu, K., and Ushikubo, T. (2021). Persistent gas emission originating from a deep basaltic magma reservoir of an active volcano: the case of aso volcano, japan. *Contributions to Mineralogy and Petrology*, 176(1):1–24.

[Kim et al., 2021] Kim, H. N., So, B.-D., Kim, M. S., Han, K. S., and Oh, S. B. (2021). Seismic fault weakening via co2 pressurization enhanced by mechanical deformation of dolomite fault gouges. *Geology*.

[Kobayashi, 2017] Kobayashi, T. (2017). Earthquake rupture properties of the 2016 Kumamoto earthquake foreshocks (M j 6.5 and M j 6.4) revealed by conventional and multiple-aperture InSAR. *Earth, Planets and Space*, 69(1):1–12.

[Kodaira et al., 2021] Kodaira, S., Iinuma, T., and Imai, K. (2021). Investigating a tsunamigenic megathrust earthquake in the japan trench. *Science*, 371(6534):eabe1169.

[Kolditz, 1995] Kolditz, O. (1995). Modelling flow and heat transfer in fractured rocks: conceptual model of a 3-d deterministic fracture network. *Geothermics*, 24(3):451–470.

[Koopman, 1983] Koopman, A. (1983). *Detachment tectonics in the central Apennines, Italy*. PhD thesis, Instituut voor Aardwetenschappen RUU.

[Lamy-Chappuis et al., 2020] Lamy-Chappuis, B., Heinrich, C. A., Driesner, T., and Weis, P. (2020). Mechanisms and patterns of magmatic fluid transport in cooling hydrous intrusions. *Earth and Planetary Science Letters*, 535:116111.

[Lara et al., 2004] Lara, L., Naranjo, J., and Moreno, H. (2004). Rhyodacitic fissure eruption in southern andes (cordón caulle; 40.5 s) after the 1960 (mw: 9.5) chilean earthquake: a structural interpretation. *Journal of Volcanology and Geothermal Research*, 138(1-2):127–138.

[Latham et al., 2013] Latham, J.-P., Xiang, J., Belayneh, M., Nick, H. M., Tsang, C.-F., and Blunt, M. J. (2013). Modelling stress-dependent permeability in fractured rock including effects of propagating and bending fractures. *International Journal of Rock Mechanics and Mining Sciences*, 57:100–112.

[Lay, 2018] Lay, T. (2018). A review of the rupture characteristics of the 2011 tohoku-oki mw 9.1 earthquake. *Tectonophysics*, 733:4–36.

[Lay et al., 2005] Lay, T., Kanamori, H., Ammon, C. J., Nettles, M., Ward, S. N., Aster, R. C., Beck, S. L., Bilek, S. L., Brudzinski, M. R., Butler, R., et al. (2005). The great sumatra-andaman earthquake of 26 december 2004. *Science*, 308(5725):1127–1133.

[Lei et al., 2014] Lei, Q., Latham, J.-P., Xiang, J., Tsang, C.-F., Lang, P., and Guo, L. (2014). Effects of geomechanical changes on the validity of a discrete fracture network representation of a realistic two-dimensional fractured rock. *International Journal of Rock Mechanics and Mining Sciences*, 70:507–523.

[Li and Muldowney, 1995] Li, M. Y. and Muldowney, J. S. (1995). Global stability for the seir model in epidemiology. *Mathematical biosciences*, 125(2):155–164.

[Lin, 2017] Lin, A. (2017). *The 2016 Mw 7.1 Kumamoto Earthquake: A Photographic Atlas of Coseismic Surface Ruptures Related to the Aso Volcano, Japan.* Springer.

[Lin et al., 2016] Lin, A., Satsukawa, T., Wang, M., Mohammadi Asl, Z., Fueta, R., and Nakajima, F. (2016). Coseismic rupturing stopped by aso volcano during the 2016 m w 7.1 kumamoto earthquake, japan. *Science*, 354(6314):869–874.

[Lombardi et al., 2010] Lombardi, A. M., Cocco, M., and Marzocchi, W. (2010). On the increase of background seismicity rate during the 1997–1998 umbria-marche, central italy, sequence: apparent variation or fluid-driven triggering? *Bulletin of the Seismological Society of America*, 100(3):1138–1152.

[Makarov et al., 2020] Makarov, V., Bakhtizin, A., Sushko, E., and Sushko, G. (2020). A design system for scalable agent-based models with multi-stage interactions of agents forming social connections. *Lobachevskii Journal of Mathematics*, 41(8):1492–1501.

[Manabe and Ejima, 1986] Manabe, T. and Ejima, Y. (1986). Reservior structure of the hatchobaru geothermal field and the evalua tion. *Chinetsu*, 23:1–9.

[Mancini et al., 2019] Mancini, S., Segou, M., Werner, M., and Cattania, C. (2019). Improving physics-based aftershock forecasts during the 2016–2017 central italy earthquake cascade. *Journal of Geophysical Research: Solid Earth*, 124(8):8626–8643.

[Manning and Ingebritsen, 1999] Manning, C. and Ingebritsen, S. (1999). Permeability of the continental crust: Implications of geothermal data and metamorphic systems. *Reviews of Geophysics*, 37(1):127–150.

[Martinelli et al., 2020] Martinelli, G., Facca, G., Genzano, N., Gherardi, F., Lisi, M., Pierotti, L., and Tramutoli, V. (2020). Earthquake-related signals in central italy detected by hydrogeochemical and satellite techniques. *Frontiers in Earth Science*, page 529.

[Matsushima et al., 2020] Matsushima, N., Utsugi, M., Takakura, S., Yamasaki, T., Hata, M., Hashimoto, T., and Uyeshima, M. (2020). Magmatic–hydrothermal system of Aso Volcano, Japan, inferred from electrical resistivity structures. *Earth, Planets and Space*, 72(1).

[McCoy-West et al., 2011] McCoy-West, A. J., Milicich, S., Robinson, T., Bignall, G., and Harvey, C. C. (2011). Geothermal resources in the pacific islands: the potential of power generation to benefit indigenous communities. In *Proceedings of the Thirty-Sixth Workshop on Geothermal Reservoir Engineering.*

[Michele et al., 2020] Michele, M., Chiaraluce, L., Di Stefano, R., and Waldhauser, F. (2020). Fine-scale structure of the 2016–2017 central Italy seismic sequence from data recorded at the Italian national network. *Journal of Geophysical Research: Solid Earth*, 125(4):1–26.

[Micklethwaite and Cox, 2004] Micklethwaite, S. and Cox, S. F. (2004). Fault-segment rupture, aftershock-zone fluid flow, and mineralization. *Geology*, 32(9):813–816.

[Miller, 2013] Miller, S. A. (2013). The role of fluids in tectonic and earthquake processes. In *Advances in geophysics*, volume 54, pages 1–46. Elsevier.

[Miller, 2015] Miller, S. A. (2015). Modeling enhanced geothermal systems and the essential nature of large-scale changes in permeability at the onset of slip. *Geofluids*, 15(1-2):338–349.

[Miller, 2020] Miller, S. A. (2020). Aftershocks are fluid-driven and decay rates controlled by permeability dynamics. *Nature communications*, 11(1):1–11.

[Miller et al., 2004] Miller, S. A., Collettini, C., Chiaraluce, L., Cocco, M., Barchi, M., and Kaus, B. J. (2004). Aftershocks driven by a high-pressure co2 source at depth. *Nature*, 427(6976):724–727.

[Min et al., 2004] Min, K.-B., Rutqvist, J., Tsang, C.-F., and Jing, L. (2004). Stress-dependent permeability of fractured rock masses: a numerical study. *International Journal of Rock Mechanics and Mining Sciences*, 41(7):1191–1210.

[Minami et al., 2018] Minami, T., Utsugi, M., Utada, H., Kagiyama, T., and Inoue, H. (2018). Temporal variation in the resistivity structure of the first nakadake crater, aso volcano, japan, during the magmatic eruptions from november 2014 to may 2015, as inferred by the active electromagnetic monitoring system. *Earth, Planets and Space*, 70(1):1–10.

[Minissale, 2004] Minissale, A. (2004). Origin, transport and discharge of co2 in central italy. *Earth-Science Reviews*, 66(1-2):89–141.

[Mitchell and Faulkner, 2008] Mitchell, T. and Faulkner, D. (2008). Experimental measurements of permeability evolution during triaxial compression of initially intact crystalline rocks and implications for fluid flow in fault zones. *Journal of Geophysical Research: Solid Earth*, 113(B11).

[Mitchell and Faulkner, 2012] Mitchell, T. and Faulkner, D. (2012). Towards quantifying the matrix permeability of fault damage zones in low porosity rocks. *Earth and Planetary Science Letters*, 339:24–31.

[Mitsuoka et al., 2020] Mitsuoka, A., Shito, A., Matsumoto, S., Yamashita, Y., Nakamoto, M., ichi Sakai, S., Iio, Y., Shimizu, H., Goto, K., Okada, T., Ohzono, M., Yamanaka, Y., Kosuga, M., Yoshimi, M., and Asano, Y. (2020). Spatiotemporal Change in the Stress State Around the Hypocentral Area of the 2016 Kumamoto Earthquake Sequence. *Journal of Geophysical Research: Solid Earth*, 125(9):1–21.

[Montone and Mariucci, 2020] Montone, P. and Mariucci, M. T. (2020). Constraints on the structure of the shallow crust in central italy from geophysical log data. *Scientific reports*, 10(1):1–12.

[Morita, 2019] Morita, M. (2019). Temporal variations of plume activities before the 8 october 2016 eruption of aso volcano, japan, detected by ground-based and satellite measurements. *Earth, Planets and Space*, 71(1):1–9.

[Morita et al., 2019] Morita, M., Mori, T., Yokoo, A., Ohkura, T., and Morita, Y. (2019). Continuous monitoring of soil co 2 flux at aso volcano, japan: the influence of environmental parameters on diffuse degassing. *Earth, Planets and Space*, 71(1):1–16.

[Moschella et al., 2021] Moschella, M., Ciaccio, M. G., and Latorre, D. (2021). Minor earthquake sequences in the amatrice-norcia epicentral area (central italy). *Tectonophysics*, 809:228858.

[Mwalili et al., 2020] Mwalili, S., Kimathi, M., Ojiambo, V., Gathungu, D., and Mbogo, R. (2020). Seir model for covid-19 dynamics incorporating the environment and social distancing. *BMC Research Notes*, 13(1):1–5.

[Nakagomi et al., 2021] Nakagomi, K., Terakawa, T., Matsumoto, S., and Horikawa, S. (2021). Stress and pore fluid pressure control of seismicity rate changes following the 2016 kumamoto earthquake, japan. *earth, planets and space*, 73(1):1–16.

[Namiki et al., 2018] Namiki, A., Tanaka, Y., and Yokoyama, T. (2018). Physical characteristics of scoriae and ash from 2014–2015 eruption of aso volcano, japan. *Earth, Planets and Space*, 70(1):1–21.

[Nauman Ahmed, 2020] Nauman Ahmed, M. R. e. a. (2020). Positive explicit and implicit computational techniques for reaction–diffusion epidemic model of dengue disease dynamics. *Advances in Difference Equations*, 202.

[Nimiya et al., 2017] Nimiya, H., Ikeda, T., and Tsuji, T. (2017). Spatial and temporal seismic velocity changes on kyushu island during the 2016 kumamoto earthquake. *Science advances*, 3(11):e1700813.

[Niu and Song, 2021] Niu, J. and Song, T.-R. A. (2021). Episodic transport of discrete magma batches beneath aso volcano. *Nature communications*, 12(1):1–12.

[Nur and Booker, 1972] Nur, A. and Booker, J. R. (1972). Aftershocks caused by pore fluid flow? *Science*, 175(4024):885–887.

[Nur and Byerlee, 1971] Nur, A. and Byerlee, J. (1971). An exact effective stress law for elastic deformation of rock with fluids. *Journal of geophysical research*, 76(26):6414–6419.

[Ogata et al., 1993] Ogata, Y., Matsu'ura, R. S., and Katsura, K. (1993). Fast likelihood computation of epidemic type aftershock-sequence model. *Geophysical research letters*, 20(19):2143–2146.

[Olsson, 1999] Olsson, R. (1999). An estimation of the maximum b-value in the gutenberg-richter relation. *Journal of Geodynamics*, 27(4-5):547–552.

[Omori, 1894] Omori, F. (1894). On the after-shocks of earthquakes. *J. Coll. Sci., Imp. Univ., Japan*, 7:111–200.

[Omori, 1895] Omori, F. (1895). *On the after-shocks of earthquakes.* PhD thesis, The University of Tokyo.

[Ono et al., 1995] Ono, K., Watanabe, K., Hoshizumi, H., and ichiro Ikebe, S. (1995). Ash eruption of the Naka-dake crater, Aso volcano, southwestern Japan. *Journal of Volcanology and Geothermal Research*, 66(1-4):137–148.

[Ozawa et al., 2011] Ozawa, S., Nishimura, T., Suito, H., Kobayashi, T., Tobita, M., and Imakiire, T. (2011). Coseismic and postseismic slip of the 2011 magnitude-9 tohoku-oki earthquake. *Nature*, 475(7356):373–376.

[Ozawa et al., 2016] Ozawa, T., Fujita, E., and Ueda, H. (2016). Crustal deformation associated with the 2016 kumamoto earthquake and its effect on the magma system of aso volcano. *Earth, Planets and Space*, 68(1):1–15.

[Parotidis et al., 2003] Parotidis, M., Rothert, E., and Shapiro, S. (2003). Pore-pressure diffusion: A possible triggering mechanism for the earthquake swarms 2000 in vogtland/nw-bohemia, central europe. *Geophysical research letters*, 30(20).

[Passarelli et al., 2015] Passarelli, L., Hainzl, S., Cesca, S., Maccaferri, F., Mucciarelli, M., Roessler, D., Corbi, F., Dahm, T., and Rivalta, E. (2015). Aseismic transient driving the swarm-like seismic sequence in the Pollino range, Southern Italy. *Geophysical Journal International*, 201(3):1553–1567.

[Petrillo et al., 2020] Petrillo, G., Lippiello, E., Landes, F. P., and Rosso, A. (2020). The influence of the brittle-ductile transition zone on aftershock and foreshock occurrence. *Nature communications*, 11(1):1–10.

[Podladchikov and Miller, 2013] Podladchikov, Y. and Miller, S. A. (2013). Episodic slip and waves of fluid-filled porosity. In *Poromechanics V: Proceedings of the Fifth Biot Conference on Poromechanics*, pages 790–793.

[Porreca et al., 2018] Porreca, M., Minelli, G., Ercoli, M., Brobia, A., Mancinelli, P., Cruciani, F., Giorgetti, C., Carboni, F., Mirabella, F., Cavinato, G., et al. (2018). Seismic reflection profiles and subsurface geology of the area interested by the 2016–2017 earthquake sequence (central italy). *Tectonics*, 37(4):1116–1137.

[Pruess, 2003] Pruess, K. (2003). Numerical simulation of leakage from a geologic disposal reservoir for CO2, with transitions between super-and sub-critical conditions. *TOUGH Symposium 2003*, pages 1–8.

[Rice, 1992] Rice, J. (1992). *Fault mechanics and transport properties of rocks*. Academic press.

[Richmond et al., 2006] Richmond, B. M., Jaffe, B., Gelfenbaum, G., and Morton, R. (2006). Geologic impacts of the 2004 indian ocean tsunami on indonesia, sri lanka, and the maldives. *Zeitschrift für Geomorphologie*, 146:235–251.

[Ritchie and Roser, 2014] Ritchie, H. and Roser, M. (2014). Natural disasters. *Our World in Data*.

[Rogers and Dragert, 2003] Rogers, G. and Dragert, H. (2003). Episodic tremor and slip on the cascadia subduction zone: The chatter of silent slip. *science*, 300(5627):1942–1943.

[Ruina, 1983] Ruina, A. (1983). Slip instability and state variable friction laws. *Journal of Geophysical Research: Solid Earth*, 88(B12):10359–10370.

[Ruiz and Madariaga, 2018] Ruiz, S. and Madariaga, R. (2018). Historical and recent large megathrust earthquakes in chile. *Tectonophysics*, 733:37–56.

[Rutqvist et al., 2002] Rutqvist, J., Wu, Y.-S., Tsang, C.-F., and Bodvarsson, G. (2002). A modeling approach for analysis of coupled multiphase fluid flow, heat transfer, and deformation in fractured porous rock. *International Journal of Rock Mechanics and Mining Sciences*, 39(4):429–442.

[Satake, 2014] Satake, K. (2014). Advances in earthquake and tsunami sciences and disaster risk reduction since the 2004 indian ocean tsunami. *Geoscience Letters*, 1(1):1–13.

[Savage and Svarc, 2009] Savage, J. and Svarc, J. (2009). Postseismic relaxation following the 1992 m7. 3 landers and 1999 m7. 1 hector mine earthquakes, southern california. *Journal of Geophysical Research: Solid Earth*, 114(B1).

[Scholz, 2019] Scholz, C. H. (2019). *The mechanics of earthquakes and faulting*. Cambridge university press.

[Schön, 2011] Schön, J. (2011). *Physical properties of rocks: A workbook*, volume 8. Elsevier.

[Scott et al., 2018] Scott, C. P., Arrowsmith, J. R., Nissen, E., Lajoie, L., Maruyama, T., and Chiba, T. (2018). The M7 2016 Kumamoto, Japan, Earthquake: 3-D Deformation Along the Fault and Within the Damage Zone Constrained From Differential Lidar Topography. *Journal of Geophysical Research: Solid Earth*, 123(7):6138–6155.

[Segall and Rice, 1995] Segall, P. and Rice, J. R. (1995). Dilatancy, compaction, and slip instability of a fluid-infiltrated fault. *Journal of Geophysical Research: Solid Earth*, 100(B11):22155–22171.

[Seropian et al., 2021] Seropian, G., Kennedy, B. M., Walter, T. R., Ichihara, M., and Jolly, A. D. (2021). A review framework of how earthquakes trigger volcanic eruptions. *Nature Communications*, 12(1):1–13.

[Shapiro et al., 2017] Shapiro, N. M., Droznin, D., Droznina, S. Y., Senyukov, S., Gusev, A., and Gordeev, E. (2017). Deep and shallow long-period volcanic seismicity linked by fluid-pressure transfer. *Nature Geoscience*, 10(6):442–445.

[Shelly et al., 2006] Shelly, D. R., Beroza, G. C., Ide, S., and Nakamula, S. (2006). Low-frequency earthquakes in shikoku, japan, and their relationship to episodic tremor and slip. *Nature*, 442(7099):188–191.

[Shinohara et al., 2018] Shinohara, H., Geshi, N., Yokoo, A., Ohkura, T., and Terada, A. (2018). Salt shell fallout during the ash eruption at the nakadake crater, aso volcano, japan: evidence of an underground hydrothermal system surrounding the erupting vent. *Earth, Planets and Space*, 70(1):1–10.

[Shirahama et al., 2016] Shirahama, Y., Yoshimi, M., Awata, Y., Maruyama, T., Azuma, T., Miyashita, Y., Mori, H., Imanishi, K., Takeda, N., Ochi, T., Otsubo, M., Asahina, D., and Miyakawa, A. (2016). Characteristics of the surface ruptures associated with the 2016 Kumamoto earthquake sequence, central Kyushu, Japan. *Earth, Planets and Space*, 68(1):1–12.

[Sibson, 1992] Sibson, R. (1992). Implications of fault-valve behaviour for rupture nucleation and recurrence. *Tectonophysics*, 211(1-4):283–293.

[Sibson, 2007] Sibson, R. H. (2007). An episode of fault-valve behaviour during compressional inversion?—the 2004 mj6. 8 mid-niigata prefecture, japan, earthquake sequence. *Earth and Planetary Science Letters*, 257(1-2):188–199.

[Silva et al., 2020] Silva, P. C., Batista, P. V., Lima, H. S., Alves, M. A., Guimarães, F. G., and Silva, R. C. (2020). Covid-abs: An agent-based model of covid-19 epidemic to simulate health and economic effects of social distancing interventions. *Chaos, Solitons & Fractals*, 139:110088.

[Song et al., 2019] Song, K., Wang, F., Dai, Z., Iio, A., Osaka, O., and Sakata, S. (2019). Geological characteristics of landslides triggered by the 2016 Kumamoto earthquake in Mt. Aso volcano, Japan. *Bulletin of Engineering Geology and the Environment*, 78(1):167–176.

[Spallarossa et al., 2021] Spallarossa, D., Cattaneo, M., Scafidi, D., Michele, M., Chiaraluce, L., Segou, M., and Main, I. (2021). An automatically generated high-resolution earthquake catalogue for the 2016–2017 central italy seismic sequence, including p and s phase arrival times. *Geophysical Journal International*, 225(1):555–571.

[Stein, 1999] Stein, R. S. (1999). The role of stress transfer in earthquake occurrence. *Nature*, 402(6762):605–609.

[Stemberk et al., 2019] Stemberk, J., Dal Moro, G., Stemberk, J., Blahut, J., Coubal, M., Košt'ák, B., Zambrano, M., and Tondi, E. (2019). Strain monitoring of active faults in the central apennines (italy) during the period 2002–2017. *Tectonophysics*, 750:22–35.

[Stern, 2002] Stern, R. J. (2002). Subduction zones. *Reviews of geophysics*, 40(4):3–1.

[Stix and de Moor, 2018] Stix, J. and de Moor, J. M. (2018). Understanding and forecasting phreatic eruptions driven by magmatic degassing. *Earth, Planets and Space*, 70(1):1–19.

[Sudo and Hurst, 1998] Sudo, Y. and Hurst, A. W. (1998). Temperature changes at depths to 150 metres near the active crater of aso volcano: preliminary analysis of seasonal and volcanic effects. *Journal of volcanology and geothermal research*, 81(1-2):159–172.

[Sudo and Kong, 2001] Sudo, Y. and Kong, L. (2001). Three-dimensional seismic velocity structure beneath aso volcano, kyushu, japan. *Bulletin of volcanology*, 63(5):326–344.

[Sulem and Famin, 2009] Sulem, J. and Famin, V. (2009). Thermal decomposition of carbonates in fault zones: Slip-weakening and temperature-limiting effects. *Journal of Geophysical Research: Solid Earth*, 114(B3).

[Taguchi and Nakamura, 1991] Taguchi, S. and Nakamura, M. (1991). Subsurface thermal structure of the hatchobaru geothermal system, japan, determined by fluid inclusion study. *Geochemical journal*, 25(4):301–314.

[Tamburello et al., 2018] Tamburello, G., Pondrelli, S., Chiodini, G., and Rouwet, D. (2018). Global-scale control of extensional tectonics on co2 earth degassing. *Nature communications*, 9(1):1–9.

[Tanaka et al., 2004] Tanaka, A., Yamano, M., Yano, Y., and Sasada, M. (2004). Geothermal gradient and heat flow data in and around japan (i): Appraisal of heat flow from geothermal gradient data. *Earth, planets and space*, 56(12):1191–1194.

[Tavani et al., 2021] Tavani, S., Cardello, G., Vignaroli, G., Balsamo, F., Parente, M., Sabbatino, M., Raffi, I., Billi, A., and Carminati, E. (2021). Segmentation of the apenninic margin of the tyrrhenian back-arc basin forced by the subduction of an inherited transform system. *Tectonics*, 40(9):e2021TC006770.

[Terada et al., 2012] Terada, A., Hashimoto, T., and Kagiyama, T. (2012). A water flow model of the active crater lake at aso volcano, japan: fluctuations of magmatic gas and groundwater fluxes from the underlying hydrothermal system. *Bulletin of volcanology*, 74(3):641–655.

[Terakawa et al., 2020] Terakawa, T., Matsu'ura, M., and Noda, A. (2020). Elastic strain energy and pore-fluid pressure control of aftershocks. *Earth and Planetary Science Letters*, 535:116103.

[Terakawa et al., 2010] Terakawa, T., Zoporowski, A., Galvan, B., and Miller, S. A. (2010). High-pressure fluid at hypocentral depths in the l'aquila region inferred from earthquake focal mechanisms. *Geology*, 38(11):995–998.

[Tertulliani et al., 2009] Tertulliani, A., Rossi, A., Cucci, L., and Vecchi, M. (2009). L'aquila (central italy) earthquakes: The predecessors of the april 6, 2009 event. *Seismological Research Letters*, 80(6):1008–1013.

[Thompson and Burke, 1974] Thompson, G. A. and Burke, D. B. (1974). Regional geophysics of the basin and range province. *Annual Review of Earth and Planetary Sciences*, 2:213.

[Thompson et al., 2020] Thompson, R. N., Hollingsworth, T. D., Isham, V., Arribas-Bel, D., Ashby, B., Britton, T., Challenor, P., Chappell, L. H., Clapham, H., Cunniffe, N. J., et al. (2020). Key questions for modelling covid-19 exit strategies. *Proceedings of the Royal Society B*, 287(1932):20201405.

[Tsutsui and Sudo, 2004] Tsutsui, T. and Sudo, Y. (2004). Seismic reflectors beneath the central cones of aso volcano, kyushu, japan. *Journal of volcanology and geothermal research*, 131(1-2):33–58.

[Tung and Masterlark, 2018] Tung, S. and Masterlark, T. (2018). Delayed Poroelastic Triggering of the 2016 October Visso Earthquake by the August Amatrice Earthquake, Italy. *Geophysical Research Letters*, 45(5):2221–2229.

[Uchide et al., 2016] Uchide, T., Horikawa, H., Nakai, M., Matsushita, R., Shigematsu, N., Ando, R., and Imanishi, K. (2016). The 2016 kumamoto–oita earthquake sequence: aftershock seismicity gap and dynamic triggering in volcanic areas. *Earth, Planets and Space*, 68(1):1–10.

[Unglert et al., 2011] Unglert, K., Savage, M., Fournier, N., Ohkura, T., and Abe, Y. (2011). Shear wave splitting, vp/vs, and gps during a time of enhanced activity at aso caldera, kyushu. *Journal of Geophysical Research: Solid Earth*, 116(B11).

[Utsu, 1961] Utsu, T. (1961). A statistical study on the occurrence of aftershocks. *Geophys. Mag.*, 30:521–605.

[Utsu et al., 1995] Utsu, T., Ogata, Y., et al. (1995). The centenary of the omori formula for a decay law of aftershock activity. *Journal of Physics of the Earth*, 43(1):1–33.

[van Dinther et al., 2014] van Dinther, Y., Mai, P. M., Dalguer, L., and Gerya, T. (2014). Modeling the seismic cycle in subduction zones: The role and spatiotemporal occurrence of off-megathrust earthquakes. *Geophysical Research Letters*, 41(4):1194–1201.

[Vespignani et al., 2020] Vespignani, A., Tian, H., Dye, C., Lloyd-Smith, J. O., Eggo, R. M., Shrestha, M., Scarpino, S. V., Gutierrez, B., Kraemer, M. U., Wu, J., et al. (2020). Modelling covid-19. *Nature Reviews Physics*, 2(6):279–281.

[Viguerie et al., 2020] Viguerie, A., Veneziani, A., Lorenzo, G., Baroli, D., Aretz-Nellesen, N., Patton, A., Yankeelov, T. E., Reali, A., Hughes, T. J., and Auricchio, F. (2020). Diffusion–reaction compartmental models formulated in a continuum mechanics framework: application to covid-19, mathematical analysis, and numerical study. *Computational Mechanics*, 66(5):1131–1152.

[Walter et al., 2007] Walter, T. R., Wang, R., Zimmer, M., Grosser, H., Lühr, B., and Ratdomopurbo, A. (2007). Volcanic activity influenced by tectonic earthquakes: Static and dynamic stress triggering at mt. merapi. *Geophysical Research Letters*, 34(5).

[Wang, 2019] Wang, Z. (2019). Multi-parameter imaging in the 2016 mw 7.0 kumamoto earthquake, kyushu, japan and its implications for fluids in seismogenesis. *Tectonophysics*, 767:228162.

[Wilson and Head Iii, 2007] Wilson, L. and Head Iii, J. W. (2007). An integrated model of kimberlite ascent and eruption. *Nature*, 447(7140):53–57.

[Xie, 2020] Xie, G. (2020). A novel monte carlo simulation procedure for modelling covid-19 spread over time. *Scientific reports*, 10(1):1–9.

[Yagi et al., 2016] Yagi, Y., Okuwaki, R., Enescu, B., Kasahara, A., Miyakawa, A., and Otsubo, M. (2016). Rupture process of the 2016 kumamoto earthquake in relation to the thermal structure around aso volcano. *Earth, Planets and Space*, 68(1):1–6.

[Yoshida et al., 2016] Yoshida, K., Hasegawa, A., Saito, T., Asano, Y., Tanaka, S., Sawazaki, K., Urata, Y., and Fukuyama, E. (2016). Stress rotations due to the m6. 5 foreshock and m7. 3 main shock in the 2016 kumamoto, sw japan, earthquake sequence. *Geophysical Research Letters*, 43(19):10–097.

[Zhao et al., 2018] Zhao, D., Yamashita, K., and Toyokuni, G. (2018). Tomography of the 2016 Kumamoto earthquake area and the Beppu-Shimabara graben. *Scientific Reports*, 8(1):1–11.

[Zhao et al., 2010] Zhao, J., Liu, Y., Zhou, Z., and Zhao, C. (2010). Spatio-temporal characteristics of strong aftershocks of the ms8. 0 wenchuan earthquake. *Earthquake Science*, 23(3):215–221.

[Zhu et al., 2020] Zhu, W., Allison, K. L., Dunham, E. M., and Yang, Y. (2020). Fault valving and pore pressure evolution in simulations of earthquake sequences and aseismic slip. *Nature communications*, 11(1):1–11.

[Zyvoloski et al., 2008] Zyvoloski, G. A., Robinson, B. A., and Viswanathan, H. S. (2008). Generalized dual porosity: A numerical method for representing spatially variable sub-grid scale processes. *Advances in Water Resources*, 31(3):535–544.